ISSN 0370-3908

REVISTA DE LA
ACADEMIA COLOMBIANA
de Ciencias Exactas, Físicas y Naturales

LA ACADEMIA ES ÓRGANO CONSULTIVO DEL GOBIERNO NACIONAL

VOLUMEN XXXVII SUPLEMENTO 2013

DIRECTOR DE PUBLICACIONES : JOHN DOUGLAS LYNCH

CONTENIDO - CONTENTS

PHYSICS

FOREWORD

The *Latin American Symposium on Solid State Physics* (SLAFES) started in Caracas, Venezuela, and over time the symposia have taken place in 9 different Latin American countries. The last five events took place in Mérida, Venezuela (2002), Havana, Cuba (2004), Puebla, Mexico (2006), Puerto Iguazú Argentina (2008) and Maragogi, Brazil (2011).

During the last years, in the different editions of the SLAFES, the aim has been to bring together researches from Latina America and renowned scientists from around the world invited to a unique forum to discuss the latest developments regarding Solid state Physics.

The XXIst SLAFES version featured the participation of experts in various areas of Physics Solid State from countries such as Belgium, United States, Spain, Ireland, Chile and Brazil, had 270 submitted works and was attended by about 140 researchers.

The development of this event was made possible by financial support from of theUniversidad Pedagógica y Tecnológica de Colombia, Universidad Nacional de Colombia, Universidad del Norte (Barranquilla), Universidad del Magdalena, Universidade Federal de Pernambuco and the Academia Colombiana de Ciencias Exactas, Físicas y Naturales.

Editorial Chair

Jairo Roa-Rojas
Departamento de Física, Universidad Nacional de Colombia, Bogotá DC, Colombia, jroar@unal.edu.co

Carlos Arturo Parra Vargas
Escuela de Física, Universidad Pedagógica y Tecnológica de Colombia, Tunja, Colombia, carlos.parra@uptc.edu.co

ACADEMIA COLOMBIANA DE CIENCIAS EXACTAS, FÍSICAS Y NATURALES

APARTADO 44763 - BOGOTÁ, D. C., COLOMBIA
SEDE DE LA ACADEMIA: CRA. 28A No. 39A - 63
Teléfonos - Fax No. (571) 2443186, 2683290, 2682846
Correo electrónico: revista@accefyn.org.co

EMBLEMA DE LA ACADEMIA MATRIZ ESPAÑOLA

Esta revista es reseñada en:

Actualidad Iberoamericana
Agris
CIRS
Current Mathematical Publications
EBSCO
Dialnet
Index kewensis
Latindex
Mathematical Reviews
PERIÓDICA
Scielo
Online Computer Library Center - OCLC
Zentralblatt MATH
Zoological Record

MinEducación
Ministerio de Educación Nacional

PROSPERIDAD PARA TODOS

Esta Publicación se ha financiado mediante la transferencia de recursos
del Gobierno Nacional a la Academia Colombiana de Ciencias Exactas, Físicas y Naturales.
El Ministerio de Educación Nacional no es responsable de las opiniones aquí expresadas.

Armada digital, impresión y acabados:
Editorial Gente Nueva
Bogotá, D.C. - Colombia


Uptc
Universidad Pedagógica y
Tecnológica de Colombia
FVTVRVM ÆDIFICAMVS


UNIVERSIDAD DEL MAGDALENA
1962


UNIVERSIDAD
NACIONAL
DE COLOMBIA


UNIVERSIDAD
DEL NORTE


Universidade Federal
de Pernambuco
VIRTUS IMPAVIDA


F
M
Grupo Física de Materiales


de Nuevos
Grupo de Física
Materiales
GFNM

DETERMINATION OF OPTICAL PROPERTIES OF COMMERCIAL THIN FILM POLYMERS USED FOR SOLAR PROTECTION APPLICATIONS

DETERMINACIÓN DE LAS PROPIEDADES ÓPTICAS EN PELÍCULAS DELGADAS POLIMÉRICAS COMERCIALES UTILIZADAS EN APLICACIONES DE PROTECCIÓN SOLAR

Andrés Felipe Pérez Marín*, Jaime Torres Salcedo, Luis Demetrio López**, Mauricio Martínez*****

ABSTRACT

Pérez Marín A. F., J. Torres Salcedo, L. D. López, M. Martínez. Determination of optical properties of commercial thin film polymers used for solar protection applications. Rev. Acad. Colomb. Cienc., 37 (1): 7-11, 2013. ISSN 0370-3908.

A procedure to determine the optical properties of commercial polymeric films used as solar control for building skins is proposed. The spectral variation (190-1100 nm) of the refractive index and extinction coefficient of the samples were obtained through the simulation of the experimental transmittance spectra of the samples. Films of polyvinyl chloride (PVC) and poly ethylene terephthalate (PET) were analyzed. Refractive index values between 1.1 and 2.5 at λ= 500 nm and extinction coefficient values of 104 cm-1 in the ultraviolet (UV) region were found. All these results show a good fit with those given in the literature for similar thin films. A new concept for the illumination and temperature control of buildings by the use of polymeric thin films as a transparent solar protection material is presented.

Keywords: Thin films; Polymers; Optical properties; Building skins

RESUMEN

Se propone un procedimiento para determinar las propiedades ópticas de películas poliméricas comerciales utilizadas como elementos de control solar en pieles de la edificación. La variación espectral (190-1100 nm) del índice de refracción y el coeficiente de extinción de las muestras se obtuvieron a través de la simulación de los espectros de Transmitancia de las muestras. Se analizaron películas de Cloruro de Polivinilo (PVC) y

* Ph. D. Engineering Candidate - Science and Materials Technology, Universidad Nacional de Colombia - Sede Bogotá - Facultad de Ingeniería - Doctorado en Ingeniería Ciencia y Tecnología de los Materiales. Bogotá, Colombia. E-mail: afperezm@unal.edu.co

** Ph. D., Grupo de Materiales con Aplicaciones Tecnológicas, Departamento de Física, Universidad Nacional de Colombia - Sede Bogotá. Bogotá, Colombia. E-mail: njtorress@unal.edu.co

*** Ph. D. Grupo de Materiales con Aplicaciones Tecnológicas, Departamento de Física, Universidad Nacional de Colombia, Sede Bogotá, Colombia. E-mail: hmmartinezca@unal.edu.co

Poli Tereftalato de Etileno (PET). Los valores del índice de refracción están dados entre 1,1 y 2,5 para $\lambda = 500$ nm y los valores del coeficiente de extinción de 10^4 cm^{-1} se encontraron en la región ultravioleta (UV). Todos estos resultados muestran un buen ajuste con los datos que figuran en la literatura para películas delgadas similares. Es así que se presenta un nuevo concepto de iluminación y control de temperatura de los edificios mediante el uso de películas delgadas de polímeros como material de protección solar transparente.

Palabras clave: Películas delgadas; Polímeros; Propiedades ópticas; Piel de la edificación

1. Introduction

The window is the element mainly used to control the optical and thermal properties of spaces in modern architecture. For this kind of application, new materials such as polymeric thin films are being used to cover the window. Currently there is a considerable effort to optimize the optical properties of these coatings for applications of conservation of energy in buildings, facade embellishment, and greenhouses [1].

One such new material is the polymers, which are an excellent alternative not only as sun protection films for glass, but also for high-quality optics [2, 3]. The optical properties depend on the materials from which the films are made and also on the physical and chemical characteristics of the materials used as a substrate for supporting the polymeric films. Nowadays the selection of polymer films is done through the appearance of the film at first glance, but this is only a minimum necessity, because the films play a key role in the window in terms of light and thermal control of the area to be protected.

However, the optical performance of the film coatings is not well understood, due to the lack of models for obtaining and interpreting their optical properties. In the present paper, a model for determining the optical properties of polymeric thin films from transmittance measurements is proposed.

2. Experimental details

Commercial polymers were measured in the form of a thin film distributed by companies such as FilmTex. The references used were: 1) Cristal Commercial UV glass (CCial UV). This has excellent transparency and highly flexible PVC film, shine and is flexible with increased resistance to yellowing caused by sunlight. Thicknesses used: 100, 125 and 150 μm and 2) PET Film FP3 (FP3), which has good transparency, toughness, handling, low-temperature resistance, high energy conservation, and a good level of environmentally protective surfaces. Also, it shows good resistance to aging. Thicknesses used: 125 and 175μm.

The samples' thicknesses were measured with a mechanical profilometer Dektak 150 Veeco with a tip diameter of 12.5 μm. A pressure of 10 μN was applied over the samples' surface with a swept length of 3 μm for 80 seconds and a resolution of 0.083 μm.

The transmittance spectra were obtained using a T80 UV-VIS Spectrophotometer PG Instruments. The experimental data were collected in the ultraviolet, visible, and near-infrared ranges (λ = 190 to 1100 nm), with a step width of 5 nm. The computer program UV WIN 5.0 was used for data collection, using air as the standard.

2.1Theoretical Model

The physical model used for the calculation is shown in Figure 1. The polymeric film was immersed between two mediums of refractive index $\mathbf{n_0}$. A complex refractive index $\tilde{\mathbf{n}}$ is assigned to the film, and the light impinges perpendicularly to the polymeric surface.

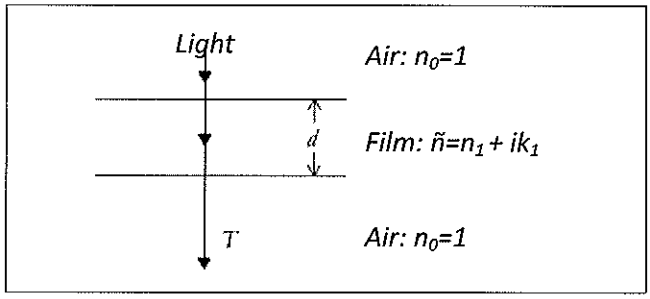

Figure 1. Physical system used to calculate the optical properties of polymeric films

The transmission coefficient T for normal incidence is given by [4]:

$$T = \frac{n_2}{n_0}\frac{[(1+g_1)^2+h_1^2]+[(1+g_2)^2+h_2^2]}{e^{2\alpha_1}+(g_1^2+h_1^2)(g_2^2+h_2^2)e^{-2\alpha_1}+Ccos\,2\gamma_1+Dsin\,2\gamma_1} \quad (1)$$

where

$$g_1 = \frac{n_0^2 - n_1^2 - k_1^2}{(n_0+n_1)^2+k_1^2}$$

$$h_1 = \frac{2n_0k_1}{(n_0+n_1)^2+k_1^2}$$

$$g_2 = \frac{{n_1}^2 - {n_2}^2 + {k_1}^2 - {k_2}^2}{(n_1 + n_2)^2 + (k_1 + k_2)^2}$$

$$h_2 = \frac{2(n_1 k_2 - n_2 k_1)}{(n_1 + n_2)^2 + (k_1 + k_2)^2}$$

$$A = 2(g_1 g_2 + h_1 h_2) \qquad B = 2(g_1 h_2 - g_2 h_1)$$

$$C = 2(g_1 g_2 - h_1 h_2) \qquad D = 2(g_1 h_2 + g_2 h_1)$$

The theoretical expression for the transmittance T of the film-air system is given as a function of λ, the wavelength, $\mathbf{n}_0$ the air refractive index, $\mathbf{n}_1$ and $\mathbf{k}_1$ the refractive index and extinction coefficient of the film, $\mathbf{d}_1$ the thickness. $\mathbf{n}_2$ and $\mathbf{k}_2$ are used when the polymeric film is supported by a substrate. In this experiment, the assigned values are $\mathbf{n}_2$=1 and $\mathbf{k}_2$=0. The thicknesses of the samples were measured using a profilometer Dektak 150 Veeco.

The procedure followed to calculate the optical properties is described by the following equation:

$$|T_{Exp} - T_{Theo}| \leq 0{,}001 \qquad (2)$$

where T_{Exp} is the experimental spectrum and T_{Theo} is theoretically obtained from Equation 1.

The theoretical values involved in Equation 2 were found by iteration using Equation 1. When Equation 2 is satisfied, the computer stops and the optical constants values are extracted.

Initially, the sample is supposed to be transparent between 500 and 1100 nm. In this region, approximate values of $\mathbf{n}_1$ are obtained, using Equation 2 and the **Wemple – DiDomenico** model [5]:

$$n = \sqrt{1 + \frac{E_0 E_d}{{E_0}^2 + \left(\frac{1237.4}{\lambda}\right)^2}} \qquad (3)$$

where $\mathbf{E}_0$ is the energy of the oscillator and $\mathbf{E}_d$ the dispersion energy, and $\mathbf{n}_1$ values are obtained over the whole spectrum. Finally, the extinction coefficient, $\mathbf{k}(\lambda)$, was theoretically determined, again using Equation 2.

3. Results and discussion

Figure 2 shows the transmittance spectra of a commercial thin film and the simulated spectrum obtained theoretically. The spectrum obtained from the simulation fit well with the experimental spectra, indicating that the mathematical model could be used to obtain the optical properties of the films. In Figure 3, the experimental spectra of the investigated samples are shown. As can be seen in the transmittances curves, (Figure 3), for wavelengths below 400 nm there is a strong absorption region, indicating that these films are excellent for UV protection applications. The samples allowed 85% transmittance of visible light between 400 to 1100 nm.

In Figure 4 the refractive index values obtained for the samples are shown. The values obtained are comparable to those found in the literature [6].

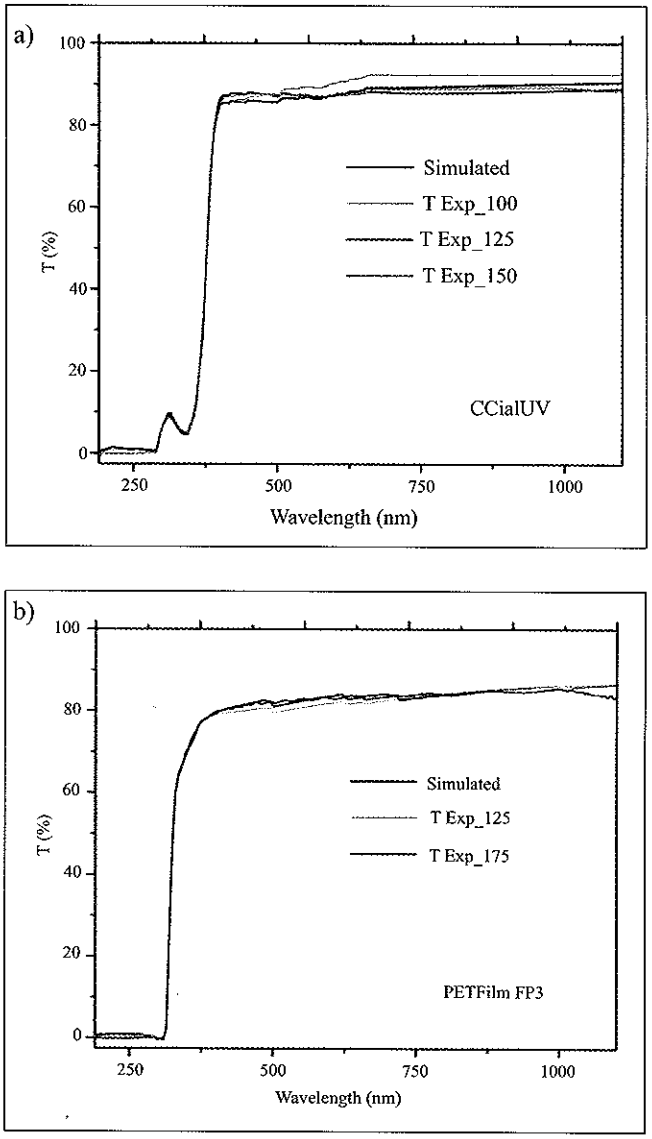

Figure 2. Simulated and experimental spectra of a FilmTex CristalCcial UV (a) and FilmTex PETFilm FP3 (b)

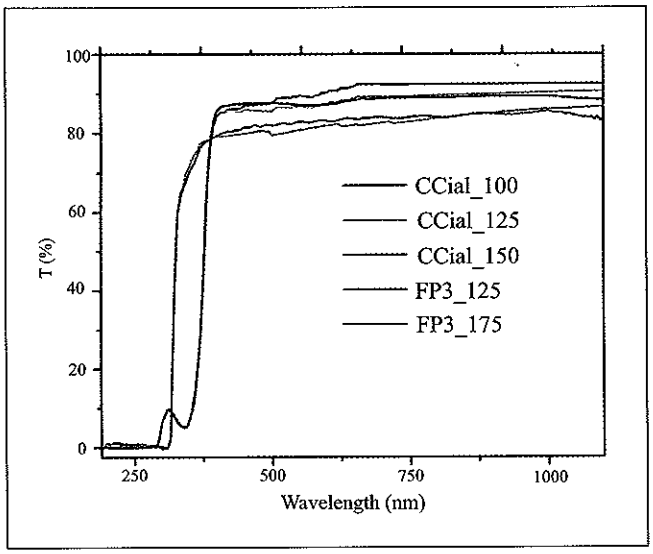

Figure 3. All transmittance spectra of polymeric films

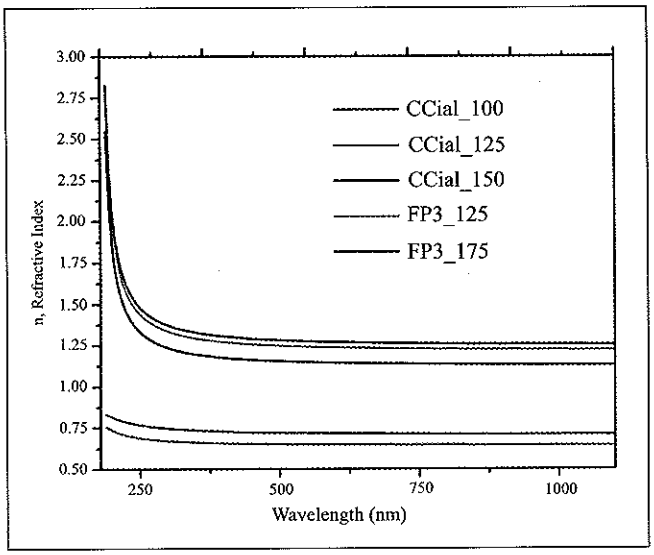

Figure 4. All refractive indexes of polymeric films

Figure 5 shows the **k** values obtained for the analyzed samples. As is shown in the figure, all the samples exhibit the same behavior in the analyzed spectral region. The samples CristalCcial 100 and PET FP3 175 have a strong absorption region for UV radiation up to 275 nm, while the other samples absorb the UV up to 274 nm. The height of the curves in the UV region is different for all the samples. This behavior could be associated with the different thicknesses of the samples.

Thicker samples allow the passage of a small percentage of short wavelengths of the UV light. From UV to NIR (1100)

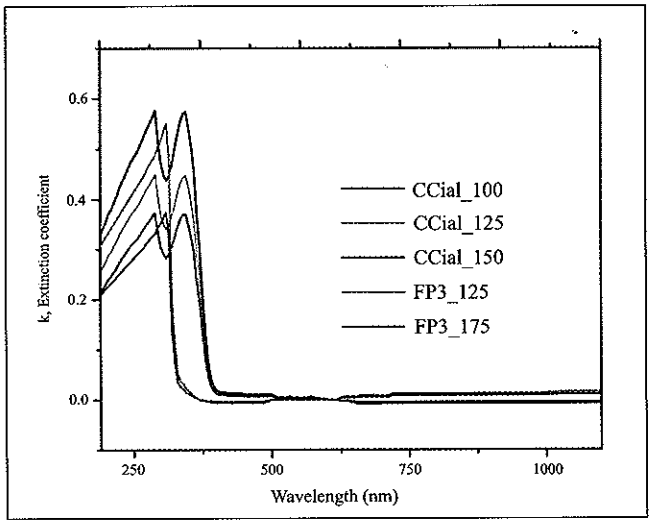

Figure 5. All extinction coeffient values of polymeric films

nm, all the samples are nearly transparent, with small absorption regions near 520 nm. If the sample is deposited on a substrate, the optical properties change, due to the presence of the substrate. This kind of system could also be analyzed using the theoretical model.

The model allows an easy determination of the optical constants of polymeric films used for the solar protection of windows.

4. Conclusions

A theoretical model was proposed for obtaining the optical properties of commercial films used as window protection. This model allows determining the spectral variation of the refractive index and absorption coefficient of polymeric films. The model could be applied to single samples, deposited on crystal substrates and multilayer systems.

Acknowledgements

The authors would like to acknowledge Film Tex Company for the supply of materials for the analysis, and especially the engineer Carlos Rincón, and National University of Colombia.

References

[1] **Roos, A., Polato, P., van Nijnatten, P., Hutchins, M.G., Olive, F., Anderson, C.** Angular dependent optical properties of low-e and solar control windows - simulations versus measurements. Sol Energy 69 (suppl.), pp. 1-6, 15-26. 2000.

[2] **Menendez, J. P., Erismann, F., Gauvin, M.A.** The advantages of plastic optical components. Optics and Photonics News, Vol. 10, Issue 8, pp. 28-30. 1999

[3] **Tolley, P.** Polymer optics gain respect. Photonics Spectra, pp. 76-79. October 2003

[4] **Heavens, O. S.** Optical Properties of Thin Solid Films. New York. Dover Publications. 2011

[5] **Wemple, S H and DiDomenico, M.** Physical Review B, 3, pp.1338-1351. 1971

[6] **Schubert, E. F.** Refractive index and extinction coefficient of materials, pp. 72, 2004.

STRUCTURAL CHARACTERIZATION, THERMAL AND MORPHOLOGICAL ANALYSIS OF MATERIALSAT ECOLOGICAL PARK THE POMA-COLOMBIA

CARACTERIZACIÓN ESTRUCTURAL, ANÁLISIS TÉRMICO Y MORFOLÓGICO DE MATERIALES EN PARQUE ECOLÓGICO LA POMA- COLOMBIA

S. Hidalgo*, D.A. Landinez Tellez*, J. Roa-Rojas*

ABSTRACT

Hidalgo, S., D. A. Landinez Téllez, J. Roa-Rojas. Structural characterization, thermal and morphological analysis of materialsat ecological park the Poma-Colombia. Rev. Acad. Colomb. Cienc., 37 (1): 12-16, 2013. ISSN 0370-3908.

This place hosts rock shelters with cave paintings. The materials studied include: clays, substrates and pigment in cave painting, these materials were analyzed under various experimental techniques suitable for structure determination, thermal and morphological analysis. To determine the basic composition the X-ray fluorescence energy dispersive (XRFED) was used. This is versatile, fast and nondestructive sampling technique used in archeological field, because it uses little sample and is not invasive. For identification of the clays, the technique of X-ray Diffraction (XRD) is employed in order to demonstrate the present phases. To observe the thermal behavior two methods were applied, differential scanning calorimetry (DSC) and thermal gravimetric analysis (TGA). These two techniques allow determining any event associated with a change in thermal properties of a material with respect to temperature or time. Finally in the morphological analysis, the study of grain size to the clay fraction was performed by scanning electron microscope (SEM).

Keyword: Rock art, pigment, characterization techniques.

RESUMEN

Este trabajo realiza un estudio de materiales en el Parque ecológico la Poma ubicado en Soacha-Cundinamarca este lugar alberga abrigos rocosos con pinturas Rupestres. Los materiales que se estudiaron son: arcillas, sustratos y pigmento en Pintura Rupestre estos materiales se analizaron bajo varias técnicas experimentales adecuadas para la determinación estructural, análisis térmico y morfológico. En cuanto composición básica para ello se utilizo la fluorescencia de rayos X por energía dispersiva (EDXRF) es una técnica de muestreo versátil,

* Grupo de Física de Nuevos Materiales, Departamento de Física, Universidad Nacional de Colombia - A.A. 5997, Bogotá D.C, Colombia. E-mail: shidalgof@unal.edu.co.

rápida y no destructiva utilizada en el campo arqueológico ya que se utiliza poca muestra y no es invasiva, para la identificación en la arcillas se aplico Difracción de rayos X(DRX) para evidenciar las fases presentes, para ver el comportamiento térmico se aplicaron dos métodos la calorimetría diferencia de barrido (DSC) y análisis Termogravimétrico (TGA) estas dos técnicas permite determinar cualquier tipo de evento asociado a un cambio de propiedades térmicas de un material respecto a la temperatura o al tiempo, para la parte de morfología realizamos estudio de tamaño de grano a la fracción arcilla.

Palabra clave: Arte rupestre, pigmento, técnicas de caracterización.

1. Introduction

The characterization of materials in artistic representations presents a great difficulty, due to the raw materials employed in their elaboration and degradation processes, which may lead to a large number of substances. Also, the historical value usually associated to samples from artistic origin imposes reserves about the amount of available sample for study,

The study of cave paintings has been focused on understanding the forms and figures represented and the relationships that these keep with a general set of symbols, in which there is an interest in the meaning and forms represented. The Archaeometric analyzes done in these paintings do not evidence in depth aspects as raw materials used and processes performed.

Knowing this information about composition and manufacturing processes of material allows to the obtained information be associated with other already archaeological events ocurred. In addition the results obtained under the techniques which pigment is studied, will guide the conservation and restoration of cave paintings. As it is necessary, in principle, conceiving the cave paintings on a broader concept of integrity in other scientific disciplines. Likewise, it is considered that the way to make plans of preservation of the pictographs is to advance in the characterization studies of the pigments.

In Latin America are still incipient studies on the application of characterization in cave paintings. Some few reported in scientific literature, as developed in the archaeological and physicochemical study of cave paintings in Hob. Which aims to present new evidences of cave representations and nondestructive techniques used on some samples [1].

The research on materials, laboratories and relationships that can be seen in these fields are quite scarce. Only recently a report has been done in this field. The GIPRI's work has become a pioneer in the development of this research. Specifically the work of Judith Trujillo Tellez. This thesis titled Paintings Archaeometry: "La Piedra de La Cuadricula" is the first work developed in archaeometric analysis of the cave paintings of cundiboyacense plateau in infrared spectrometry laboratories of the National Museum of Natural History in Paris [2].

2. Experimental details

In this paper we study samples of clay materials from Ecological Park La Poma, whose geographical coordinates are 4° 31'56 .74" N and 74 ° 16'49 .08" W respect to Bogota at a height of 2600 meters. In this place several rock shelters are found along with paintings. This article will include results of some samples as a pigment and substrate rock, collected on a rock shelter called the Grid stone see Figure 1, which is located in the inside the park.

Figure 1. Photographs Grid stone wall the Poma Park.
Source: Researchers o frock art in Colombia.

Samples were taken following the protocols of sampling of rupestre sites. This indicates extract small rock samples to not affect the rock panel, 6 samples were taken from different materials, three of them are clays of the area denoted in the paper like (M1 , M2, M3) with different colors and textures, one rock fragment the grid stone (rock) and one of paint not exceeding 2 cm ^{2} denoted (pigment), the GIPRI group in an field trip several years ago found a reddish rock that also link to the study as a possible candidate for pigment raw material (M5).

2.1. *Techniques*

Fluorescence Spectrometer for X-ray, has been developed especially for mineral analysis in the field and other industrial and scientific applications.

Some characteristics of X-ray fluorescence portable (XRF) analysis make it an ideal method for researching of cultural relics and archaeological finds. Therefore, it has become a standard method used in archeometry. Paintings, manuscripts, ceramics, metalwork, glass, and many other objects are analyzed in order to recognize their materials, production technologies and origin, and to identify counterfeit [3], for this technique all samples were studied.

Thermogravimetry (TG) was used to determine the loss mass experienced by the solid sample subjected to the action of temperature. Furthermore, to determine the endothermic and exothermic reactions the differential scanned calorimetry was used (DSC), for the study a differential scanning calorimeter was used, TA Instruments DSC Q100, whose the temperature accuracy is ± 0.05°C previously calibrated with a Indian standard, an atmosphere of nitrogen was used with a controlled flow of 50ml/min.

The XRD analysis helped to characterize and quantify the mineral phases present in the samples of clays, there are two methods of XRD: Powder Method, used to make a characterization and quantification of mineral phases in general, and the aggregate oriented method, used to make a good characterization and semi-quantification of clay mineral phases, the X-ray diffraction analysis was performed with analytical X'Pert PRO MPD diffractometer, located in the department of Physics at the National Unive rsity. diffractograms were analyzed using X'Pert HighScore.

Before applying the technique of clay for samples oriented XRD, in some cases it is necessary the cleaning and preconcentration of the clays present in the sample [4].

These preparatory steps are briefly described below.

- Treatment with acetic acid to remove carbonates: It may be necessary to dissolve the carbonates in some limestones and sediments before the clay minerals can be identified.
- Removal of organic material with hydrogen peroxide: The presence of organic compounds, which causes a large hump in the diffraction patterns of powder X-ray, can obscure the maximas of diffraction of the mineral species.
- To prepare oriented aggregates of the fine fraction, the total sample is treated by homogenization and dispersion with distilled water. Then the fine fraction is separated by decantation recovering the finest fraction to verify particle size which is what we used to prepare oriented aggregates, we used the scanning electron microscope (SEM).

3. Results and discussion

3.1. *X-Ray Fluorescence*

The X-ray fluorescence, shows a high content of oxides of Aluminum and Silicon, as shown in Table.1 and 2. Lower values than 1% were not taken into account because their low percentage of concentration.

Table 1. Chemical element by X-Ray Fluorescence and concentration percentagesin clay sample M1, M2, and M3.

	Percent concentration (%)		
Compuesto / Elemento	**M1**	**M2**	**M3**
Si02	68,78	52,92	47,44
TiO2	-	1,10	0,94
Al203		25,81	26,79
Fe2O3	4,00	7,79	7,65
K20	2,05	-	-

Table 2. Chemical elements and percent concentration in samples (M5), substrate and pigment, Portable x-ray Fluorescence.

		Percent concentration (%)		
Element	**Symbol**	**M5**	**rock**	**Pigment**
Silicon	Si	-	24,33252	4,52926
Potassium	K	-	-	-
Calcium	Ca	1,71633	-	7,61755
Titanium	Ti	0	7,3547	-
Iron	Fe	98,28366	12,73902	75,56346
Strontium	Sr	-	18,6709	6,42859
Nickel	Ni	-	12,56221	-
Zirconium	Zr	-	24,34061	5,86111

For the pigment, the substrate and the M5 sample, the portable X-ray fluorescence technique was applied. In the pigment an iron (Fe) and zirconium (Zr) were found as potential chromophores. On the other hand for the substrate, elements such as silicon (Si) and zirconium (Zr) were found in equal proportions.

3.2. *Analysis Thermal*

The results of TG and DSC analysis are presented in Figure 2 and 3, they evidence similar peaks in the two studied clays, the DSC chart between (8.01°C and 9.54°C) is obser-

ved respectively, and a second endothermic peak common to all clays, between 138.61 °C and 122.89 ° C, both peaks are caused by the loss of hygroscopic or free water. This loss of water is also reflected in the thermogravimetric curves for the marked loss weight and these result from the loss of hygroscopic or free water [5], this water loss is also reflected in the thermogravimetric curves, for the marked weight loss as shown in Table 3, mass loss on clay is very small, they are thermally stable, in the M5 sample the mass loss is minimal and no marked losses.

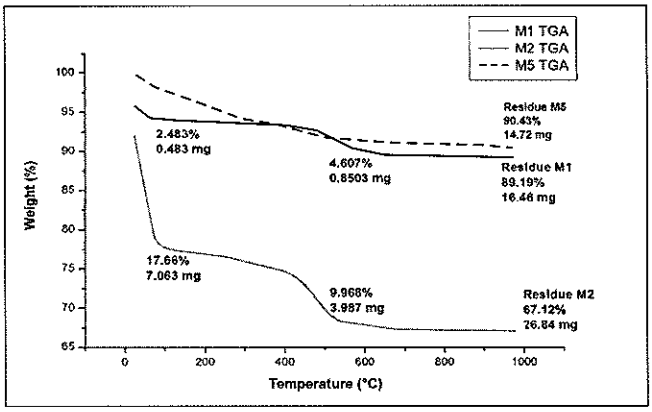

Figure 2. Graphical mass loss for the (TGA) M1 and M2.

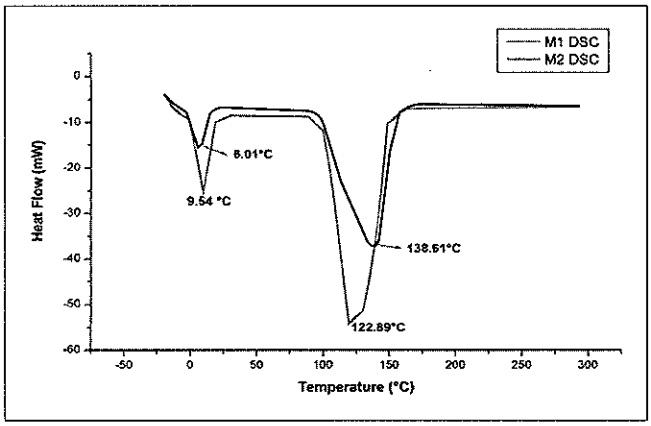

Figure 3. Scanning calorimetry differences (DSC) M1 and M2.

Table 3. Percent of mass loss between O°C y 1000°C.

Mass	Mass initial (mg)	Mass loss (%)	Residue (mg)	Residue (%)
M1	18,456	10,81	16,46	89,19
M2	39,993	32,88	26,84	67,12
M5	16,283	5,57	1,563	90,43

3.3. *Analysis granulometric*

The obtained results for the various fractions in table 4 are given. Product average values are shown for chemical treatments performed. The counting was done in the Image J. Processing and Analysis Imagen is a public domain software, As noted, the samples M1, M2, M3 and M5 has an average value between 0.390µm- 0.559µmwhich corresponds to a clay fraction, Becomes effective chemical treatment processes carried out for the removal of impurities to find the fraction clays.

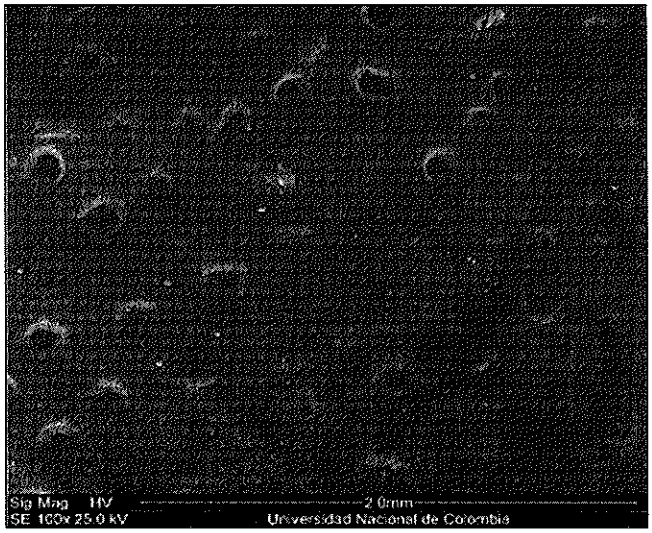

Figure 4. Clay Fraction M1, SEM image taken by.

Table 4: mean, standard deviation SD, Maximum, Minimum and all elements studied.

Date	Mean	SD	Minimum	Size
M1	3,93E-04	2,33E-03	1,59E-06	1343
M2	4,93E-04	1,83E-03	1,61E-06	2267
M3	5,59E-04	2,90E-03	1,61E-06	1937
M5	0,00409	0,00331	0,00178	1789

3.4. *Analysis X-ray diffraction*

X-ray diffractograms obtained for samples M1 are presented in Figure 5, based on these, one can identify the majority and minority phases which compose each of the clays, for powder samples, the clay glycol treated, and process temperature 350°C and 550°C.

The analysis took into account the higher mineral phases of the sample, in the samples studied these are: a high content of Quarzo Si O_2, Kaolinita ($Al_2Si_2O_5(OH)_4$), Hematita (Fe_2O_3) y Aluminum Phosphate (PO_4).

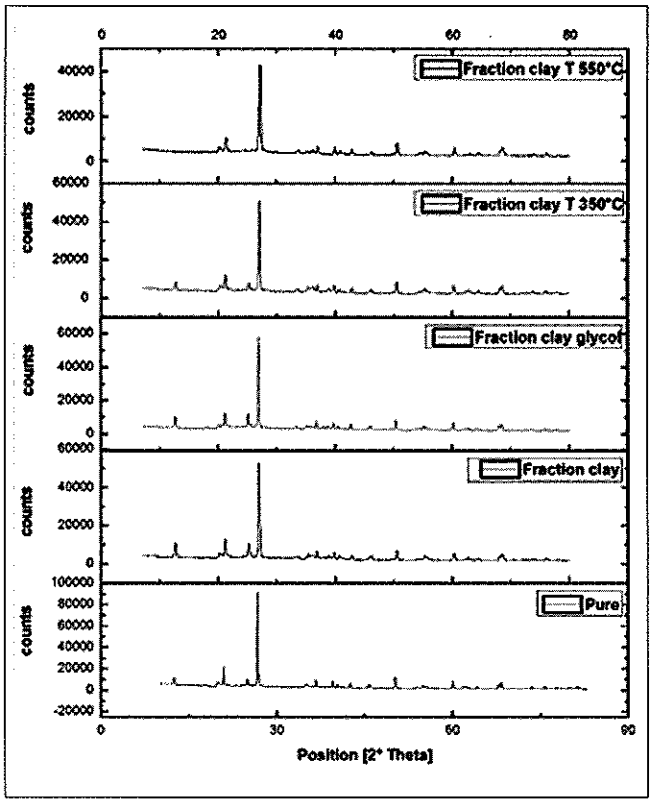

Figure 5. X-ray diffraction shows M1 powder sample, treated with glycol temperature 350 ° C and 550 ° C.

Table 5. Phase percent in samples clay treated..

	Quarzo (%)	Kaolinite (%)	Anastase (%)	Aluminium phosphate (%)	Hematita (%)
M1	31	11	1	56	1
M1 sin glicol	57	33	-	6	3
M1 con glicol	20	28	8	41	3
350 C	25	20	4	43	8
550 C	31	30	4	33	2
M2	58	36	-	-	5
M2 sin glicol	26	68	4	-	3
M2 con glicol	37	56	7	-	-
M3	37	56	7	-	-
M3 sin glicol	12	84	3	-	-
M3 con glicol	11	83	6	-	-
M5	20	-	-	21	59

4. Conclusions

The clays studied under the x-ray fluorescence technique shows the presence of oxides of Si and Al. This matches with majority mineral phases exhibited in the X-ray diffraction, These two techniques in the sample M5 presents greater amounts of iron oxides.

The x-ray fluorescence Portable technique showed a great advantage in the study of pigment and substrate, since allowed to identify separately its composition without damaging the sample, the use of this technique resulted very useful because the amount of sample studied was very small and has great wear. The presence of iron oxide in the clay and the pigment are associated like responsible for its reddish color.

Clay samples analyzed under the DSC and TGA thermal techniques exhibit thermal stability, this is evidenced by the low mass loss also associated with hygroscopic water loss.

Acknowledgements:

This work was partially supported by DIB (Hermes code 13893) and "Patrimonio Autónomo Fondo Nacional de Financiamiento para la Ciencia, la Tecnología y la Innovación Francisco José de Caldas" Contract RC-No.0850-2012.

References

[1] **H. Yacobaccio, M. Catá, P. Solá y M. Alonso**, Estudio arqueológico y fisicoquímico de pinturas rupestres en Hornillos 2 (Puna de Jujuy), Estudios Atacameños Arqueología y Antropología Surandinas, 36 (2008), pages 5-28.

[2] **J.Trujillo, Arqueometría de Pinturas Rupestres**: La Piedra de La Cuadricula, Soacha, Cundinamarca, Universidade de tras-os Montes e Alto Douro, para optar el título de Maestría en Arqueología, Prehistórica y Arte Rupestre, (2008).

[3] **L. Musílek, T. Cechák, T. Trojek**, X-ray fluorescence in investigations of cultural relics and archaeological finds Original Research Article Applied Radiation and Isotopes, Volume 70, Issue 7, July 2012, Pages 1193-1202.

[4] **J. Poppe, V.F. Paskevich**, Geological Survey Open-File Report 01-041, consultada (marzo 2013), http://pubs.usgs.gov/of/2001/of01-041/.U.S.

[5] **C.M.F. Vieira, R. Sánchez, and S.N. Monteiro**. Characteristics of clays and properties of building ceramics in the state of Rio de Janeiro, Brazil, Construction and Building Materials, 22, Issue 5, 781-787, 2008.

SPIN POLARIZATION RESONANT TUNNELING WITH DRESSELHAUS AND RASHBA SPIN-ORBIT COUPLING IN THE PRESENCE OF HYDROSTATIC PRESSURE AND THE MAGNETIC FIELD

TUNELAMIENTO RESONANTE ESPIN-POLARIZADO CON ACOPLAMIENTO ESPÍN-ÓRBITA DE DRESSELHAUS Y RASHBA EN PRESENCIA DE PRESIÓN HIDROSTÁTICA Y CAMPO MAGNÉTICO

J. A. Zúñiga[*], S. T. Pérez-Merchancano[**], H. Paredes Gutiérrez[***]

ABSTRACT

J. A. Zúñiga, S. T. Pérez-Merchancano, H. Paredes Gutiérrez: Spin polarization resonant tunneling with Dresselhaus and Rashba spin-orbit coupling in the presence of hydrostatic pressure and the magnetic field. Rev. Acad. Colomb. Cienc., 37 (1): 17-21, 2013. ISSN 0370-3908.

Whereas electron transport through spin polarization has a high potential for applications of electronic devices, making relevant the study of the physical effects inherent to the spin; are shown with this work theoretical results which allow investigations done about possible optimal heterostructures for spin filter manufacturing. The spin polarization is analyzed using the resonant tunneling on a double potential barrier considering the semiconductor heterostructure of GaAs/$Ga_{1-x}Al_xAs$/GaAs. The physical-mathematical model presented includes the interaction of coupling of the spin type: k^3-Dresselhaus and Rashba in the barriers, Rashba before and after them and Dresselhaus in the well. In addition all the heterostructure is subjected to a constant magnetic field and hydrostatic pressure (PH); because of these additional effects, the model also considers the g factor of Landé as function of the PH. The estimates obtained for the spin polarization is in function of the energy applied to the electron, the magnetic field and fixed PH.

Key words: Spin polarization, Dresselhaus and Rashba Spin-orbit coupling, Spin filters.

RESUMEN

Considerando que el transporte electrónico mediante la polarización de espín tiene un alto potencial en aplicaciones de dispositivos electrónicos, haciendo relevante el estudio de los efectos físicos inherentes al espín;

[*] Grupo de Semiconductores y Nuevos Materiales, Departamento de Matemáticas, Universidad del Cauca, Popayán, Colombia. Email: jazuniga@unicauca.edu.co

[**] Grupo de Semiconductores y Nuevos Materiales, Departamento de Física, Universidad del Cauca, Popayán, Colombia.

[***] Escuela de Física, Universidad Industrial de Santander, Bucaramanga, Colombia.

se muestran con este trabajo resultados teóricos que permiten realizar investigaciones sobre posibles heteroestructuras óptimas para la fabricación de filtros de espín. La polarización de espín se analiza mediante el tunelamiento resonante en una doble barrera de potencial considerando la heteroestructura semiconductora de $GaAs/Ga_{1-x}Al_xAs/GaAs$. El modelo físico-matemático que se presenta incluye la interacción de acoplamiento de espín tipo: k^3-Dresselhaus y Rashba en las barreras, Rashba antes y después de ellas y Dresselhaus en el pozo. Además toda la heteroestructura es sometida a campo magnético constante y a presión hidrostática (PH); debido a estos efectos adicionales, el modelo también considera el factor g de Landé como función de la PH. Los cálculos obtenidos para la polarización de espín está en función de la energía aplicada al electrón, el campo magnético y PH fijas.

Palabras clave: Polarización de espín, Acoplamiento espín orbita Dresselhaus y Rashba, Filtros de espín.

1. Introduction

Most of proposals for the spintronic devices are sometimes spin polarized transport through interfaces in various hybrid structures. Structures of double resonant barrier are not only rich in physics but also useful for various device fabrications. To determine the viability of the devices in mention is essential to answer questions of how to transport and detect spin polarized and how keeping its spin polarization over a relatively long time. Schmidt et al. proposed that the conductivity mismatch of metal and semiconductor structure causes a fundamental obstacle for electrical injection in ferromagnetic semiconductor [1]. As a result, Rashba uses tunneling contact at the interface of semiconductor and metal [2]. Sun et al. Polarized spin current generated in the semiconductor by the effect Rashba coupling [3,4].

On this work is presented a theoretical study to analyze the efficiency of polarization in any heterostructure type of double-barrier through spin orbit coupling k^3-Dresselhaus (DSOC) given on the crystalline structure zinc-blende type, which generates a breaking of reversal symmetry (BIA) [5], present in the barriers and well that are generated by the heterostructure as $GaAs/Ga_{1-x}Al_xAs/GaAs$ and coupling in the plane Rashba (RSOC) that is generated by the rupture of structural inversion symmetry (SIA) [6] in the barriers [7] before and after them.

2. Method

For the analysis of the electron tunneling, initially is considered a wave vector $k=(k_{\|},k_z)$ through a system of dual potential barrier of symmetrical of height $V_{0,P}$ generated by a heterostructure type $GaAs/Ga_{1-x}Al_xAs/GaAs$ which grows along z on the direction [001]; the components $k_{\|}$ and k_z are also wave vectors, the first in the plane of the barrier and the following is a component normal to the direction of tunneling. In fact, $k=(k_{\|}Cos\varphi, k_{\|}Sen\varphi, k_z)$ where φ is the polar angle of the wave vector k in plane xy. The calculation of the spin polarization and the probability of tunneling for the spin up and down under the DSOC and RSOC, considering effects of magnetic field and hydrostatic pressure, is based the Hamiltonian:

$$\hat{H}=-\frac{\hbar^2}{2m_P^*}\left(k_z^2+k_{\|}^2\right)+V_P(z,x)+\hat{H}_{SO} \quad (1)$$

Where m_P^* is the effective mass in function of the PH, $V_P(z,x)$ is the potential of the heterostructure that dependent on concentration of Al and of the PH by ref. [8,9], and $\hat{H}_{SO}$ is the Hamiltonian effective dependant of the spin, which is the addition of the spin orbit interaction k^3-Dresselhaus $\hat{H}_D=\beta_D\left(\hat{\sigma}_x k_x-\hat{\sigma}_y k_y\right)k_z^2$, the term in the plane Rashba $\hat{H}_R=\alpha_R\left(\hat{\sigma}_x k_y-\hat{\sigma}_y k_x\right)$ and the contribution of the magnetic field given by Zeeman $\hat{H}_z=\frac{1}{2}g_P^*\mu_B\left(\hat{\sigma}\cdot\vec{B}\right)$ [5,6,7,10]. Where β_D y α_R are constants characteristic of each material, $\hat{\sigma}=(\hat{\sigma}_x,\hat{\sigma}_y,\hat{\sigma}_z)$, with $\hat{\sigma}_i$ as the matrices of Pauli, k_i the components of the electron wave vector, g_P^* corresponds to factor of Landé effective in function of the PH, μ_B is the magneton of Borh and $\vec{B}=(BCos\theta, BSen\theta, 0)$ magnetic field orientation.

To solve the equation of Schrödinger-Pauli $\hat{H}_{b,w}\hat{\psi}=E\hat{\psi}$ generated by the expression (1) requires that the wave function $\hat{\psi}$, and disengaged for the effects of spin and magnetic field, for this considered the spinors of Dresselhaus $\hat{\chi}_{\pm}^D$ and the Zeeman $\hat{\chi}_{\pm}^B$, which are supplementary [10,11] and allow diagonalize the Hamiltonians that relate, a function $u=u(z)$ which describes the behavior of the electron on the tunneling direction and a plane wave parallel to the plane of the barrier $exp[i\vec{k}_{\|}\cdot\vec{\rho}]$ where $\vec{\rho}$ is a vector in the plane of the barrier given by $\vec{\rho}=(x,y)$, accordingly must be $\hat{\psi}=\hat{\chi}_{\pm}^D u_{\pm}(z)exp[i\vec{k}_{\|}\cdot\vec{\rho}]$.

Under the considerations of the wave function $\hat{\psi}$, the function u_{σ}, where $\sigma=\pm$ makes reference to the spin states up "+" and spin down"−", is defined by the expression:

$$\begin{cases} A_\sigma^L exp\left[i\kappa_{\sigma,1}z\right]+B_\sigma^L exp\left[-i\kappa_{\sigma,1}z\right] & si \quad -a_L < z \\ C_\sigma^L exp\left[\rho_\sigma z\right]+D_\sigma^L exp\left[-\rho_\sigma z\right] & si \quad -a_L < z < 0 \\ E_\sigma exp\left[i\kappa_{\sigma,2}z\right]+F_\sigma exp\left[-i\kappa_{\sigma,2}z\right] & si \quad 0 < z < a_w \\ C_\sigma^R exp\left[\rho_\sigma z\right]+D_\sigma^R exp\left[-\rho_\sigma z\right] & si \quad a_w < z < a_w + a_R \\ A_\sigma^R exp\left[i\kappa_{\sigma,1}z\right]+B_\sigma^R exp\left[-i\kappa_{\sigma,1}z\right] & si \quad z > a_w + a_R \end{cases} \quad (2)$$

The wave vectors $\kappa_{\sigma,1}^2$, $\kappa_{\sigma,2}^2$ and ρ_σ^2 are functions in terms of the electron energy applied to the hydrostatic pressure and the magnetic field. Determine:

Where a_L and a_R represents the width of the left and right barriers respectively, a_w the width of the well. The wave vectors $\kappa_{\sigma,1}^2$, $\kappa_{\sigma,2}^2$ and ρ_σ^2 are functions in terms of the electron energy applied to the hydrostatic pressure and the magnetic field. Determine:

$$k_{P,R,j} = \alpha_R \frac{2m_{P,j}^*}{\hbar^2} k_{\|}, \quad (3)$$

$$k_{P,D,j} = 1 \pm \beta_D \frac{2m_{P,j}^*}{\hbar^2} k_{\|}, \quad (4)$$

$$k_{P,B,j} = \frac{m_{P,j}^* g_{P,j}^* \mu_B'}{\hbar^2} B. \quad (5)$$

For $j = w, b$, which w is associated with the results given by the well and b and the barrier, is obtained:

Table 1. Wave vectors along the direction of magnetic field application.

$\theta = -\frac{\pi}{4}$	$\kappa_{\sigma,1}^2 = \rho_{P,w}^2 \pm k_{P,R,w} \pm k_{P,B,w}$	$\kappa_{\sigma,2}^2 = \frac{\rho_{P,w}^2 \pm k_{P,B,w}}{k_{P,D,w}}$	$\rho_\sigma^2 = \frac{\rho_{P,b}^2 \mp k_{P,R,b} \mp k_{P,B,b}}{k_{P,D,b}}$
$\theta = \frac{3\pi}{4}$	$\kappa_{\sigma,1}^2 = \rho_{P,w}^2 \pm k_{P,R,w} \mp k_{P,B,w}$	$\kappa_{\sigma,2}^2 = \frac{\rho_{P,w}^2 \mp k_{P,B,w}}{k_{P,D,w}}$	$\rho_\sigma^2 = \frac{\rho_{P,b}^2 \mp k_{P,R,b} \pm k_{P,B,b}}{k_{P,D,b}}$

Considering to $\rho_{P,w}^2$ and $\rho_{P,b}^2$ analogous to those defined in ref. [7, 10, 11]

For calculating the coefficients of transmission, T_σ, through the heterostructure GaAs/$Ga_{1-x}Al_xAs$/GaAs was used the standard conditions of border of Ben Daniel-Duke for the barriers of the left and right and the method of the transfer matrix for the whole system, thus obtaining an expression involving the spin up and the spin down, with the various variables specified in this work. The efficiency of spin polarization is determined by

$$P = \frac{T_+ - T_-}{T_+ + T_-} \quad (6)$$

3. Results and discussion

For the analysis of the theoretical results was considered the semiconductors of GaAlAs, $Ga_{0.70}Al_{0.30}As$ y GaAs, since they are crystal structure with constant of similar network. On consequence the relevant parameters needed for simulations involving the above materials are shown in Table 2 below.

Table 2. Parameters for the semiconductors.

	GaAlAs	$Ga_{0.70}Al_{0.30}As$	GaAs
β_D, eV A^3	19.7 [12]	18 [14]	24 [14]
α_R, eV A	0.0047 [13]	0.025 [13]	0.0873 [7]
g_P^*/g_0	−0.43 [15]	0.4 [15]	−0.44 [15]

Values are given at atmospheric pressure.

The wave vector in the plane of the barrier is fixed for all simulations $k_{\|} = 2\times10^8\ m^{-1}$ according ref. [6,7,10,11] . The thickness of the barriers are worked as $a_L = a_R = 3\,nm$ and width of well as $a_w = 8\,nm$, to $T = 80\,K$.

In Fig. 1.a) is observed that polarization given by all the conditions that this paper suggests (1) reaches 2% favoring spin down, while if only considers in the barriers the effects DSOC y RSOC (2) the polarization rises to 6% but favoring the spin up. For Fig. 1.b) Is observed greater symmetry in polarization, appearing equally in the spin inversion, of up to (2) to down in (1). This same phenomenon occurs again to only consider the effect DSOC in the well.

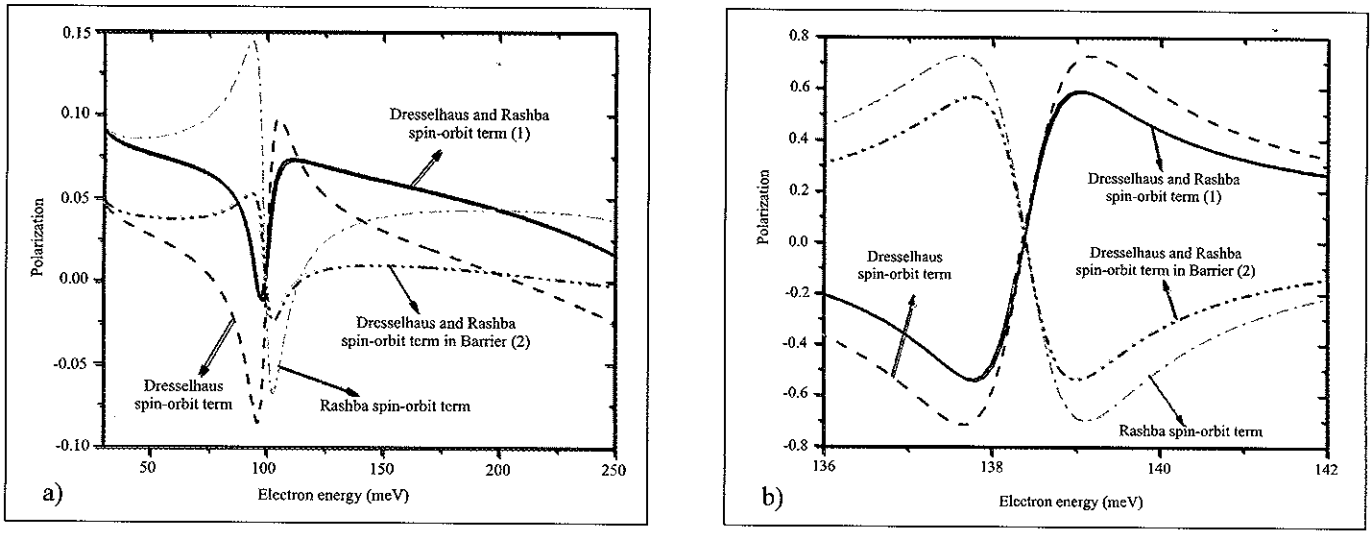

Figure 1. Spin polarization for the system double barrier of potential corresponds to the heterostructures of a) GaAs/GaAlAs/GaAs, b) GaAs/ $Ga_{0.70}$ $Al_{0.30}As$ /GaAs, depending on the energy applied, at atmospheric pressure without the presence of magnetic field.

The presence of magnetic field favors appreciably the spin up polarization in the heterostructures (2), approximately a 90% to $B = 4T$, but as HP increases spin polarization decreases helping the spin down from 10% to about 35%, as shown in Fig. 2.a), this effect can be counteracted by changing the direction of application of the field favoring the spin up from 35% to 42%. In an analogous manner behaves the heterostructure (1), but with lower efficiency.

In Fig. 2.b) is observed a balance point in a range between 7.5 to 8 Kbar approximately, where the spin polarization is invariant, which indicates that the terms involving the magnetic field in table 1 are made zero, implies in turn that the factor of Landé must be zero to GaAs and GaAlAs since this factor increases as the PH increases according to the ref. [15], likewise shows that the spin up polarization rate decreases to the balance point and then it slowly increases after him, as the magnetic field increases to the heterostructure (1), till $B = 0.5T$.

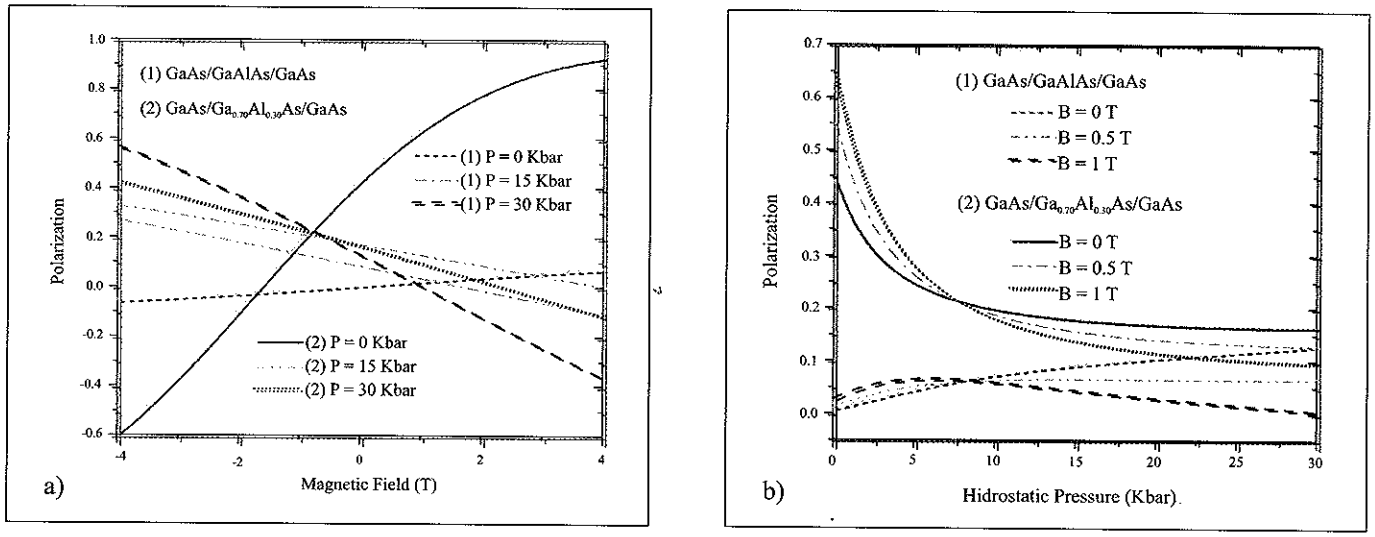

Figure 2. Spin polarization under all conditions proposed for this work. With a energy applied to the electron of $E_{(1)} = 100\,\text{meV}$ and $E_{(2)} = 140\,\text{meV}$. Is considered an initial state for the spin of $\varphi = \frac{\pi}{4}$.

4. Conclusions

The effect of moderate pressures to which they are exposed electronic devices in their construction process generated significant changes in the conduction bands in the materials that make up; situation that is reflected in the loss of spin polarization for the heterostructures in study; fact that can be largely reduced by reversing the direction of the magnetic field to consider.

For heterostructures analyzed by taking into account the effect DSOC and RSOC in the barriers prevails the spin up, but when added DSOC in the well and RSOC before and after of the barriers inversion occurs in the spin. Therefore these interactions continue encouraging the manufacturing engineering for the spin valves, based on double barriers given by non-magnetic semiconductors.

5. Acknowledgments

The Vice-rector for Research (VRI) at the Universidad del Cauca partial funding for the development of this work, through the research project ID 3088. Likewise for its academic collaboration, to the Fundación Universitaria de Popayán.

References

G. Schmidt, D. Ferrand, L. W. Molenkamp, A. T. Filip, B. J. Van Wees, "Fundamental obstacle for electrical spin injection from a ferromagnetic metal into a diffusive semiconductor", Phys. Rev. B, vol. **62**, pp. R4790-R4793, 2000.

E.I. Rashba, "Theory of electrical spin injection: Tunnel contacts as a solution of the conductivity mismatch problem", Phys.Rev. B, vol. **62**, pp. R16267-R16270, 2000.

Q. Sun, J. Wang, H. Guo, "Quantum transport theory for nanostructures with Rashba spin-orbital interaction", Phys.Rev. B, vol. **71**, pp. 165310: 1-11, 2005.

Q. Sun, X. C. Xie, "Spontaneous spin-polarized current in a nonuniform Rashba interaction system", Phys.Rev. B, vol. **71**, pp. 155321: 1-6, 2005.

V. I. Perel, S. A. Tarasenko, and I. N. Yassievich, "Spin-dependent tunneling through a symmetric barrier", Phys. Rev. B., vol. **67**, pp. 201304:1-3, 2003.

K. Gnanasekar, K. Navaneethakrishnan, "Spin-polarized resonant tunneling in double-barrier structure" Phys. E., vol. **28**, pp. 328-335, 2005.

A. John Peter, "Electron-spin polarization in a non-magnetic heterosturctre", Phys. Let. A., vol. **372**, pp. 5239-5242, 2008.

A. M. Elabsy, "Effect of the $\Gamma - X$ crossover on the binding energies of confined donors in single GaAs/Al_xGa_{1-x}As quantum-well microstructures" J. Phys. Condens. Matter., vol. **6**, pp. 10025-10030, 1994.

J. A. Zuñiga, S. T. Perez-Merchancano, L.E. Bolivar Marinez, "Tunelamiento en una doble barrera de potencial tipo Pöschl-Teller afectada por presión hidrostática", RCF., vol. **43**, pp. 812-817, 2011.

Mohammad Reza Khayatzadeh Mahani, "Influence of in-plane magnetic on spin polarization in the presence of the oft-neglected k^3-Dresselhaus spin-orbit coupling", Phys. Let. A., vol. **372**, pp. 6022-6025, 2008.

Jian-Dou Lu and Jian-Wen Li, "The effects of Dresselhaus and rashba spin-orbit intereactions on the electron tunneling in a non-magnetic heterostructure", Applied Surface Science, vol. **256**, pp. 4027-4030, 2010.

M. A. Toloza Sandoval, A. Ferreira da Silva, E. A. de Andrada e Silva, G. C, La Rocca, "Rashba and Dresselhaus spin-orbit interaction strength in GaAs/GaAlAs heterojunctions", Phys. Procedia, vol. **28**, pp.95-98, 2012.

Robert H Silsbee, "Spin–orbit induced coupling of charge current and spin polarization", J. Phys.: Condens. Matter, vol. **16**, pp. R179-R207, 2004.

Hu Li-Yun, Zhou Bin, "Spin-dependent Breit-Wigner and Fano resonances in photon-assisted electron transport through a semiconductor heterostructure", Chin. Phys. B., vol. **20**, pp. 067201:1-8, 2011.

J.R. Mejia-Salazar, "Hydrostatic pressure and coupling-barrier effects on the cyclotron effective mass and Landé g factor in GaAs-$Ga_{1-x}Al_xAs$ doublé coupled quantum wells", Phys. E., vol. **44**, pp. 1196-1201, 2012.

ELECTRICAL TRANSPORT PROPERTIES OF $Cu_2ZnSnSe_4$ THIN FILMS FOR SOLAR CELLS APPLICATIONS

PROPIEDADES DE TRANSPORTE ELÉCTRICO DE PELÍCULAS DELGADAS DE $Cu_2ZnSnSe_4$ PARA APLICACIONES EN CELDAS SOLARES

Neyder Jesús Seña*, Anderson Dussan Cuenca*, Gerardo Gordillo Guzmán.**

ABSTRACT

Seña, N.J., A. Dussan Cuenca, G. Gordillo Guzmán. Electrical transport properties of $Cu_2ZnSnSe_4$ thin films for solar cells applications. Rev. Acad. Colomb. Cienc., 37 (1): 22-26, 2013. ISSN 0370-3908.

In this work we study the electrical transport properties of $Cu_2ZnSnSe_4$ (CZTse) thin films. CZTSe thin films were prepared by PVD method; the parameters of deposition as substrate temperature (T_s) and mass, (Mx), (Mx = ZnSe, Cu) were varied for a range wide. Conductivity and resistivity measurements as a function of temperature were obtained between 120 and 400 K. It was observed, that high-temperature range above room temperature (>300 K) the carrier transport is thermally activated, with a single activation energy that changes with the variation of T_s and Mx. In the low-temperature range (<300 K), variable range hopping (VRH) was established as a predominant electronic transport mechanism for all samples. Hopping parameters were obtained by Diffusinal model and percolation theory.

Key words: Semiconductors, Electrical properties, VRH

RESUMEN

En este trabajo presentamos un estudio de las propiedades de transporte eléctrico de películas delgadas de $Cu_2ZnSnSe_4$ (CZTSe). Las películas de CZTSe fueron preparadas a través del método PVD, variando en un amplio rango la temperaturas de sustrato (T_s) y la masa (Mx), (Mx = ZnSe, Cu). Las medidas de conductividad y resistividad en función de la temperatura fueron realizadas entre 120 y 400 K. Se evidenció que para la región de altas temperaturas (>300 K) los portadores son térmicamente activados con una única energía de activación que cambia con T_s y Mx. Para la región de bajas temperaturas (<300 K), se estableció, para todas las muestras, que el mecanismo de transporte es hopping de rango variable (VRH). Se obtuvieron los parámetros hopping a partir del modelo Difusional y la Teoría de Percolación.

Palabras clave: Semiconductores, Propiedades Eléctricas, VRH

* Grupo de Materiales Nanoestructurados, Dpto. de Física, Universidad Nacional de Colombia, Bogotá. E-mail: njsenag@unal.edu.co

** Dpto. de Física, Universidad Nacional de Colombia, Bogotá

Introduction

Quaternary compounds Cu_2ZnSnS_4 (CZTS) and $Cu_2ZnSnSe_4$ (CZTSe) have attracted increasing attention as potential absorber materials for thin film solar cells. [Lechner R., Jost S., Palm J., Gowtham M., Sorin F., Louis B., Yoo H., Wibowo R. A., Hock R., 2013; Guo Q. J., Ford G. M., Yang W. Ch., Charles J. H., Hugh W. H., Rakesh A., 2012] This is due to their cheap resource, n-type conductivity, high absorption coefficient ($>10^4$ cm^{-1}), and direct band gap close to the optimum value for solar energy conversion. [Lin S., Jun H., Hui K., Fangyu Y., Pingxiong Y., Junhao Ch., 2011; Lee S. M., Mohanty B. Ch., Jo Y. H., Yong S. Ch., 2013] There are some reports in which CZTS and CZTSe thin-film have been prepared by several typical techniques, such as sol gel [Fahrettin Y., 2011], electrodeposition [Ji L., Tuteng M., Ming W., Weifeng L., Guoshun J., Changfei Z., 2012], selenization of elemental precursor [Salomé P.M.P., Fernandes P.A., Da Cunha A.F., 2009], sputtering [Brammertz G., Ren Y., Buffière M., Mertens S., Hendrickx J., Marko H., Zaghi A., Lenaers N., Köble Ch., Vleugels J., Meuris M., Poortmans J., 2013], etc.

A thorough understanding of the physical properties of $Cu_2ZnSnSe_4$ thin films is quite essential for its ultimate use as absorber in thin film solar cells; however few studies are reported on electrical and transport properties for this compound semiconductor.

In this work we present a study on electrical and transport properties of $Cu_2ZnSnSe_4$ (CZTse) thin films prepared by thermal co-evaporating method. The influence of the initial composition of the films was studied for Cu-rich, stoichiometric and Cu-poor layers, as well as also on effect of the temperature. From dark conductivity measurements performed over a wide range of temperatures, showed that above room temperature the dominant mechanism is the thermal activation of carriers. In the low-temperature range, it is between 300 and 120 K, variable range hopping (VRH) was established as a predominant electronic transport mechanism for all samples. Using classical equations from the percolation theory and the diffusional model, the density of states near the Fermi level, as well as the hopping parameters, were calculated. A correlation between the hopping parameters for both models is presented.

Experimental details

Thin films $Cu_2ZnSnSe_4$ were prepared on Soda Lime-type glass substrates through physical vapor deposition (PVD) in the presence of Se. The substrates were washed with sulphochromic solution and after cleaned with neutral PH liquid soap and followed by cleaning with deionized water in ultrasonic bath. The masses of the precursors used were between 0.104 and 0.131 g for Cu, 0.097 g for Sn, and between 0,134 and 0.171 g for ZnSe; It compounds had a high degree of purity (99.95 ± 0.05%). The deposition process was conducted in three stages. During the first stage, Cu and Se_2 were simultaneously co-evaporated at a substrate temperature of T_s(Cu) varying between 573 and 773 K. This stage formed the Cu_2Se composite, as a result of the reaction of the two precursors. During the second stage (in situ), Sn and Se were simultaneously co-evaporated, maintaining T_s(Sn) = 523 K; this stage formed the $SnSe_2$ composite, which in turn reacted with Cu_2Se to give way to the formation of the Cu_2SnSe_3 ternary composite. During the third stage (in situ), ZnSe was evaporated varying T_s(ZnSe) between 573 and 773 K. The final reaction gave way to the formation of the $Cu_2ZnSnSe_4$ quaternary composite. The successive reactions during thin films deposition by PVD method allowed obtaining of the CZTSe compound with characteristic phase. [Seña N., 2013] These reactions occurring have been considered by other researchers in the fabrication of the composite. [Redinger A., Mousel M., Djemour R., Gütay L., Valle N., Siebentritt S., 2013]

Dark conductivity measurements were carried using four-probe method by Van der Pauw method in equipment PPMS resistivity. The electrical current was measured with a Keithley electrometer 617 connected to a computer. The samples were annealed at 400 K and then cooled down to 120 K at a constant rate of 2 K per min. The applied field was 5mV/cm. Conductivity n type for $Cu_2ZnSnSe_4$ thin films was identified from thermo power measurements.

Results and discussion

Figure 1 shows an Arrhenius plot of the dark conductivity of the quaternary $Cu_2ZnSnSe_4$ thin films varying the mass of ZnSe compound and substrate temperature T_s(Cu).

A linear behavior is only observed in the high-temperature region, as shown in the Figure 1 (300 K < T < 400 K). In this temperature region, it is over 300 K, the transport mechanism involves carriers activated directly from levels below the Fermi level to states at the bottom of the conduction band. Fit linear for both cases is showed in the inset of Figure 1. Region for higher temperature in the sample with open squares symbols (see Figure 1 a, b) can be associated to formation of structural disorder during the characteristic phase formation of CZTSe contributing to the improvement of ionic conductivity. [Dong-Hau Kuo D., Tsega M., 2014; Yilmaz S., Turkoglu O., Belenli I., 2007] Termopower measurements (TM) are used for conduction type identification.

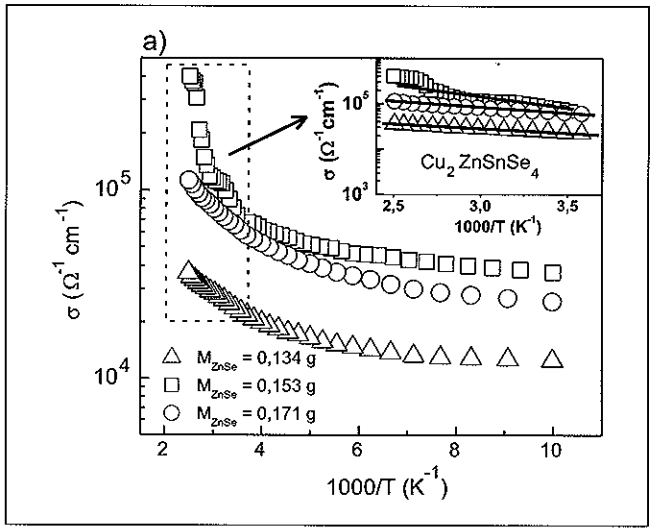

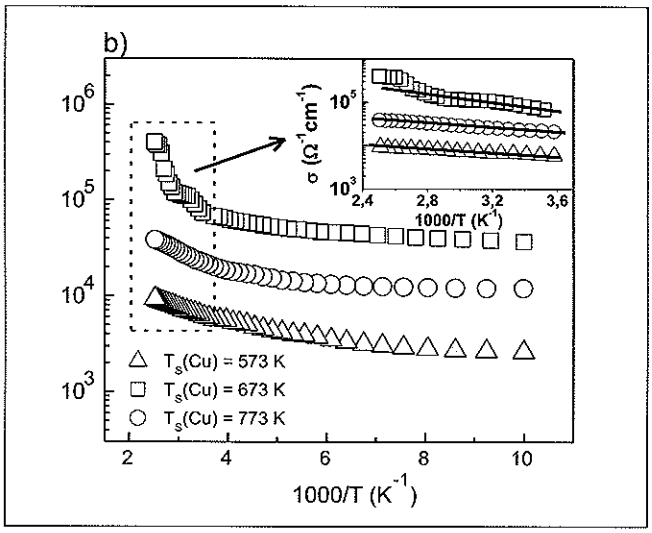

Figure. 1. Dark conductivity as a function of the inverse temperature for CZTSe samples varying a) M_{ZnSe} and b) T_s(Cu).The Figure inset shows a lineal fitting for all samples in the high-temperature range.

[Xie H., Tian C., Li W., Feng L., Zhang J., Wu L., Cai Y.,, Lei Z., Yang Y., 2010] In this case, TM were performed on all samples and it was observed, that conductivity is n-type. Being the conductivity an exponential function of the activation energy, small changes in the Fermi level will result in large variations of σ_{dk}, as it can be seen in Fig. 1. The activation energies, E_a, are reported in the table 1.

Table 1. Activation energies calculated from dark conductivity measurements for the CZTSe samples varying the M_{ZnSe} and T_s(Cu).

MZnSe (g)	TS(Cu) (K)	Ea (eV)
0.134	673	0.020
0.153		0.072
0.171		0.014
0.117	573	0.021
	673	0.072
	773	0.014

Quaternary phase, without binaries phases was obtained with 0.118 g for Cu, 0.097 g for Sn, and 0.151 g for ZnSe; temperatures for Cu, Sn and Se were 673, 523 and 673, respectively.

From Table 1 it's observed that increasing the substrate temperature, T_s(Cu), from 573 K to 673 K evidence an increase in the activation energy of the material, therefore an increasing substrate temperature favors the formation copper bonds on surface, as thus the reducing on charge trapping centers, structural dislocations and the breaking bonds at crystal lattice. When the substrate temperature rises again from 673 K to 773 K is evidenced a drop in the value of the activation energy and the conductivity, this can be attributed to the fact that possibility, at these temperatures the copper was re evaporated showing thus a shortage of carriers.

On the other hand, in the case of the variation of M_{ZnSe}, the behavior observed in the curves is similar to that described above, except that the increase in conductivity is associated with increased presence of Cu atoms participating in the electric conduction.

Since the Arrhenius plot does not fit at low temperatures (See Figure 1) and then, other possible transport mechanisms were sought. In Figure 2, the variation of dark conductivity versus $1/T^{1/4}$ is shown.

It is observed, that at low temperatures, the lineal fitting is very good giving a correlation according to Mott's equation. [Mott N. F. (1969)] (See Figure 2)

$$\sigma = \sigma_0^* e^{(\frac{T}{T_0})^{1/4}} \quad (1)$$

The percolation theory has been widely used to study transport phenomena in semiconductors, in particular to calculate the hopping parameters of Mott's equation for the case of VRH; however, these parameters are improved by Diffusional model. [Dussan A., Buitrago R. H., 2005] In this last model, is assumed that the density of states is constant in a range

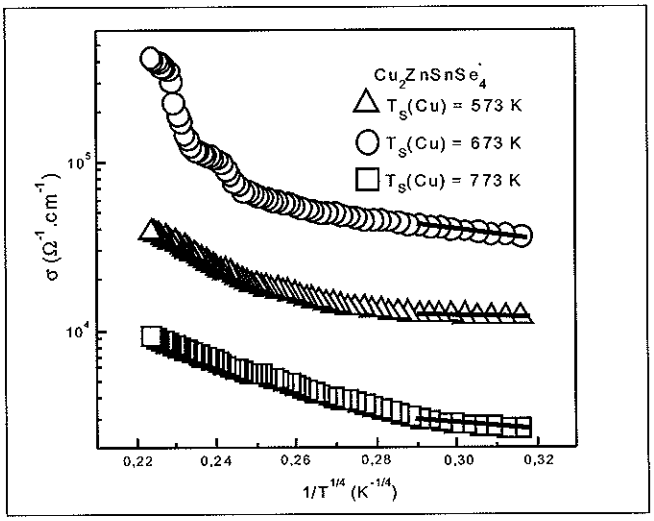

Figure 2. Dark conductivity as a function of $T^{1/4}$ for CZTSe samples varying T_s(Cu).

of some k_BT around the Fermi energy, and the latter is within the localized states, then for the three-dimensional case, the number of states per unit volume and energy (N_{Fermi}), separated by a hopping distance R_{hopp}, is related to the energy difference between hopping states as W_{hopp}.

Table 2 shows the results for the hopping parameters R_{hopp} and W_{hopp}, calculated from the diffusional model at a temperature of 150 K. The density of states at the Fermi level, N_{Fermi}, was calculated.

Table 2. Values of W_{hopp} and R_{hopp} for T = 150 K in samples CZTSe varying the substrate temperature during the evaporation of Cu. Calculating $N(E_{Fermi})$ we assumed c = 2.0, γ= 257 Å [Thamilselvan M., Premnazeer K., Mangalaraj D., Narayandass S. K., 2003]

$Cu_2ZnSnSe_4$ TS(Cu) (K)	$N(E_{Fermi})$ ($cm^{-3}\cdot eV^{-1}$)	Diffusional Model	
		R_{hopp} (cm)	W_{hopp} (eV)
573	$7.11x10^{20}$	$6.22x10^{-7}$	0.01
673	$3.40x10^{18}$	$2.36x10^{-6}$	0.05
773	$3.87x10_{19}$	$1.28x10^{-6}$	0.02

Values of W_{hopp} and R_{hopp} are in agreements with the basic initial assumption that the density of states was constant around the Fermi level, and that the jumps of the carriers from one state to the other were only of the order of some k_BT.

Conclusion

Dark conductivity measurements performed over a wide range of temperatures for CZTSe samples were investigated. It was found that for temperatures higher than 300K the dominant mechanism is the thermal activation of carriers. The different activation energies found were obtained in terms of presence of Cu in the material. In the low-temperature ranges, the main transport mechanism is the VRH. From the diffusional model and using experimental data W_{hopp} and R_{hopp} were calculated.

Acknowledgments

This work was supported by Universidad Nacional de Colombia - DIB. We thank the Semiconductor Materials and Solar Energy Group for Laboratory support in sample preparation.

References

Brammertz G., Ren Y., Buffière M., Mertens S., Hendrickx J., Marko H., Zaghi A., Lenaers N., Köble Ch., Vleugels J., Meuris M., Poortmans J., 2013. Electrical characterization of $Cu_2ZnSnSe_4$ solar cells from selenization of sputtered metal layers. Thin Solid Films 535: 348-352.

Dussan A., Buitrago R. H., 2005. Transport mechanism in lightly doped hydrogenated microcrystalline silicon thin films. J. Appl. Phys. 97: 1-5.

Fahrettin Y., 2011. Nanostructure Cu_2ZnSnS_4 thin film prepared by sol–gel for optoelectronic applications. Sol. Energy 85: 2518-2523.

Guo Q. J., Ford G. M., Yang W. Ch., Charles J. H., Hugh W. H., Rakesh A., 2012. Enhancing the performance of CZTSSe solar cells with Ge alloying. Sol. Energy Mater. Sol. Cells 105: 131-136.

Ji L., Tuteng M., Ming W., Weifeng L., Guoshun J., Changfei Z., 2012. Appl. Surf. Sci. 258: 6261–6265.

Kuo D. H., Tsega M., 2014. The investigation of $Cu_xZnSnSe_4$ bulks with x = 1.4–2.2 for debating the Cu excess and Cu deficiency used in thin-film solar cells. Mater. Res. Bull. 49: 608–613.

Lechner R., Jost S., Palm J., Gowtham M., Sorin F., Louis B., Yoo H., Wibowo R. A., Hock R., 2013. $Cu_2ZnSn(S,Se)_4$ solar cells processed by rapid thermal processing of stacked elemental layer precursors. Thin Solid Films 535: 5-9.

Lee S. M., Mohanty B. Ch., Jo Y. H., Yong S. Ch., 2013. Phase development, microstructure and optical properties of $Cu_2ZnSnSe_4$ thin films modified with Pb and Ti. Surf. Coat. Technol. 231: 389-393.

Lin S., Jun H., Hui K., Fangyu Y., Pingxiong Y., Junhao Ch., 2011. Structure, composition and optical properties of Cu_2ZnSnS_4 thin films deposited by Pulsed Laser Deposition method. Sol. Energy Mater. Sol. Cells 95: 2907-2913.

Mott N. F., 1969. Conduction in non-crystalline materials II. Localized states in a pseudogap and near extremities of conduction and valence bands. Philos. Mag. 19: 835-852.

Redinger A., Mousel M., Djemour R., Gütay L., Valle N., Siebentritt S., 2013. $Cu_2ZnSnSe_4$ thin film solar cells produced via co-evaporation and annealing including a $SnSe_2$ capping layer. Prog. Photovolt Res. Appl. DOI: 10.1002/pip.2324.

Salomé P.M.P., Fernandes P.A., Da Cunha A.F., 2009. "Morphological and structural characterization of Cu_2ZnSnS_4 thin films grown by selenization of elemental precursor layers", Thin Solid Films 517: 2531–2534.

Seña N., 2013. Tesis MSc: Caracterización eléctrica y estudio de las propiedades de transporte del compuesto $Cu_2ZnSnSe_4$ para ser usado como capa absorbente en celdas solares. Universidad Nacional de Colombia. Bogotá-Colombia.

Thamilselvan M., Premnazeer K., Mangalaraj D., Narayandass S. K., 2003. Field and temperature-dependent electronic transport parameters of amorphous and polycrystalline GaSe thin films. Phys. B 337: 404 - 412.

Xie H., Tian C., Li W., Feng L., Zhang J., Wu L., Cai Y., Lei Z., Yang Y., 2010. Preparation of p-type CdS thin films and in situ dark conductivity in vacuum deposited CdS:Cu films. Appl. Surf. Sci. 257: 1623–1627.

Yilmaz S., Turkoglu O., Belenli I., 2007. Synthesis of β-Phase $((Bi_2O_3)_{1-x}(Dy_2O_3)_x (0.01<x<0.10)$ System and Measurement of Oxygen Ionic Conductivity. Res. Lett. Materials Science 2007 (97204): 1-5.

STUDY OF OPTICAL PROPERTIES BIREFRINGENT OF HEMA - DR13

ESTUDIO DE LAS PROPIEDADES ÓPTICAS BIRREFRINGENTES DEL HEMA –DR13

Emmanuel Mercado Gutiérrez[*], Cesar Maestre Molinares[**], Sonia Valbuena Duarte[***], Francisco Racedo Niebles[*]

ABSTRACT

Mercado Gutiérrez, E., C. Maestre Molinares, S. Valbuena Duarte, F. Racedo Niebles. Study of optical properties birefringent of hema - DR13. Rev. Acad. Colomb. Cienc., 37 (1): 27-30, 2013. ISSN 0370-3908.

The following paper is a detailed study of the optical properties of HEMA-DR13 from optical birefringence can be induced azopolymeric material. Based on the method of two-photon absorption, anisotropy is generated due to the reorientation of the chromophores in the sample of HEMA-DR13. Using allow-power laser He-Ne, and a laser Nd-YAG medium power, it was possible to implement an optical system which allows observing the subsequent quantification of photoinduced birefringence in said material. Subsequently comparing the results obtained with different theoretical models, thereby determining the characteristic times (time of excitation and relaxation time) of HEMA-DR13. Additionally, a study of the response signal based on the excitation power and the temperature of the material being able to obtain the relationship between this variables and the intensity of birefringence.

Key words: Two-photon absorption, Photoinduced birefringence, Azocompounds.

RESUMEN

En el siguiente trabajo se hace un estudio detallado de las propiedades ópticas del HEMA - DR13 a partir de la birrefringencia óptica que se puede inducir un material azopolímerico. Basándose en el método de absorción de dos fotones, se generó una anisotropía debida a la reorientación de los cromóforos que componen la muestra del HEMA – DR13.Utilizando un láser de baja potencia de He - Ne y un láser de Nd - YAG de mediana potencia, se logró implementar un sistema óptico el cual permite observar para su posterior cuantificación de la birrefringencia foto inducida en dicho material. Posteriormente se comparan los resultados obtenidos con los diferentes modelos teóricos, determinando así los tiempos característicos (tiempo de excitación y tiempo de relajación) del HEMA – DR13. Adicionalmente se hace un estudio de la respuesta de la señal en función de la potencia de excitación y de la temperatura del material logrando obtener la relación que existe entre estas variables y la intensidad de la birrefringencia.

Palabras clave: Absorción por dos fotones, Birrefringencia fotoinducida, Azopolímero.

[*] Grupo GEOEL, Dpto de Física, Universidad del Atlántico, Barranquilla. E-mail: fran@mail.uniatlantico.edu.co

[**] Maestría Física SUE-CARIBE, Universidad de la Guajira - Colombia

[***] Grupo MATINCUC, Universidad de la Costa – Colombia

1. Introduction

The phenomenon of photo isomerization the azocompounds have been studied for several years [7] with the aim of finding ever more effective [2,3]materials and with a much faster response photosensitive, so they can be used in photonic technologies, storage and temporary[5]. That is why a study of birefringent properties of azopolymer 2-hydroxyethyl-methacrylate and 4 - [Nethyl-N-(2-methacryloxy-ethl)]-amino-2'-chloro-4'-nitro-azobenezene (HEMA - DR13) through photo isomerization reversible Trans - Cis - trans birefringence can be induced in azopolymer linearly polarized light using low power, this causes the photo orientation of the chromophores in the material causing a change in the dipole moment of these, by means of a lateral movement mechanism, now called inversion mechanism. Chromophores rotate in a free volume perpendicular to the applied external electric field. The induced birefringence is through photo isomerization Trans - Cis – Trans[1,3]. Applying an external electric field generated by a laser beam is achieved by this process.

2. Material and Methods

Synthesis HEMA DR13 samples obtained from crystallization method by solvent evaporation of two monomers which were, tris (2-hydroxyethyl) isocyanurate triacrylate (monomer A) and ethoxylated (6) Trimethylol propane triacrylate (Monomer B) acts as the first generator in material hardness, while the second is responsible for reducing the rigid clumps in the mixture, the mixture was added disperse Red 13 (DR13) which provides mobility as the photosensitive compound. The mixture was dissolved in ethanol, an inert solvent in the reaction of the monomers A, B and DR13, the mixture generated a viscous dark red and is deposited on a glass substrate subsequently processed samples were exposed to a temperature approximately 70 C in an atmosphere saturated with the same solvent. Once developed HEMA DR13 samples proceeded to perform the experimental setup which allowed induce birefringence in that azopolymer. Figure 1 shows a diagram of the experimental setup used to measure the photo-induced birefringence [3,6].

The experimental setup for measuring the birefringence comprises two lasers, laser He - Ne linearly polarized, whose wavelength is 632.8 nm and 1 mW of power, in our description we call this, the read laser and which is responsible for verifying the polarization state of the chromophores of the polymer network of HEMA - DR13. Moreover laser used a medium power Nd: YAG linearly polarized with a wavelength of 532 nm power of 100mW, this is the writing laser or laser excitation chromophores which react to the field applied electric and thereby inducing birefringence in the material. Figure 1 show the experimental arrangement used.

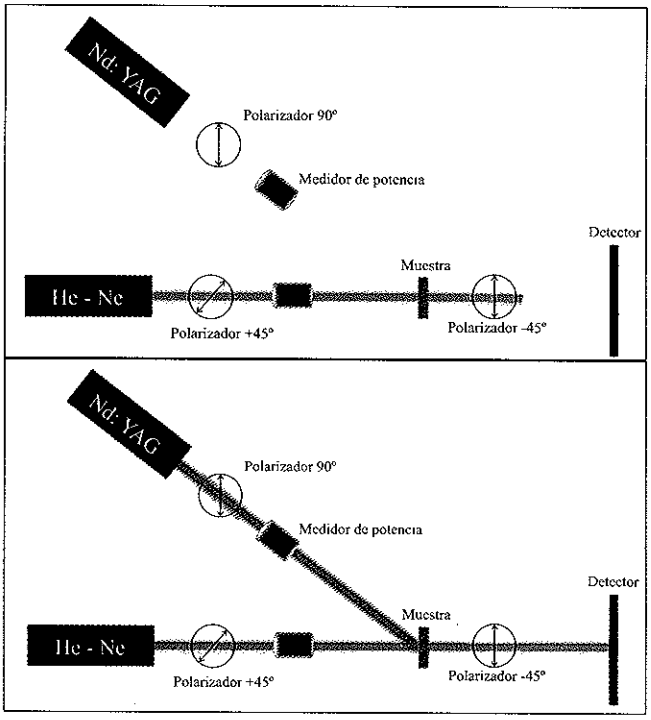

Figure 1. Experimental scheme to measure the birefringence induced in samples HEMA - DR13

Two crossed polarizers are each responsible for controlling the amount of light reaching the photodetector, sign azopolymer interposing between the two polarizers, which is verified is the state of the photo isomerization in the chromophores found in the sample (Figure 1). When the excitation laser is turned on and calibrated to a determined power, is incident on the sample, taking into account that the writing laser beam must have a polarization of 90 to the incident read laser beam. Note that this difference in the angle of the polarizers must be in a relationship of 45 to the writing laser and -45 to the reading laser. This is because chromophores exhibit a maximum in the intensity of the transmitted signal when the angle of polarization of the writing laser is 45 or -45.

The experiment was conducted at a temperature of 24C finds, which was the ambient temperature at which the experiment was developed. At the time the writing laser is not incident on the sample of azopolymer, do not get any signal from the reading laser.

3. Results

At the time of the writing laser light with a power of 4.5 mW, begins the process of photo isomerization in the sample

of HEMA - DR13. When the writing laser impinges on the material of the polymeric network chromophores begin to orient perpendicular to the external electric field by changing the dipole moment of the chromophores and thus changing the polarization state of laser beam that passes through the sample. In Figure 3, the signal is observed photoinduced birefringence for a sample of HEMA - DR13 containing 70% by weight of monomer A and 30% by weight of monomer B. The duration of the writing laser incident on the sample was 15 minutes, was withdrawn When excitation source, the duration of the signal acquisition to photo isomerization Cis - trans was also 15 minutes. In figure 3 shows an increase in the transmitted signal as chromophores change state Cis to state Trans photo isomerization the first stage of Trans - cis. Then when the chromophores are at a maximum value of

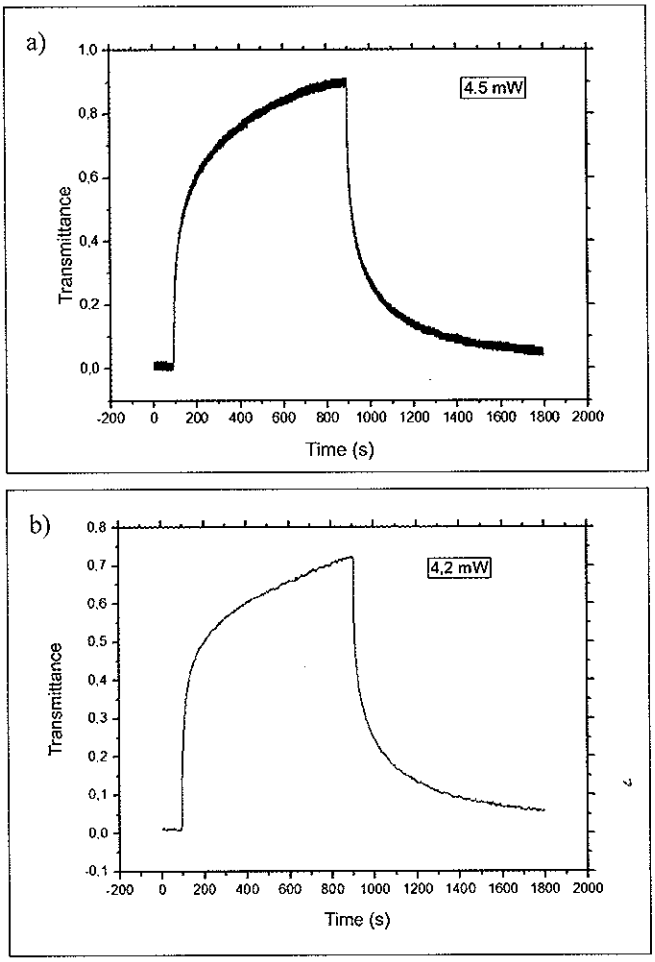

Figure 2. Photoinduced birefringence curves for the HEMA - DR13. a) Signal transmission reading laser in the process of photo isomerization Trans - Cis - Trans, for excitation power of 4.5 mW. b) Signal transmission reading laser in the process of photo isomerization Trans - Cis - Trans, for excitation power of 4.2 mW.

orientation is removed, the excitation source thermal photoisomerization starting Cis - Trans.

In the figure 2 is induced birefringence for excitation power of 4.5 mW and 4.2 mW respectively, showing the same behavior but with deference in the maximum signal obtained for each. The variation of the excitation power is shown in figure 3.

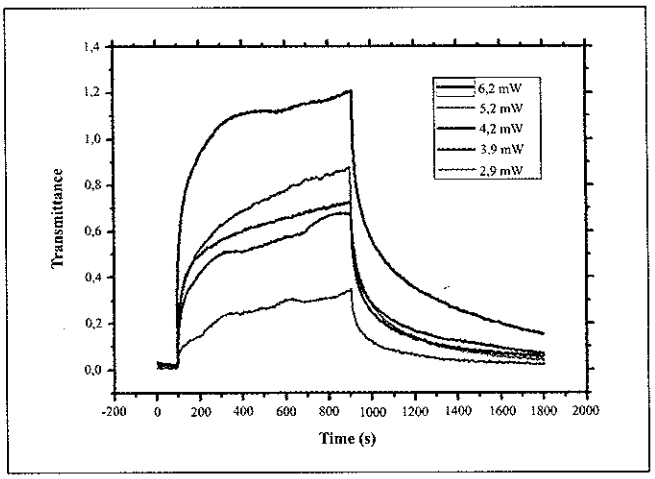

Figure 3. Curve of the induced birefringence in HEMA - DR13 for different excitation powers an Nd: YAG.

Model using the bi-exponential function, which describes the transmission of the induced birefringence as

$$T = A_f[1 - exp(-t/\tau_f)] + A_s[1 - exp(-t/\tau_s)]$$

for excitation and relaxation

$$T = A_f[exp(-t/\tau_f)] + A_s[exp(-t/\tau_s)]$$

results were adjusted experimentally to obtain the characteristic times of HEMA - DR13. Settings function model bi – exponential shown in figure 4.

Figure 4a shows the results obtained in the process of photo isomerization Trans - Cis, where the black line represents our experimental curve, while the color represent bi exponential function for different characteristic times. Then in Figure 4b shows the process that occurs when we remove the write laser, it shows the experimental curve (blackline) against bi function curve - exponential relaxation process. In Table 1 the data from Figure 4 are shown.

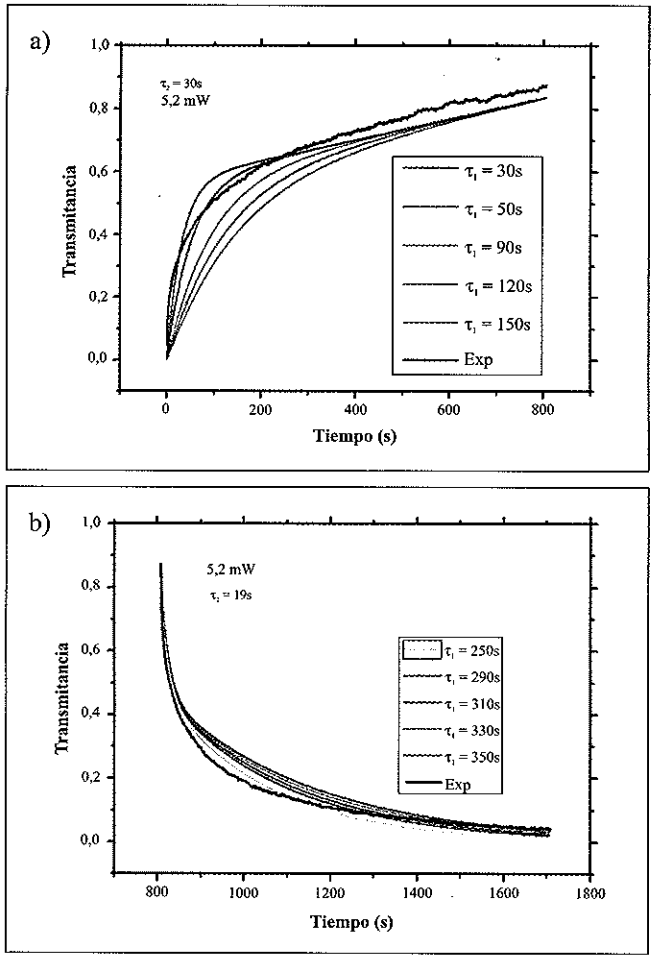

Figure 4. Show the relationship between the model function bi - exponential with theoretical curves obtained experimentally. a) Process photo isomerization Trans - Cis. b) Photo isomerization process Cis - Trans.

Table 1. Shows the parameters that describe the phenomenon of Trans Cis Trans photo isomerization, through bi function - exponential for HEMA -DR13.

	A_f	τ_f	A_s	τ_s
Excitation	0.57	30	0.3	30
Relajation	0.47	19	0.4	250

4. Conclusions

Was synthesized samples azopolymer HEMA - DR13, by the method of deposition by evaporation of the s olvent, and that the samples were of excellent quality. Additionally, an experimental setup was achieved high accuracy to obtain the curves of HEMA - DR13, so that it could make variations in the excitation power and reproduce easily bends. Further experimental data were compared with the model of the function bi - exponential, where comparing the different data and thus to obtain the characteristic times of excitation and relaxation for the HEMA - DR13. Achieving establish the model of bi exponential function as an effective model for describing the photo isomerization azoaromatics molecules. By varying the excitation power is able to observe the strong dependence of the excitation power with the birefringence induced in the material, this indicates that we can control the intensity of the signal by means of this variable. Thus allowing for the HEMA - DR13 is a photosensitive material and capacity to be used as information storage device.

References

[1] **E. Mercado Gutiérrez, et al**. Analysis of induced birefringence in microstructured PMMA films to study the phenomenon of optical storage. Opt. Pura Apl. **45(3)303-306** (2012).

[2] **Osvaldo N. Oliveira Jr. et al**. Optical storage and surface-relief gratings in azobenzene-containing nanostructured films. Advances in Colloid and Interface Science 116 pag. 179-192, (2005).

[3] **M. C. Cardoso 2005:** Estudio da Birrefringencia Fotoinduzida Por um e Dois Fotons em Compostos Azo-aromaticos da Familia Salen, Tesis de Maestría, Universidad de Sao paulo.

[4] **C. R Mendoca, D. S. et al**. Polymer **42**(2001) 6539 - 6544.

[5] **H. Rau**, in Photochemistry and Photophysics. Vol II, J.K. Rabek., Ed., Boca Raton, Florida, 1990, p. 119.

[6] **Z. Sekkat, J.**: Reorientation Mechanism of Azobenzenes within the Trans-Double-Right-Arrow- Cis Photo isomerization. Journal of Physical Chemistry 99 (1995) 17226-34.

[7] **V. Sánchez, E. Meléndez**: Química Orgánica, 2da Ed., editorial Reverte, 1984 pg 1110 - 1114.

TRANSPORT PROPERTIES OF HOT PRESSED $\beta - Zn_4Sb_3$ COMPOUNDS

PROPIEDADES DE TRANSPORTE DE COMPUESTOS $\beta - Zn_4Sb_3$ PREPARADOS POR EL MÉTODO DE PRENSADO EN CALIENTE

Mónica Morales*, Jorge I. Villa*, Julio E. Rodríguez*

Abstract

Morales, M., J. I. Villa, J. E. Rodríguez: Transport properties of hot pressed β – Zn_4Sb_3 compounds. Rev. Acad. Colomb. Cienc., 37 (1): 31-35, 2013. ISSN 0370-3908.

Single phase $\beta - Zn_4Sb_3$ samples were prepared by using hot pressing method. Their structural and morphological properties were studied by x-ray diffraction analysis (XRD) and Scanning Electron Microscopy (SEM), respectively. The transport properties were obtained from Seebeck coefficient $S(T)$ and electrical resistivity $\rho(T)$ measurements between 100 and 290K. $S(T)$ shows positive values suggesting a p-type material, its magnitude increases with the processing time, reaching maximum values close to $270\mu V/K$. The electrical resistivity measured by four D.C. probe method, increases with processing time, however its magnitude is less than $9m\Omega - cm$. We observe an order-disorder transition in the transport properties around 240K, which is a characteristic property of pure single crystals of $\beta - Zn_4Sb_3$. From $S(T)$ and $\rho(T)$ experimental data we calculate the thermoelectric power factor PF , this performance parameter reaches maximum values close to $10\mu W/K^2 - cm$, which makes this kind of compounds promising materials for thermoelectric applications.

Keywords: Zn_4Sb_3 compounds, Thermoelectric materials, Hot pressing method.

Resumen

Muestras monofásicas de $\beta - Zn_4Sb_3$ fueron preparadas por el método de prensado en caliente. Sus propiedades estructurales y morfológicas se estudiaron mediante análisis de difracción de rayos-X (DRX) y microscopía electónica de barrido (SEM), respectivamente. Las propiedades de transporte se estudiaron a partir de mediciones de coeficiente Seebeck S(T) y resistividad eléctrica $\rho(T)$, en el rango de temperatura entre 100K y 290K. S(T) muestra valores positivos sugiriendo un material tipo-p, su magnitud se incrementa con el tiempo de procesamiento alcanzando valores máximos cercanos a $270\mu V/K$. La resistividad eléctrica se incrementó con el tiempo de procesamiento. Sin embargo su magnitud fue en todos los casos menor que $9m\Omega - cm$. En las propiedades de transporte se observó una transición del tipo orden-desorden a temperaturas cercanas a 240 K, esto es una característica típica de materiales monocristalinos de $\beta - Zn_4Sb_3$. A partir de los datos experimentales de $S(T)$ y $\rho(T)$ se calculó el factor de potencia termoeléctrico PF, Este parámetro de rendimiento alcanzó valores máximos cercanos a

* Departamento de Física, Universidad Nacional de Colombia, Bogotá.

$10\mu W/K^2-cm$, lo cual convierte esta clase de compuestos en materiales prometedores para aplicaciones termoeléctricas.

Palabras clave: Compuestos de Zn_4Sb_3, Materiales termoeléctricos, Método de prensado en caliente.

1 Introduction

Over the past years, much interest has been focused on the search for new thermoelectric materials driven by the need for more efficient materials for electronic refrigeration and power generation [1, 2].

Efficient thermoelectric devices require the development of new materials that combine high thermoelectric performance, low cost and high chemical stability. The thermoelectric performance is characterized by the figure of merit, ZT. This parameter is a direct function of the transport properties and is given by the expression [3, 4]: $ZT = S^2T/\rho\kappa$, where κ is the total thermal conductivity, S the Seebeck coefficient, ρ the electrical resistivity and T the absolute temperature.
The Zn_4Sb_3 compound is a promising thermoelectric material due to its high figure of merit values, which is a result of its particular low thermal conductivity and high Seebeck coefficient values [4, 5, 6].
For Zn_4Sb_3 compounds three structural modifications are known: $\alpha-$, $\beta-$ and $\gamma-Zn_4Sb_3$ which are stable below $263K$, between $263K$ and $765K$ and above $765K$, respectively. Due to it, the production of single phase Zn_4Sb_3 samples involves complicated processes[7, 8].

In this work we report on the study of transport and thermoelectric properties of $\beta - Zn_4Sb_3$ compounds prepared by hot pressing method.

2 Experimental

From high purity zinc and antimony powders (Merck 9.999%), the hot pressing method was used to prepare $\beta - Zn_4Sb_3$ samples. These components were thoroughly mixed in a ball mill during 40 hours, then the mixture was heated for 5 hours at $300°C$, $400°C$ and $450°C$, under a pressure of $50MPa$.
Electrical resistivity and Seebeck coefficient data were obtained by using the standard D.C. four-probe method and the differential technique, respectively. Additionally, the structural and morphological properties of the samples where studied by XRD and SEM analysis, respectively.

3 Results

Morphological properties of the studied samples can be seen in the Fig. 1, it is possible to observe samples highly dense, with compact grains without a defined shape and size.

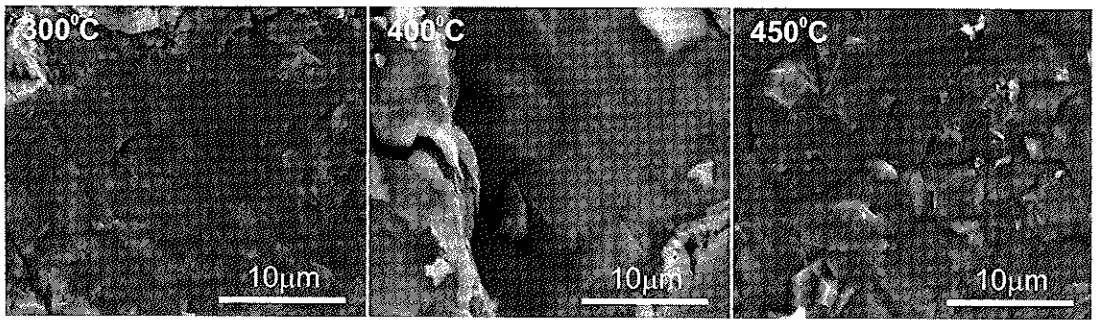

Figure 1: SEM micrographs of Zn_4Sb_3 polycrystalline samples grown by hot pressing method.

The x-ray diffraction analysis shows samples with $\beta - Zn_4Sb_3$ phase which has a rhombohedral (Hex.) crystal structure, of space group $R\bar{3}c$ and unit cell dimensions $a = b = 12.237(4)\AA$, $c = 12.446(5)\AA$ and $\gamma = 120.8^0$. Small quantities $ZnZb$ have been observed in the samples, which decreases with the processing temperature (see Fig. 2).

The behavior of electrical resistivity of Zn_4Sb_3 compounds corresponds to that of poor metals or heavily doped semiconductors [9]. The magnitude of $\rho(T)$ increases with the temperature and the annealing temperature (see Fig. 3a). $\rho(T)$ shows maximum values close to $9m\Omega - cm$ in the case of the sample annealed at 450^0C.

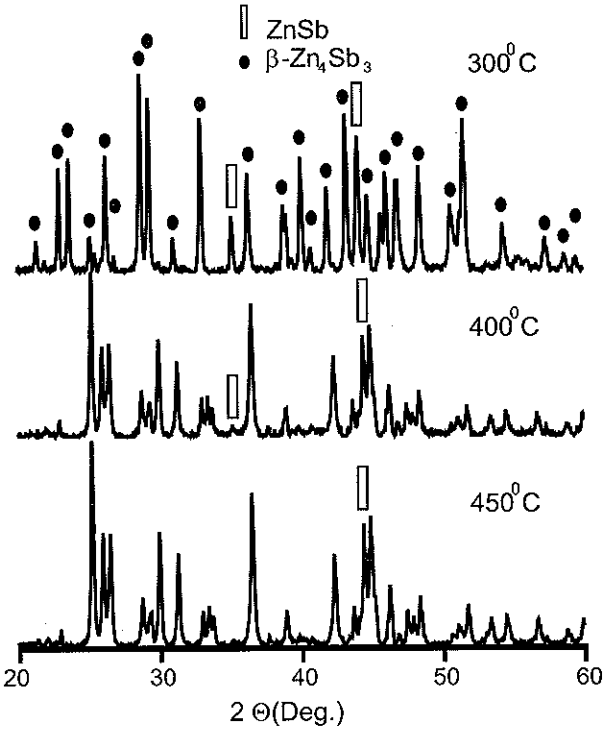

Figure 2: Room temperature powder x-ray diffraction patterns of Zn_4Sb_3 samples.

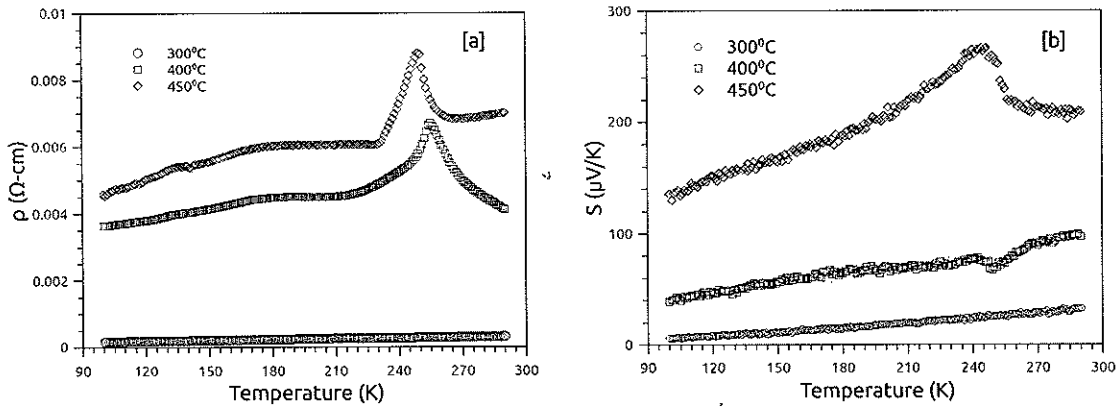

Figure 3: Temperature and annealing time dependence of electrical resistivity [a] and Seebeck coefficient[b] of polycrystalline Zn_4Sb_3 samples.

Figure 3b shows the temperature behavior of Seebeck coefficient. $S(T)$ is positive throughout the studied temperature range indicating a p-type conduction. The magnitude of $S(T)$ increases with the temperature reaching maximum values close to $270\mu V/K$.

Electrical resistivity and Seebeck coefficient show pronounced discontinuities between 235 and 255K, where the room temperature stable, disordered $\beta - Zn_4Sb_3$ goes to higher ordered $\alpha - Zn_4Sb_3$ phase. The β to α phase transition is given by the slight Zn deficiency of Zn_4Sb_3 with respect to its ideal crystallographic composition $Zn_{13}Sb_{10}$. It is important to note that the magnitude of this transition increases with the temperature of processing, that makes evident the increase of the quality of the samples [10, 11].

Good thermoelectric materials are those that exhibit high values of electrical conductivity and Seebeck coefficient and low thermal conductivity. The electrical properties of a thermoelectric material are evaluated through the thermoelectric Power Factor, PF. It is a function of the mobility and the effective mass of the electrical carriers. PF is expressed as [1] $PF = S^2/\rho$, where S is the Seebeck coefficient and ρ the electrical resistivity. From Seebeck coefficient and electrical resistivity experimental data the thermoelectric power factor was calculated. PF increases with the temperature, reaching maximum values close to $10\mu W/K^2 - cm$, for the sample annealed during five hours at 450^0C. The values of PF exhibited by these samples suggest that Zn_4Sb_3 compounds can be prepared by using the hot pressing method. This method avoids both the oxidation and the segregation of Zn and Sb, which are serious problems in the preparation of this kind of compounds.

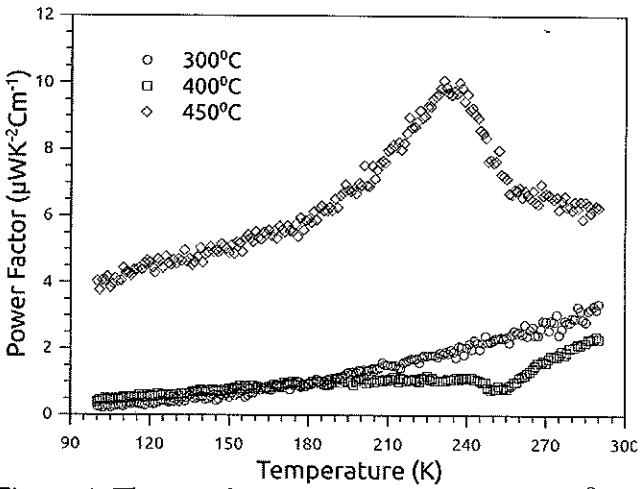

Figure 4. Thermoelectric power factor ($PF = S^2/\rho$) as a function of temperature of Zn_4Sb_3 samples.

4 Conclusions

By using the hot pressing method was possible to prepare single phase $\beta - Zn_4Sb_3$ samples. It, in all the studied samples, exhibit high Seebeck coefficient values and an electrical resistivity with maximum values less than $9m\Omega - cm$. From Seebeck coefficient and electrical resistivity was possible to calculate the thermoelectric Power Factor it in the case of the samples prepared at 450^0C, during 5 hours, reaches maximum values close to $10\mu W/K^2 - cm$.

An order-disorder transition was observed in the transport properties close to $240K$, which is associated with a reduction of symmetry between β- and α-Zn_4Sb_3 phases. This transition is a typical feature observed in pure single crystals $\beta - Zn_4Sb_3$ samples.

Acknowledgements

The authors would like to thank to *"La División de investigación de la Universidad Nacional de Colombia,* DIB" for the financial support.

References

[1] Rowe D. M. *CRC Handbook of thermoelectrics* (ed.D.M. Rowe), Boca Raton, CRC Press, 1995.

[2] Mahan G., Sales B. and Sharp J., *Physics Today* **50**, 42 (1997).

[3] Nolas G.S., Sharp J., Goldsmid H. J.,*Thermoelectrics, Basic principles and new materials developments*, Springer-Verlag, Berlin, 2001.

[4] Venkatasubramanian R., Siivola E., Colpitts T., O'Quinn B., *Nature*, **413**, 597 (2001).

[5] Chen G., Dresselhaus M.S., Dresselhaus G., Fleuriar J.P. and Caillat T., *Inter. Mater. Rev.*, **48**, 45-66(2003).

[6] Izard V., Record M.C., Tedenac J.C. and Fries S.G., *Calphad*, **25**, 567-581 (2001).

[7] Caillat T., Fleurial T. J., Borshchevsky A., *J. Phys. Chem. Solids*, **58**, 1119-1125 (1997).

[8] Ur S., Nash P. and Kim I., *J. Alloys Compd.*, **361**, 84-91 (2003).

[9] Wu Y., Nylen J., Naseyowma C., Garcia-Garcia F. and Haussermann U., *Chem. Mater.* **21** 151-155(2009).

[10] Bhattacharya S., Hermann R.P., Keppens V., Tritt T. M. and Snyder G. J., *Phys. Rev.B* **74**,134108 (2006).

[11] Souma T., Nakamoto G. and M. Kurisu, *J.Alloys Compd.*, **340**, 275-280 (2002).

GRÄTZEL TYPE-SOLAR CELLS SENSITIZED WITH SOME COLOMBIAN'S DYES.

CELDAS SOLARES TIPO GRÄTZEL SENSIBILIZADAS CON COLORANTES COLOMBIANOS

Eduardo Perez*, Kiara Montalvo*, María Acuña*, Tomás Rada* , Florian Buchholz**

ABSTRACT

Perez, E., K. Montalvo, M. Acuña, T. Rada, F Buchholz. Grätzel type-solar cells sensitized with some Colombian's dyes. Rev. Acad. Colomb. Cienc., 37 (1): 36-39, 2013. ISSN 0370-3908.

In the present work we want to show some progress related to the effects of two colombian´s natural dyes in the sensitized solar cells (Grätzel type). The dyes used are achiote and blackberry, which are used to develop a photochemical process that mimics photosynthesis. The use of sensitizers in conjunction with nanocrystalline oxide semiconductor films (TiO_2) permits to increase the absorption of sunlight. Raman spectroscopy technique has been used to characterize the achiote. They show that the samples have a strong fluorescence in the range between 640 and 800 nm, and this fluorescence is very sensitive to the laser power. After the construction of the solar cells, the efficiencies determined are around 0.13%, in the best of our cases.

Key words: Dye-sensitized solar cells; Nanocrystalline oxide semiconductor films; titanium dioxide TiO_2. Bixa Arellana

RESUMEN

En el presente trabajo se muestran algunos logros relacionados con los efectos de dos colorantes naturales colombiano en las celdas solares tipo Grätzel. Los colorantes usados son achiote y mora de castilla, los cuales son usados para desarrollar un proceso fotoquímico que asemeja la fotosíntesis. El uso de estos sensibilizadores en unión con películas nanocristalinas de un óxido semiconductor (TiO_2) permite incrementar la absorción de luz solar. La técnica de espectroscopía Raman se ha usado para caracterizar el achiote. En los espectros se observa que las muestras tienen una fuerte fluorescencia en el rango entre 640 y 800 nm, la cual es muy sensible a la potencia del laser. Después de construidas las celdas solares, la eficiencia obtenida está alrededor de 0,13% en el mejor de nuestros casos hasta ahora.

Palabras claves: Celdas solares Sensibilizadas por colorantes; Películas de óxido semiconductor nanocristalinas; TiO_2. Achiote

* Grupo de Investigación en Física Aplicada, Universidad del Norte, Barranquilla, Colombia. Email: trada@uninorte.edu.co

* Technische Universität Berlin, Berlin, Germany

1. Introduction

Chemists and physicists have been interested for long time in the harnessing of sunlight to convert the light directly into electrical energy. A seminal work driven by **B. O´Reagan** and **M. Graetzel,** 1991 [1] showed that the application of dye molecules harvest the sunlight, with an additional interesting feature which is the low-cost. The study of this type of solar cells in Colombia has an important role because of two main aspects; one is Colombia's location near the equator with a high solar radiation throughout the entire year and second for the diversity of fruits and plants that we have here.

Typically, Dye Sensitized Solar Cell (DSSC) devices consist of two substrates of glass that are coated with a thin conductive layer (in this investigation it was used glass with fluorine-doped tin oxide (FTO)) that serve as basis for the electrodes. On the anode a layer of the mesoporous semiconductor is applied (nanoparticles of titania-oxide, TiO_2) and on the cathode (or counter electrode) a layer of a catalytic conductor (in this case carbon). In between the electrodes the sensitizing dye and a solution with a redox couple (in this case iodide/triiodide) is positioned. Two dyes were used: Achiote (*Bixa orellana*) and Blackberry (*Rubus glaucus or mora de castilla*) with several concentrations in ethanol and water.

For maximal power output a solar cell is operated at the so called maximum power point (P_{MPP}). The efficiency η of the solar cell is defined by the following equation (1):

$$\eta=P_{MPP}/P_{in}=(U_{MPP}*I_{MPP})/P_{in} \quad (1)$$

Where P_{in} is the solar power input into the solar cell (SC) and U_{MPP} and I_{MPP} are voltage and current at maximum power point. For detecting the MPP (maximum power point) it is necessary to measure a so called IV-curve that is the graph of current as a function of voltage and calculate the product of both values. In order to have a main idea of the quality of the cells and also for deeper knowledge about other parameters of a cell, the open-circuit voltage and short-circuit current are important parameters. They are connected with P_{MMP} through the following equation (2):.

$$P_{MPP}=U_{MPP}*I_{MPP}=U_{OC}*I_{SC}*FF \quad (2)$$

Where FF is the so called fill factor, which is defined as the ratio of $U_{MPP}*I_{MPP}$ / $U_{OC}*I_{SC}$.

2. Samples preparation

Two native dyes were used: Achiote and Blackberry. The dye of Achiote needs to be extracted from the shell of the seeds, thus it is not possible to just crush them. We did it in two different ways without noticeable differences in the results. First we took 10 g of fresh seeds in 10 ml of ethanol and stirred for about 20 min until an homogenous color was observed. Then it was heated up until powder was extracted and ethanol evaporated. Next we mixed 1g of Achiote powder with 10 ml of ethanol. The second way was to mix 10 g of Achiote with 10 ml (1:1 proportion or 50% for us) or 10 g of Achiote with 20 ml of ethanol (1:2 proportion or 25% for us), then we stirred for 20 min and finally we filtered the mixture to get rid of many solid particles. The fresh blackberries were smashed without water (100%) and 20 g mixed with 20 ml of water (1:1 proportion or 50%). We explore other proportions but good results came only from the previously mentioned.

As support for electrical contact in the SC, glass with a tin film of FTO was used both at the photoanode and the counter electrode. The glasses pieces are of approximately 2 x 2 cm^2, the counter electrodes had to be drilled two times for the injection of electrolyte. All pieces were cleaned through the following procedure: Primary each piece was wiped carefully with a soft sponge using tapped water, then rinsed with deionzed water and stored in a bath of deionzed water until the fat-free glasses were put in an ultrasonic bath of ethanol for some minutes to get rid of the last contaminating particles.

For the photoanode, a ready to use paste of semiconducting nanocrystalline TiO_2 from Solaronix (Ti-Nanoxide D) was used in conjunction with Dr Blade technique for layers depositions. Working areas were of 1x1 cm^2 or 0.5 x 0.5 cm^2 for smaller active areas. It is important to mention that the deposition of titania on the transparent conducting oxide (TCO) glasses is the most important part of the production process because the homogeneity of the layer is crucial for cell efficiencies. Primary masks of 1x1 cm^2 (or 0.5x0.5 cm^2 for smaller active areas) were cut into a stripe of adhesive tape (Scotch 3M Magic # 810) with a stencil. The area of the mask remained uncovered on the conductive layer and the paste was spread across the plate. For multilayers of Titania two or more layers of tape were applied (one layer of tape for up to two layers of Titania). Sintering of every layer occur in a programmable oven up to 450°C and leaving there for 20 to 30 min.

The sensitization of titanium dioxide by natural dyes consists of soaking the titania electrode in mashed fruits or Achiote solution. Complete staining can take from several minutes, for Achiote solution, to several hours for blackberries mixture, while the dye molecules naturally adsorb onto the titania particles. The longer the electrode soaks in the dye, the better

dyed the titania will be. To remove the stained electrode we rinse it carefully with water (for Blackberries) or ethanol (for Achiote) and wait a few minutes for the ethanol to evaporate until the resulting stained titania looked homogeneously dyed almost all over its surface. If not, put it back in to the solution for further dyeing.

Properties of solar cell can be determined when it is under homemade 10.9 mW/cm^2 (for most of the cases) halogen illumination and tested using the standard silicon solar cell, as published by **Ali,** 2010 [2].

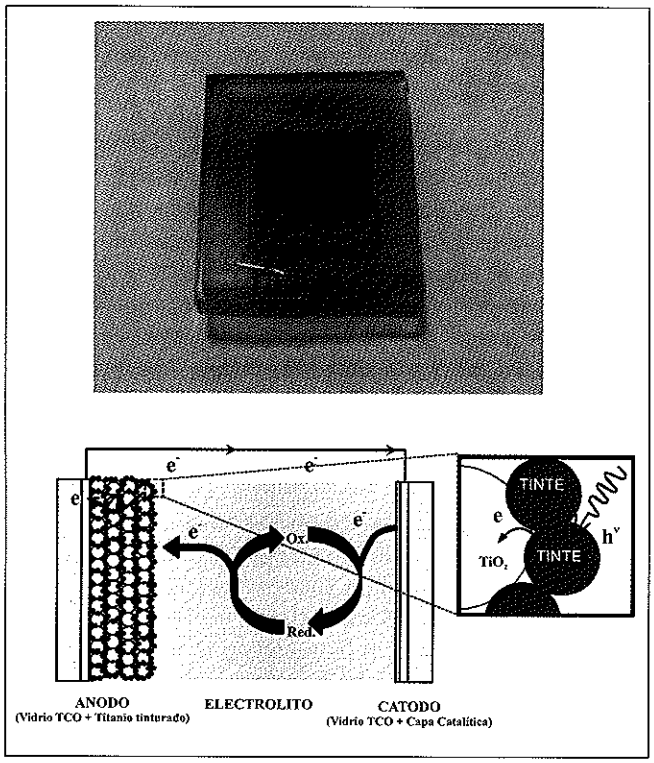

Figure 1. A picture of a full assembled SC in the left. In the right a schematic SC under illumination is showed.

3. Results and discussions

There is little information regarding the physical and chemical properties of Achiote, therefore some Raman measurements were made in order to identify the basic molecule. According to the results the Achiote contains mainly carotene molecule as shown in Fig 2. In addition, the Achiote showed a strong fluorescence in the range from 640 to 800 nm, however this fluorescence is very sensitive to the laser power.

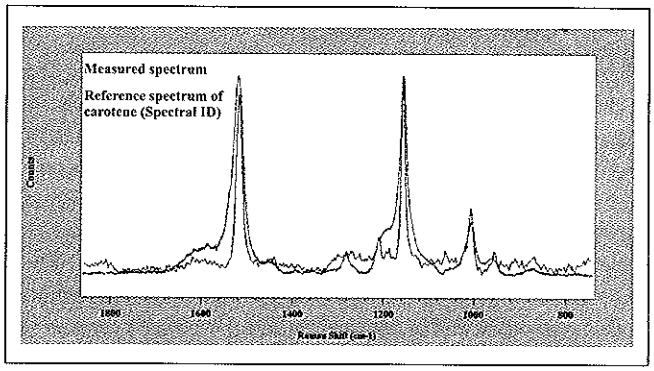

Figure 2. A Raman spectrum of Achiote match with a reference spectrum of carotene. Courtesy of Aphèlie Lancry from HORIBA Jobin Yvon SAS and S&S Ingeniería Colombia.

3.1 Current-voltage measurements

Several variables were explored in our approach to study their effects in the solar cells construction ranging from dye concentration, TiO_2 layer thickness and sizes of active areas. In the table No. 1 we show the effect of layers number on the I-V measurements of the SC using blackberry as sensitizing dye. We considered that good results for the current were obtained using either 4 or 6 layers with size of 1.0 x 1.0 cm^2. However the voltage seems similar regardless the thicknesses of titania layers: all measurements are above 400 mV.

Table 1: Parameters of SC with Blackberry.

Cell N°	Layers	A (cm^2)	UOC (mV)	ISC (μA)
89	2	1,0X1,0	450	47
73	3	0,5X0,5	419	39
84	4	1,0X1,0	440	74
82	5	1,0X1,0	440	14
79	6	1,0X1,0	427	64

For Achiote as sensitizing dye, in table No. 2, we observe that the best results for voltage and current occurs with 6 TiO_2 layers with active area of 1.0x1.0 cm^2. The voltage values are also around 400 mV for any number of layers in our range and the current is increased with layers.

Table 2: Parameters of SC with Achiote

Cell N°	Layers	A (cm^2)	UOC (mV)	ISC (μA)
50	2	1,0x1,0	391	24
88	4	1,0x1,0	454	39
71	6	1,0x1,0	427.1	103.6

3.2 Efficiency

The IV-characteristics curve and the performance values of some of the best cells are demonstrated in Fig. 3 and Tab. 3. The best efficiency of 0.130 % was obtained using Achiote and 6 layers of Titania, despite the very low fill factor of 32%. A calculation of the best cell with smaller area (No.74), with a fill factor of 49,8 % showed a very similar efficiency of 0.118%. These are close to the 0.22% reported by **Ali, R.A.M.& Nayan, N,** 2010.[2] for Dragon Fruit and 0.42% and 0.56% reported by **G. Galogero et al.,** 2012 [3] for Raw Blackberry and Giacchè Grape, respectively.

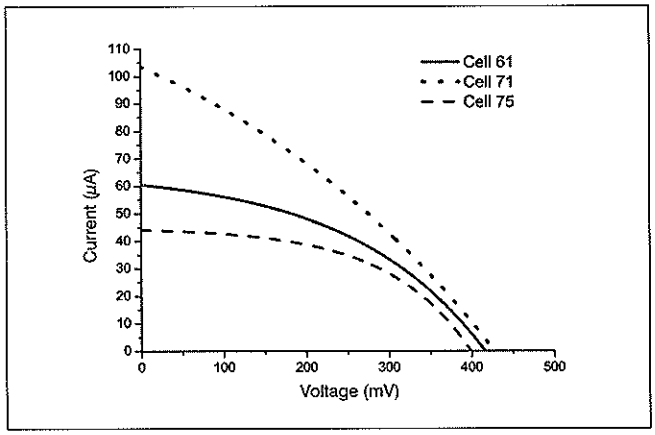

Figure 3. I-V Curves of three different SC under illumination for P_{MPP} calculations.

Table 3: Parameters of SC including the efficiency

No.	61	71	75	74
Dye	BB 50%	Achiote	BB 50 %	BB 50 %
layers	4	6	4	4
A (cm^2)	1,0x1,0	1,0x1,0	0,5x0,5	0,5x0,5
J (mW/cm^2)	21,6	10,9	10,9	10,9
Uoc (mV)	416,0	427,1	398,8	405
Isc (mA)	60,5	103,6	44,2	64
FF	41,8 %	32,0 %	49,8 %	49,8 %
Efficiency	0,052 %	0,130 %	0,080 %	0,118 %

4. Conclusions

Two Colombian's native fruits, Achiote and Blackberry (also known as Mora de Castilla), are used in the fabrication of DSSC as sensitizers. Both dyes have showed a relatively good efficiency (0.130% and 0.118%) and performance under controlled illumination. Exploring some variables, we have found that the greatest enhancement was achieved by increasing the number of titania layers, through the Dr Blade preparation. In our case 4 layers of TiO_2 for Blackberry and 6 layers of TiO_2 for Achiote are the best semiconductor thickness.

Another important aspect is related to the voltage and current values. In general, voltage values are relatively stables and are around 400 mV, while the current is directly affected by active area and the quality of TiO_2 deposition. We found for Achiote that the 1.0 x1.0 cm^2 is good size, however for Blackberry a smaller area works better. We can reasonably conclude that reducing the size of the active area improved the efficiency significantly, especially the fill factor.

References

[1] **O'Regan B, and Graetzel M,** 1991, A low–cost, high–efficiency solar cell based on dye- sensitized colloidal TiO2 films, Nature 353, 737

[2] **Ali Ram. and Nayan N,** 2010, Fabrication and analysis of dye-sensitized solar cell using natural dye extracted from dragon fruit, International Journal of Integrated Engineering, 2 55

[3] **Calogero G,** et al. 2012, Anthocyanins and betalains as light-harvesting pigments for dye-sensitized solar cells, Solar Energy 86, 1563

THE INFLUENCE OF PRESSURE ON THE STRUCTURAL AND ELECTRONIC PROPERTIES OF Bi

INFLUENCIA DE LA PRESIÓN SOBRE LAS PROPIEDADES ESTRUCTURALES Y ELECTRÓNICAS DE Bi

G. Patricia Abdel Rahim[*,], Jairo Arbey Rodríguez Martínez[**], María Guadalupe Moreno-Armenta[***]**

ABSTRACT

Abdel Rahim G. P, J. A. Rodríguez Martínez, M. G. Moreno-Armenta: The influence of pressure on the structural and electronic properties of Bi. Rev. Acad. Colomb. Cienc., 37 (1): 40-43, 2013. ISSN 0370-3908.

Calculation of the structural and electronic properties of Bi was carried out in the framework of density functional theory (DFT). The graphs of energy vs. volume for some possible structures show that the most stable one is the rhombohedral; the others are metastable. We also found two phase transitions induced by pressure. The most important result of this research is the prediction about the existence of FCC structure of Bi at higher pressures than ~3GPa. The electronic properties for the rhombohedral structure show that our calculations are in overall good agreement with other calculations. This agreement serves to validate the pseudo Bi.pbe-dn-kjpaw.UPF. Therefore, the above-mentioned is suitable for use in future calculations.

Key words: Bismuth, structural and electronic properties, wien2k, quantum-espresso, rhombohedral structure

RESUMEN

Se realizaron cálculos acerca de las propiedades estructurales y electrónicas del Bi en el marco de la teoría DFT. De los gráficos de energía contra volumen se halló que la estructura más estable es la romboedral; las demás son meta estables. También encontramos dos transiciones de fase provocadas por presión. Nuestro principal hallazgo es la existencia del Bi en la fase FCC para presiones superiores a 3GPa aproximadamente. Nuestros resultados de las propiedades calculadas están en muy buen acuerdo con otros cálculos y con mediciones experimentales. Esta concordancia nos sirve para validar el pseudopotencial Bi.pbe-dn-kjpaw.UPF para otros cálculos futuros.

Palabras clave: Bismuto, propiedades estructurales y electrónicas, wien2K, quantum-espresso, estructura romboedral.

* Universidad Distrital Francisco José de Caldas, Bogotá, Colombia. E-mail: pabdelrahim@gmail.com

** GEMA, Departamento de Física, Universidad Nacional de Colombia, Sede Bogotá, Colombia. E-mail: jarodriguez@unal.edu.co

*** Centro de Nanociencias y Nanotecnología – CNy N, UNAM, Ensenada, BC, México. E-mail: Moreno@cnyn.una.mx

Introduction

Bi is interesting because its surfaces, such as Bi(111), Bi(110), and Bi(100), are an open door for use in nanotechnology. Because Bi's surfaces are quasi-two-dimensional metals with peculiar spin properties, Bi could be used in both spintronics and quantum computing as a spin source or a spin filter [1]. Due to the fact that its importance in nanotechnology is rising [2], here we present the first step of a wider investigation that comprises volume, surfaces, absorption of atoms, and interfaces with other materials such as graphene or MgO. Bi has been studied in thin films, nanowires and clusters [3]. In the present paper, we carried out calculations of energy as a function of volume for several structures such as diamond (#227), NiAs-like (#194), FCC-like (#225), Cubic Simple-like (CS, #221), and rhombohedral (R-structure, #166). From these graphs, we deduce that the most stable one is the R-structure and that the others are metastable, and finally there are two phase transitions induced by pressure. After that, we present the electronic properties.

Bi is semi-metallic and has an R-structure with a=4.746 Å, α=57.23° (300K) [1]. Because $\alpha \approx 60°$, and this value defines the cubic structure, other cubic and hexagonal phases such as the NiAs-like were included, because they are close to it. Taking into account that at room-temperature Bi exhibits a phase transition toward monoclinic at about 2.55 GPa and after that it changes, at about 2.7GPa, to tetragonal and finally reaches a body-centered cubic structure, at ~ 7.7 GPa, we searched for other phase transitions and in fact found some of them. The study of this had not been done before our research. All calculations were carried out in the framework of DFT, with spin polarization using W2k [5] and QE [6]. This task was also done in order to validate the pseudo Bi.pbe-dn-kjpaw.UPF, which we obtained from Theos-Theory and Simulation of Materials's pseudo library [7]. The results show that this pseudo is suitable for use in QE-calculations, because the results are in a good agreement with those obtained with the all-electron full-potential (linearized) augmented plane-wave ((L)APW) + local orbitals (lo) method, which is implemented in the W2k code and other calculations. Table 1 shows some parameters found in the scientific literature which served us for the sake of comparison.

Table 1. Cell parameters for Bi in hexagonal structure space-group #166, *the method used in [1] is tight-binding and in [4], [8] and [10] is interaction of X-Ray with matter.

Bismuth	a (Å)	c(Å)	c/a
Ph. Hofmann [1]	4.5332	11.7967	
C. Laulhé, et al. [4]	4.546	11.862	
P. Cucka and C. S. Barrett 8]	4.546 (298°K) 4.535 (78°K)	11.862 (298°K) 11.814 (78°K)	
T.N. Kolobyanina, et al. 10]	4.5452 (298°K)	11.860 (298°K)	2.609 (298°K)

Calculation details: Parameters used in wien2k and quantum-espresso

In calculations with W2k, we used the GGA approx. in the parametrization of Perdew, Burke y Ernzerhof (PBE) [11]. Muffin-tin radius was R_{MT}= 2.65 a.u., and R_{MT} X K_{max}= 8.0, where K_{max} limits the maximum kinetic energy for plane wave base. For the base of spherical harmonics Y_{lm},, we used l_{max} = 10. The convergence criterion for the energy was 0.0001 Ry. In QE-calculations, we also used GGA-PBE approx. with 45 Ry as the energy cutoff, and the charge density cutoff was 450 Ry. The convergence was 0.0001 Ry.

Results

Fig. 1 shows the dependence of cohesion energy as a function of volume for several structures. These results are very similar for calculations carried out with W2k and QE. All phases are metastable because they all have a minimum, and the most stable one is the R-structure. The values of a and c are in a good agreement with those in [1] (~ 1% for a and ~ 2% for c). Fig. 2 shows the enthalpy calculated from the data of energy vs. volume. One can observe that there are interceptions at ~ 3 GPa, because there are two phase transitions induced by pressure. One is from FCC to CS, and the other is from NiAs to the CS phase. We predict a new structure for Bi: FCC; from that phase it would be possible to reach the CS phase.

In the transitions the volume reduces by about 12%, from 67 Å^3 to 60 Å^3. The minimum of the energy of the FCC and the NiAs-like differ by only 0.11 eV and 0.18 eV by unit formula, respectively. The structural parameters obtained by means of W2k are shown in Table 2. Calculations performed with QE resulted in a=4.5651 Å, c/a=2.5327, and volume V=52.170 Å^3. These parameters differ by only 0.7% and 2.7% from those in [1] in a and the quotient c/a, respectively. With the R-structure, we obtained a=4.7043 Å and V=70.058 Å^3. The Bi atoms were freed during the relaxation process in QE, and the final coordinates were (0.54, 0.54, 0.54) and (0.0067, 0.0067, 0.0067). Other parameters were α= 57.890° and d_1/d_2 = 0.86. Comparison with [1] shows that α and d1/d2 differs by only 0.95% and 2.23%, respectively.

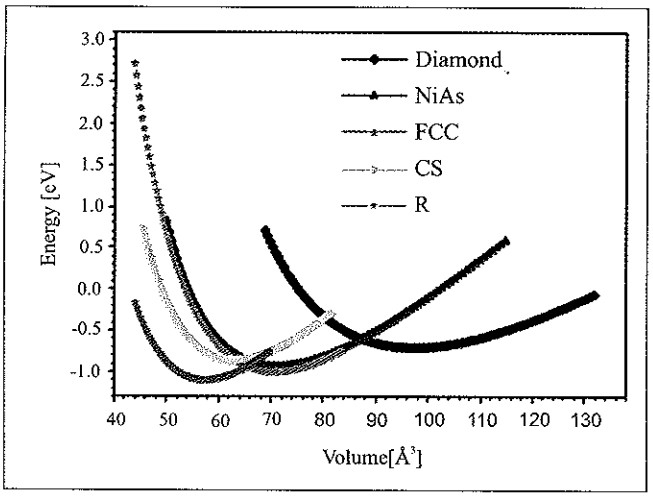

Figure 1 Energy vs. volume for several phases

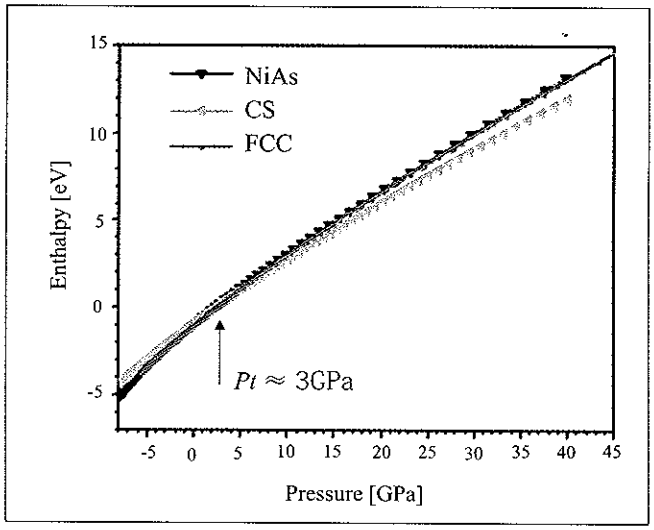

Figure 2. Enthalpy vs. pressure shows the transition phases

Table 2. Structural properties of Bi calculated with W2k.

Structural Parameter	Diamond Our results	NiAs Our results	FCC Our results	CS Our results	R-structure Our results
amin [Å]	7.300	4.515	6.565	3.983	4.6719
Volume [Å3]	97.256	71.138	70.745	63.218	58.072
c/a	--------	1.78	--------	--------	2.6303
B [GPa]	28.24	42.19	47.04	53.14	52.50
B'	4.33	4.887	4.059	4.30	4.5198
E cohesión [eV]	-0.707	-0.9315	-1.0018	-0.859	-1055

Electronic Properties

Fig. 3 shows the electron bands in the R-structure at the minimum of the energy, i.e. at zero pressure, and they are in a good agreement with those obtained in [1] and [3]. We note that the valence and conduction bands touch each other at the L and T high-symmetry points of the first Brillouin zone, and this fact is a sign of the semi-metallic behavior of Bi. Fig. 4 shows the bands calculated by means of QE-code, and one can observe that they are in a good agreement with those of Fig 3.

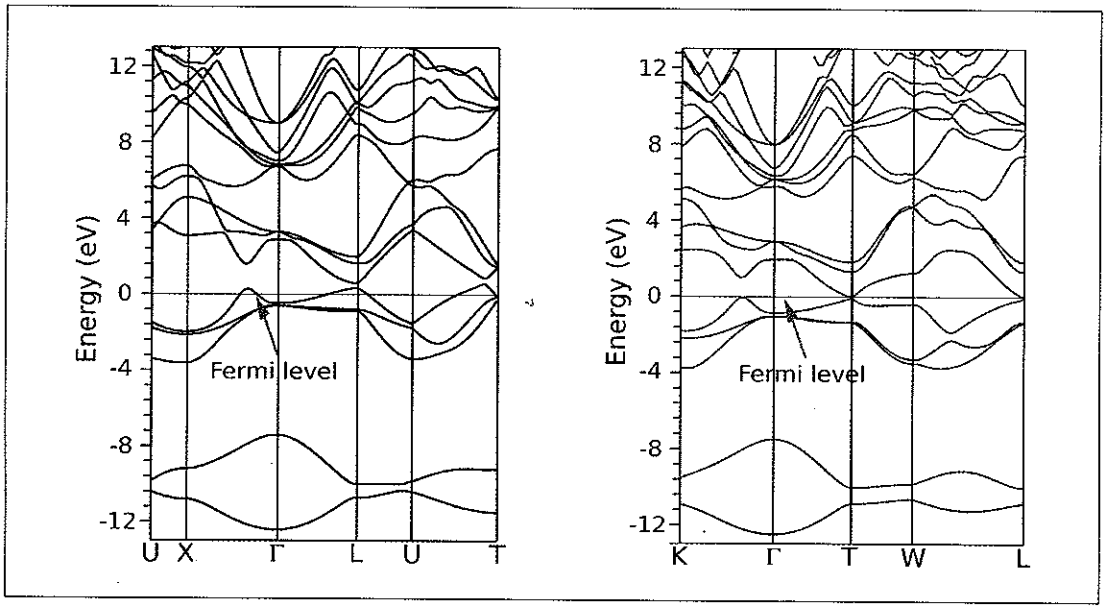

Figure. 3. Bands of Bi in the R-structure calculated using W2k

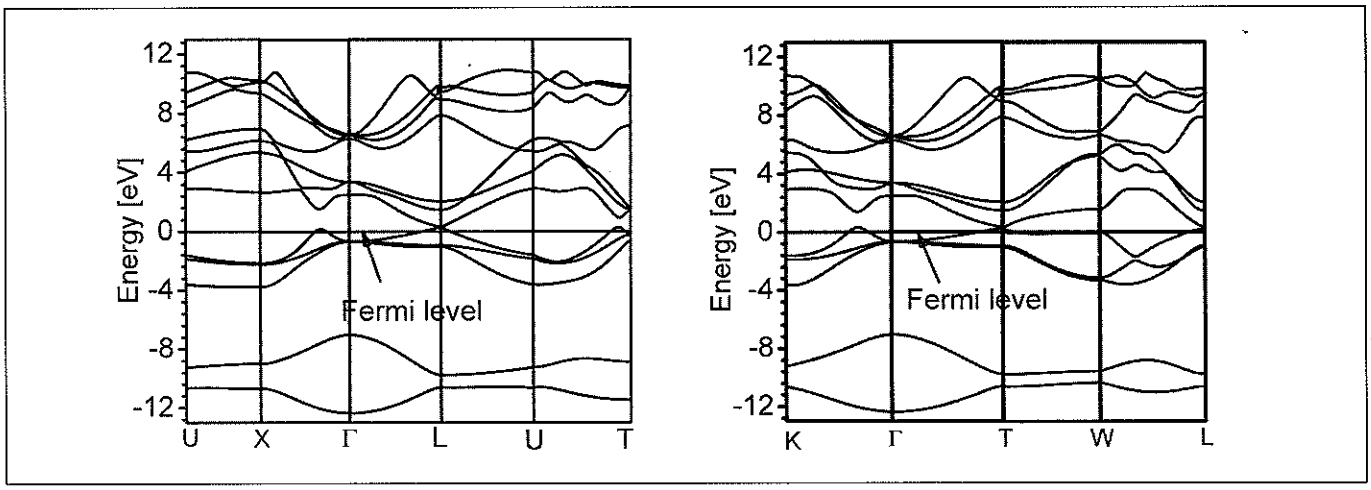

Figure. 4. Bands of Bi in R-structure calculated using QE-code

Summary and conclusions

Calculations of the structural and electronic properties of Bi were carried out in the framework of DFT using two codes: W2k and QE. From the graphs of the energy as a function of volume, in several possible structures, one finds that the most stable is the R-structure. The other structures considered are metastable, and one also finds two phase transitions induced by pressure. The first is from FCC to CS, and the other is from NiAs to the CS. Our main conclusion is about the prediction of the phase FCC of Bi at higher pressures than ~3GPa. The electronic properties for the R-structure show that our calculations are in overall good agreement with other calculations. This agreement serves to validate the pseudo of Bi that we obtained from the QE pseudo library. Therefore, the pseudo mentioned is suitable for use in future calculations.

Acknowledgments

Calculations were carried out in the DGCTIC UNAM Supercomputing Center in México and in the cluster of the GEMA Group at the Physics Dept. of Universidad Nacional de Colombia (UN), Bogotá. GPAG was partially supported by the Doctoral Curricular Program of the Faculty of Engineering at UN.

References

[1] **Ph. Hofmann**, 2006. The surfaces of bismuth: Structural and electronic properties, Progress in Surface Science, 81, DIO:10.1016/j.progsurf.2006.03.001

[2] **Bernadette Landschreiber et al.**, 2013, Structural and thermoelectric properties of $Bi_{1-x}Sb_x$ nanoalloys prepared by mechanical alloying, Journal of Electronic Materials, DOI: 10.1007/s11664-012-2455-1.

[3] **Y. Liu, R.E, Allen**, 1995. Electronic structure of the semimetals Bi and Sb, Physical Review B **52** 1566.

[4] **C. Laulhé, M. Cammarata, M. Servol, R.J. Dwayne Miller, M. Hada, and S. Ravy**, 2013, Impact of laser on bismuth thin-films, Eur. Phys. J. Special Topics **222**, 1277--1285, DOI: 10.1140/epjst/e2013-01922-0.

[5] **P. Blaha, K. Schwarz, and J. Luitz**, WIEN97, A Full Potential Linearized Augmented Plane Wave Package for Calculating Crystal Properties (Karlheinz Schwarz, Techn. Universität Wien, Austria), 1999. ISBN 3-9501031-0-4.

[6] **P. Giannozzi, et al**, 2009, Quantum espresso: a modular and open-source software for quantum simulations of materials, J.Phys.: Condens. Matter, **21**, 395502, http://dx.doi.org/10.1088/0953-8984/21/39/395502

[7] We used the pseudopotential Bi.pbe-dn-kjpaw.UPF from http://theossrv1.epfl.ch/Main/Links

[8] **P. Cucka and C. S, Barrett**, 1962, The crystal structure of Bi and of solid solutions of Pb, Sn, Sb and Te in Bi, Acta Cryst. 15, 865-872 doi: 10.1107/S0365110X62002297

[9] **J.P. Dismukes, R. J. Paff R. T. Smith, and R. Ulmer**, 1968, Lattice Parameter density in bismuth-antimony alloys, J. Chem. Eng. Data 13, 317--320.

[10] **T. N. Kolobyanina, S. S. Kabalkina, L. F. Vereshchagin, A. Y. Michkov, and M. F. Kachan**, 1971, Soviet Physics Jetp, 32(4), 624-629, http://www.jetp.ac.ru/cgi-bin/dn/e_032_04_0624.pdf

[11] **J.P. Perdew, K. Burke, M. Ernzerhof**, 1996 ,Generalized Gradient Approximation Made Simple, Phys. Rev. Lett. 77, 3865.

MAGNETIC TRANSITION OF YTTERBIUM ATOMS CONFINED IN OPTICAL SUPERLATTICE WITH LOCAL FERROMAGNETIC INTERACTION

TRANSICIONES DE FASE MAGNÉTICA DE LOS ÁTOMOS DE ITERBIO CONFINADOS EN UNA SUPERRED ÓPTICA CON UNA INTERACCIÓN LOCAL FERROMAGNÉTICA

Diego-F Ramírez*, R. Franco., J Silva-Valencia*****

ABSTRACT

Ramírez Diego-F, R. Franco, J. Silva-Valencia. Magnetic transition of ytterbium atoms confined in optical superlattice with local ferromagnetic interaction. Rev. Acad. Colomb. Cienc., 37 (1): 44-49, 2013. ISSN 0370-3908.

We used the density matrix renormalization group to study the ground state of ytterbium atoms (^{171}Yb) for the Hund lattice model, where the delocalized atoms are confined in a one-dimensional optical superlattice and his number is one third of the lattice sites. We found a paramagnetic-ferromagnetic quantum phase transition for any value of the potential strength. The local critical ferromagnetic coupling decreases as the superlattice potential increases.

Key words: Hund lattice model, ferromagnetic coupling, heavy fermions

RESUMEN

Nosotros usamos el grupo de renormalización de la matriz densidad para estudiar el estado base de los átomos de Iterbio (^{171}Yb) para el modelo de red de Hund, donde los átomos delocalizados son confinados en una superred óptica unidimensional y son un tercio de los sitios de la red. Nosotros hallamos una transición de fase magnética paramagnética-ferromagnética para algunos valores del potencial. El punto crítico del acoplamiento decrece cuando el potencial de la superred disminuye.

Palabras clave: Modelo de red de Hund, acoplamiento ferromagnético, fermiones pesados.

* Departamento de Física, Universidad Nacional de Colombia, A.A. 5997, Bogotá, Colombia, E-mail: difframirezro@unal.edu.co

** Departamento de Física, Universidad Nacional de Colombia, A.A. 5997, Bogotá, Colombia, E-mail: refrancop@unal.edu.co

*** Departamento de Física, Universidad Nacional de Colombia, A.A. 5997, Bogotá, Colombia, E-mail: jsilvav@unal.edu.co

1. Introduction

Ultracold atoms confined in an optical lattice (quantum simulation) offer a clean and simple system for the experimental investigation of quantum phase transitions. Bosonic [1] and fermionic [2, 3] models, and the spin Hamiltonians [4] can be controlled under novel conditions: dimensionality, interactions between particles through Feshbach resonances [5], independent periodic potential [6, 7] and different lattice topologies [8]. Moreover, Gorshkov et al. [9] showed that properties of fermionic alkaline-earth-metal atoms confined in an optical lattice allows the simulation of simple models, or condensed-matter Hamiltonians, such as the Kugel-Khomskii model [10], $SU(N)$ Hubbard chains [11] and the Kondo lattice model [12, 13]. Motivated by these developments, we analyze ytterbium atoms confined in an optical superlattice using the Hund lattice model (HLM).

The Kondo lattice model (KLM) and its Hund lattice model (HLM) counterpart are canonical models for studying the interaction between a magnetic moment (localized) interacting via a contact Heisenberg exchange J with the spin of any conduction (delocalized) electron at each lattice site. For these models, the one-dimensional and three-dimensional ground-state phase diagram is determined by two para/meters: the ratio of the exchange coupling to the hopping (J/t), and the density of the conduction electrons n_c; with strong coupling the Kondo effect favors the singlet state, while with weak coupling the RKKY interaction tends to stabilize a magnetic order. Fig. 1 shows the phase diagram for the Hund model with numerical results, with a localized magnetic moment $S=1/2$, analogous to the KLM [14]. At half-filled $n=1$, characterized by a spin gap, the system exhibits a spin-liquid phase [15]. The ferromagnetic phase exists above the critical points (empty symbols). The phase beneath the critical points is much less understood; Ref. [14] shows two phases: the "spiral" phase characterized by two broad peaks in the local spin-spin correlation function, and the "island" phase, characterized by the ferrimagnetic condition. However, for intermediate coupling, there is another ferromagnetic state between the "paramagnetic" phase [16]. Moreover, Ref. [17] analyzes the paramagnetic phase in the KLM with alkaline-earth-metal atoms confined in an optical lattice. Based on the latest literature, which motivates the present paper, we assumed the "paramagnetic" term for this area.

For three-dimensional electronic structures, the KLM is applied to heavy-fermions material (with greatly enhanced effective mass), which exhibits an antiferromagnetic (AFM) exchange, favoring the antialignment between localized and delocalized particles. The HLM is applied to manganese oxide perovskites, with a ferromagnetic (FM) exchange moderated by Hund's rule coupling; a strong coupling favors the alignment of the three localized t_{2g} spins with the spin of the e_g conduction electron [23]. However, the experimental data of manganese oxide perovskites disagree with the model [27].

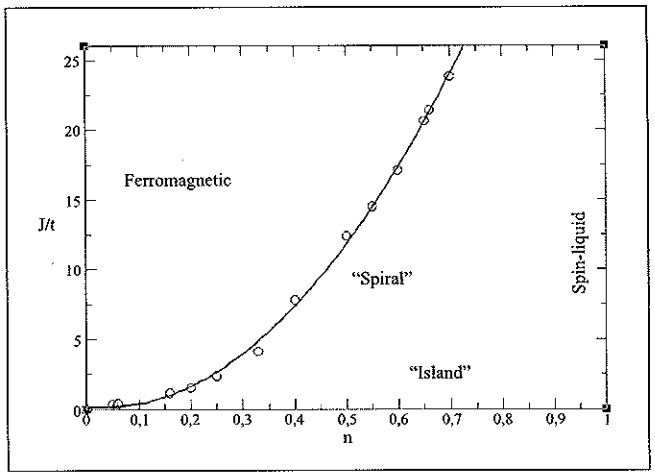

Figure 1. Magnetic phase diagrams of 1D Hund model. The ferromagnetic coupling increases with the filling. (Points taken from Ref. [14]).

Experimental investigation at low dimensionality in heavy fermion systems, reproduces the conditions of the KLM (Kondo effect vs. RKKY interaction) and offers the possibility of exploring the fundamental physics of the two-dimensional system [18]. Analogous to the 2D one, the 1D KLM and HLM will have a superlattice structure with nanofabrication techniques [19, 20]. However, to our knowledge these systems are not realized in condensed-matter systems. Nevertheless, it could be explored with the ytterbium atoms confined in a one-dimensional optical superlattice. Therefore, the new model has three parameters: the ratio of the exchange coupling and optical superlattice to the hopping-matrix element (J/t, V/t), and the density of the delocalized atoms (n). We analyzed a ground-state phase diagram of the HLM, where the number of delocalized atoms is one third of the system sites ($n=1/3$), using the density matrix renormalization group method DMRG [21].

We end this section with the features of the ytterbium atoms and the optical lattice. Section 2 explain the Hamiltonian

model. Section 3 shows the result for the HLM, and section 4 summarizes our results.

Recently papers [16, 22] have used the KLM to explored the magnetic transition of ytterbium (Yb) atoms confined in optical lattice. The stables isotopes of this element are ^{168}Yb, ^{170}Yb, ^{171}Yb, ^{172}Yb, ^{173}Yb, ^{174}Yb and ^{176}Yb. For experimental studies of the Fermi gases two fermionic isotopes are used: ^{171}Yb and ^{173}Yb with nuclear spin $I = 1/2$ and $I = 5/2$ [11]. The first has two different internal states: $I = F = 1/2$, then $2F + 1 = 2$. Hence, the ^{171}Yb can be used to simulated the KLM, which allows two degrees of freedom for each band, either spin up or spin down [23]. Furthermore, the atoms exhibits electronic state dependence: the metastable excited state $^3P_0$ and the ground state $^1S_0$, which posses no electron spin and thus no hyperfine interaction with the nuclear spin. Therefore, the nuclear spin strongly affects the interaction solely between these atoms [24, 25].

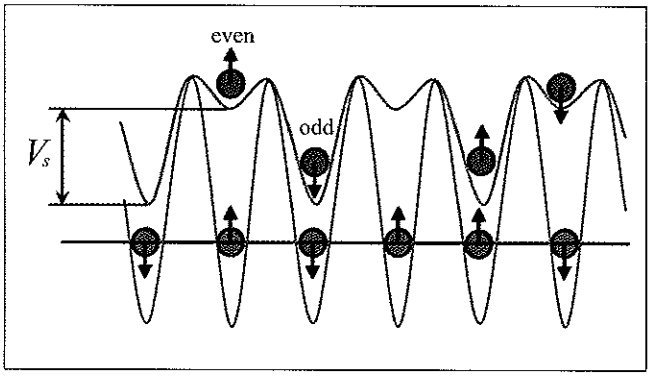

Figure 2. (Color online) HM plus a superlattice potential for delocalized atoms.

The optical lattice is formed by the interference of two or more laser beams. The electric field provided by the oscillating light from a laser, interacts with the dipole moment in the atoms, creating a trapping potential [26] $V(x) \sim I \sin(2x\lambda)$, where I is the intensity and λ the wavelength of the laser beam. Therefore, the atoms can be trapped in a bright interference pattern. Thus, independent storage associate with the ground state $^1S_0$ (g) and transport associate with the metastable excited state $^3P_0$ (e) are created, where the ytterbium atoms can be trapped in two different optical lattice potential with the same periodicity. Furthermore, it is possible to form periodic 1D, 2D and 3D spatial structures and different kinds of potentials can be constructed: harmonic, anharmonic and superlattice. This last kind consists of a superposition of two laser beams along the same direction with different wavelengths, obtaining different periodicities and potential depth on the sites. In Fig. 2, the optical superlattice (red line) is associate with the $^1S_0$, and the other optical lattice (blue line) is associate to the $^3P_0$.

2. Model

The separation and the deepth of the sites and supersites (even and odd in Fig. 2) throughout the optical superlattice define the interaction between the ultracold fermionic atoms and give rise to strongly a correlated system, which can be analyzed with the Anderson lattice Hamiltonian, the Hubbard model and the KLM. If a short-range superlattice potential is applied to this last model, the system can be simulated by means of localized atoms (blue line, Fig. 2) coupled with the delocalized atoms at the sites and supersites (red line, Fig. 2), where no interaction exists between them. Moreover, the model may exhibit two cases for the coupling: the "Kondo" model with $J < 0$ (antiferromagnetic) and the "Hund" model with $J > 0$ (ferromagnetic). In the present paper, we analyzed the last case where the delocalized atoms are confined in a one-dimensional optical superlattice whose Hamiltonian has the form:

$$\begin{aligned} H &= -t\sum_{i,\sigma}\left(\hat{c}^{\dagger}_{i,\sigma}\hat{c}_{i+1,\sigma} + \text{h.c}\right) \\ &\quad -J\sum_{i,\sigma,\beta}\left(\hat{c}^{\dagger}_{i,\alpha}\mathbf{\acute{o}}_{\alpha\beta}\hat{c}_{i,\beta}\bullet\mathbf{S}_i\right) \\ &\quad +\sum_{i,\sigma}V_i\hat{n}_{i,\sigma} \end{aligned} \tag{1}$$

The first term represent the kinetic energy of delocalized atoms hopping between nearest-neighbor sites, where $\hat{c}^{\dagger}_{i,\sigma}\left(\hat{c}_{i+1,\sigma}\right)$ are the creation (annihilation) operators for one atom at the site i with spin $\sigma(=\uparrow,\downarrow)$ and t is the hopping amplitude. The second term represent the local Heisenberg interaction, where J is the coupling Hund, $\mathbf{\acute{o}}$ is the Pauli matrix and $\mathbf{S}_i$ is a localized spin operator 1/2. We assume that t is set to 1.

The third term represents the one-dimensional optical superlattice potential. Here, $\hat{n}_{i,\sigma} = \hat{c}^{\dagger}_{i,\sigma}\hat{c}_{i,\sigma}$ represent the local density of the delocalized atoms. V_i determines the optical superlattice potential, being the difference between the odd and even sites defined with two sites periodicity. In the present paper, $V_s = V$; therefore, $V_i = V$ for odd sites and $V_i = 0$ for even sites (Fig. 2), which denotes the shift in the energy levels for each site. When $V_s = 0$ Eq. 1 returns to the HLM Hamiltonian.

Since we study a one-dimensional many-body system in the ground state, the density matrix renormalization group method (DMRG) is applied in order to study the Hamiltonian (1), when the number of delocalized atoms is one third of the localized atoms.

3. Result

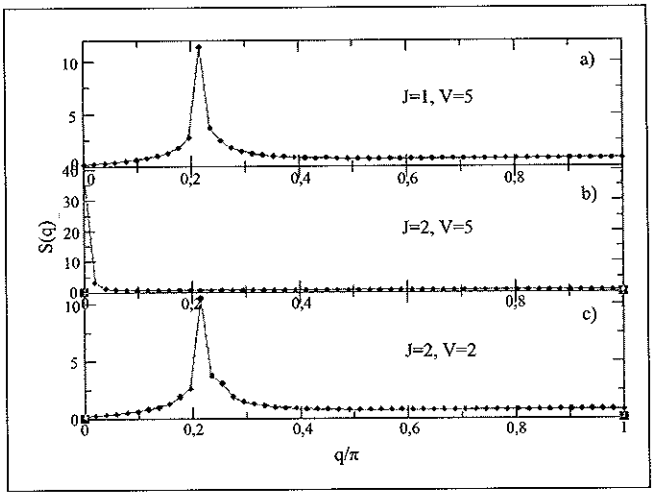

Figure 3. (Color online). Spin structure factors of ytterbium (Yb) atoms in a superlattice potential with lattice size $L = 102$, and $N = 34$ delocalized atoms. a) and c) represent a paramagnetic phase at $J = 1$, $V = 5$ and $J = 2$, $V = 2$. b) exposed a ferromagnetic phase at $J = 2$, $V = 5$.

The magnetic phase diagram of the KLM and Hund models for a partially filled system has been calculated through the spin structure factor [14], defined as the local spin-spin correlation function and its Fourier transform. We used this argument for the same purpose, which can be written as:

$$S(q) = \frac{1}{L}\sum_{j,k} e^{iq(j-k)} \left\langle \mathbf{S}_j^T \cdot \mathbf{S}_k^T \right\rangle \qquad (2)$$

L represent the lattice sites and $\mathbf{S}_j^T = \sum_{\alpha,\beta} \hat{c}_{j,\alpha}^{\dagger} \boldsymbol{\sigma}_{\alpha\beta} c_{j,\beta}^{\dagger} + \mathbf{S}_j$ is the total spin at the site j (Fig. 2). When Eq. 2 shows a peak at $q = 0$, the system indicates an alignment of the total spin or *ferromagnetic state*. The paramagnetic state exhibits a maximum at a q-value between 0 and π.

The Hund model for the case $n = 1/3$ exhibits a ferromagnetic phase at $J \geq 5$ (Fig. 1), which is highlighted for a maximum value or peak of $S(q)$ at $q = 0$. However, we observed this phase at $J = 5$ when the model is subjected to a superlattice potential. This can be seen in Fig.3b, in which we consider $J = 2$ and $V = 5$, for $L = 102$ sites and $m = 200$ states per block. The confinement of the delocalized atoms at the odd sites increases with the potential, reducing the tunneling and the kinetic energy and favoring local ferromagnetic coupling.

If the local ferromagnetic coupling is fixed and the potential decreases, we expect that the system will show a paramagnetic phase when $J = 2$. Fig. 3c shows the maximum spin structure factor at $q \approx 0.2$ for $V = 2$, indicating that the system evolves to a paramagnetic phase.

Now, we vary the ferromagnetic coupling and fix the potential. Comparing the figures 3a and 3b, the maximum value of $S(q)$ has a paramagnetic order at $J = 1$ and a ferromagnetic order at $J = 2$, for $V = 5$. This occurs by means of Hund's rule coupling, in which if J increased the delocalized atoms force the localized atoms to align in the same direction favoring the ferromagnetic phase. Therefore, the probability of the delocalized atoms being aligned parallel to the localized atoms at each site increases.

With Fig. 3, we conclude that the system evolves from a paramagnetic to ferromagnetic phase, which can be tuned by varying the local coupling or the potential strength.

The weight of the peak of the spin correlation $S(q)_{max}$ represents the magnetic order of the system. In Fig.4a, the potential is fixed and the coupling changes. For $J = 1$ (red line), $S(q)_{max}$ increases slowly and is finite at the thermodynamic limit, indicating that the paramagnetic state is stable. For a larger coupling (blue line), the maximum of the spin structure factor increases as a function of the lattice size. For these parameters, the system is in a ferromagnetic state; hence this result indicates to us that the system remains in this state and that the magnetic order is not due to the finite size effects.

Keeping in mind Fig 3, we explored several values of the potential and the coupling, indicating a magnetic phase transition. In Fig 5, we change the potential, finding the points of the coupling at which the transition occurs; in this figure, we demonstrate the propagation of the ferromagnetic area when the potential is increased. Furthermore, we analyzed the situations when $V = 0$ and $V \to \infty$. The first case represents the HLM without potential, in which the transition phase occurs at $J \geq 5$ (Fig. 1). The critical point in Fig. 5 is $J_c(V = 0) = 4.964 \pm 0.085$, which is in agreement with the previous result [19]. The second case indicates that the ferromagnetic phase can be obtained for low values of the coupling, where the critical point at which the transition occurs acquires a constant value.

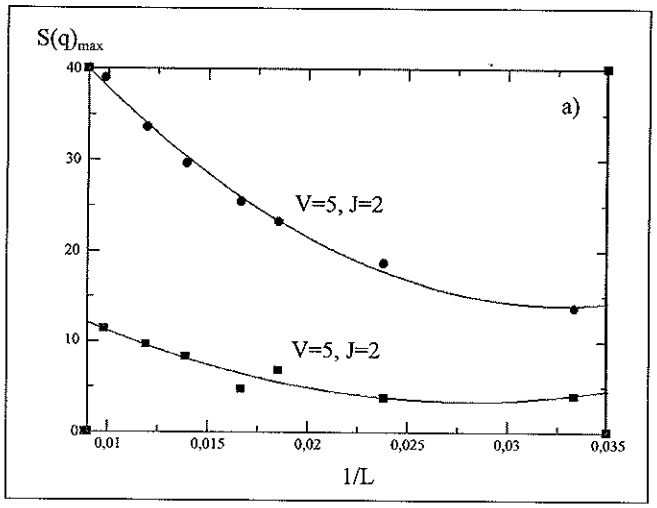

Figure 4. (Color online) The peak weight $S(q)$ a) for the ferromagnetic ($J = 2$) and paramagnetic ($J = 1$) cases at $V = 5$.

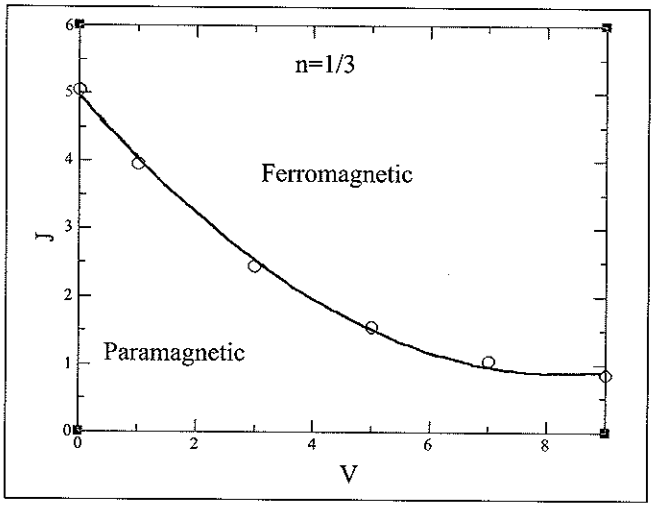

Figure 5. (Color online). Magnetic phase diagram of Ytterbium atoms for the Hund model with superlattice potential. The number of the delocalized atoms is a third of the localized magnetic moment: $n = 1/3$.

Conclusions

We considered the number of delocalized atoms to be one third of the lattice size, and adopted the density matrix renormalization group technique to find the ground-state wave function of the Hund model plus a superlattice potential. We showed the magnetic phase diagram, in which the system increases the ferromagnetic phase with the potential, while the critical coupling decreases. This is caused by Hund's rule coupling, in which if the coupling is strong, an alignment of the delocalized spin with localized spin exists. Furthermore, the spin structure factor exhibits a ferromagnetic ordering of the total spins if the coupling increases for any value of the potential, favoring the ferromagnetic phase. Moreover, the ferromagnetic or paramagnetic ordering is maintained at the thermodynamic limit $L \to \infty$.

References

[1] **Greiner, M., Mandel, O., Esslinger, T, Hänsch, T. W., Bolch, I,** 2002, Quantum phase transition from a superfluid to a Mott insulator in a gas of ultracold atoms, Nature 415, 39.

[2] **Schneider, U., Hackermüller, L., Will, S., Best, Th., Bloch, I., Costi, T.A., Helmes, R. W., Rash, D.**, 2008, Metallic and Insulating Phases of Repulsively Interacting Fermions in a 3D Optical Lattice, Science 322, 1520.

[3] **Jördens, R., Strohmaier, N., Günter, K., Moritz, H., Esslinger, T.**, 2008, A Mott insulator of fermionic atoms in optical lattice, Nature 455, 204.

[4] **Jané, E., Plenio, M. B., Jonathan, D.**, 2002, Quantum-information processing in strongly detuned optical cavities, Phys. Rev. A 65, 050302.

[5] **Courteille, Ph., Freeland, R. S., Heinzen, D. J.**, 1998, Observation of a Feshbach Resonance in Cold Atom Scattering Phys. Rev. Lett. 81, 69.

[6] **Markus, O., Greiner, M., Widere, A., Rom, T., Haensch T. W., Bloch, I.**, 2013, Coherent transport of neutral atoms in spin-dependent optical lattice potentials, cond-mat/0301169

[7] **Jaksch, D., Cirac, J. I., Zoller**, P., 2002, Dynamically turning off interactions in a two-component condensate, Phys. Rev. A 65, 033625.

[8] **Guidoni, L., Verkerk, P.**, 1998, Direct observation of atomic localization in optical superlattices, Phys. Rev. A 57, R1501 (1998); Gorlitz, A., Kinoshita, T., Hansch, T. W., Hemmerich, A., 2001, Realization of bichromatic optical superlattices, ibid. 64, 011401.

[9] **Gorshkov, A.V., Hermele, M., Gurarie, V., Xu, C., Julienne, P.S., Ye, J., Zoller, P., Demler, E., Lukin, M.D., Rey, A.M.**, 2010, Two-orbital Su(N) magnetism with ultracold alkaline-earth atoms, Nature Phys. 6 289.

[10] **Kugel, K.I., Khomskii, D.I.**, 1973, Crystal Structure and magnetic properties of substance with orbital degenerecy, Sov. Phys. JETP 37 725.

[11] **Manmana, S.R., Hazard, K. R. A., Chen, G., Feiguin, A.E., Rey, A. M.**, 2011, SU(N) magnetism in chains of ultracold alkaline-earth-metal atoms: Mott transitions and quantum correlations Phys. Rev. A 84 043601.

[12] **Tsunetsugu, H., Sigrist, M., Ueda, K.**, 1997, The ground-state phase diagram of the one-dimensional Kondo lattice model, Rev. Mod. Phys. 69 809.

[13] **Shibata, N., Ueda, K., 1999** J. Phys.: Condens. Matter 11 R1.

[14] **Garcia, D. J., Hallberg, K., Alascio, B., Avignon, M.**, 2004, Spin Order in One-Dimensional Kondo and Hund Lattices, Phys. Rev. Lett. 93, 177204.

[15] **Tsunetsugu, H., Hatsugai, Y., Sigrist, M.**, 1992, Spin-liquid ground state of the half-filled Kondo lattice in one dimension Phys. Rev. B 46, 3175.

[16] **Peters, R., Kawakami, N.**, 2012, Ferromagnetic state in the one-dimensional Kondo lattice model, Phys. Rev. B 86, 165107.

[17] **Foss-Feig, M., Hermele, M., Gurarie, V., Rey, A. M.**, 2010, Pro-

bing the Kondo lattice model with alkaline-earth-metal atoms, Phys. Rev. A 81, 053624.

[18] **Shishido, H., Shibauchi, T., Yasu, K., Kato, T., Kontani, H., Terashima, T., Matsuda, Y.**, 2010, Tuning the Dimensionality of the Heavy Fermion Compound CeIn3, Science 372, 980.

[19] **Kim, S., Razegi, M.**, 2001: Advances in quantum dot structures. In: Processing and Properties of Compound Semiconductors, ed. by Willardson, K., Weber, E.R., Academic, New York.

[20] **Babak Ziaie, Antonio Baldi, Massood Z. Atashbar**, 2010: Introduction to micro-/Nanofabrication. In: Springer Handbook of Nanotechnology, ed. by Bhushan, B., Springer Berlin Heidelberg.

[21] **White, S. R.**, 1992, Density matrix formulation for quantum renormalization groups, Phys. Rev. Lett. 69, 2863.

[22] **Silva-Valencia, J., Franco, R., Figueira, M.S.**, 2013, Quantum phase transition of alkaline-earth fermionic atoms confined in an optical superlattice Physics Letters A. 377, 643.

[23] **Gulacsi, M.**, 2004, The one-dimensional Kondo lattice model at partial band filling, Advances in physics 53, 769.

[24] **Hayes, D., Julienne, P. S., Deutsch, I. H.**, 2007, Quantum Logic via the Exchange Blockade in Ultracold Collisions, Phys. Rev. Lett. 98, 070501.

[25] **Daley, A. J. , Boyd, M. M., Ye, J., Zoller, P.**, 2008, Quantum Computing with Alkaline-Earth-Metal Atoms, Phys. Rev. Lett. 101, 170504.

[26] **Grimm, R., Weidemuller, M. Ovchinnikov, Y. B.**, 2000, Optical dipole traps for neutral atoms. Adv. At. Mol. Opt. Phys. 42, 95-170.

[27] **Millis, A. J., Littlewood, P. B., and Shraiman, B. I.**, 1995, Phys. Rev. Lett., 74, 5144.

MORPHOLOGICAL AND STRUCTURAL ANALYSIS OF CERAMIC MATERIALS COMPOSITE BY KAOLINITE AND ALUMINA

ANÁLISIS MORFOLÓGICO Y ESTRUCTURAL DE MATERIALES COMPÓSITOS CERÁMICOS DE KAOLINITA Y ALÚMINA

A.F. Guzmán[*], D.A. Landinez Téllez[**], J. Roa-Rojas[,1], F. Fajardo[*].**

ABSTRACT

Guzmán A.F., D.A. Landinez Téllez, J. Roa-Rojas, F. Fajardo. Morphological and structural analysis of ceramic materials composite by Kaolin and Alumina. Rev. Acad. Colomb. Cienc., 37 (1): 50-54, 2013. ISSN 0370-3908.

In this work, we report the preparation, structural and electrical characterization, morphological analysis and hardness measurements of ceramic materials composed of kaolinite $Al_2(Si_2O_5)(OH)_4$ and alumina Al_2O_3. Samples were prepared from mixtures of precursor oxides starting with 100% alumina and increased the kaolinite concentration on steps of 10% up to complete 100% of kaolinite. The samples were sintered by the method of solid state reaction at temperatures of 1150, 1250 and 1350 °C. We found that the alumina samples are stable at the different temperatures of synthesis. The samples of kaolinite at 100% suffer a change phase depending on the sinterization temperature, noting that at 1350 °C yields 87% mullite and 13% cristobalite. The presence of quartz was only detected in samples with 100% kaolinite for sinterization temperatures of 1150 and 1250 °C. All samples with a mixture of alumina and kaolinite showed the presence of mullite, which is increased when the content of kaolinite is high or when the sinterization temperature is increased. This allows us to infer that the introduction of alumina optimizes the process of mullite formation by their reaction with the SiO_2 that remainder from the kaolinite. The sample with 100% alumina has a Mohs hardness of about 5, and this is increased with the content of kaolinite, until a Mohs hardness of about 6 to the sample with 100% kaolinite. The dielectric constant of these materials is around 27.82.

Key words: Ceramics, kaolinite, mullite, alumina.

RESUMEN

En este trabajo reportamos la preparación, la caracterización eléctrica y estructural, el análisis morfológico y las medidas de dureza de materiales compuestos de caolinita $Al_2(Si_2O_5)(OH)_4$ y alúmina Al_2O_3. Las muestras fueron preparadas a partir de mezclas de óxidos precursores iniciando con 100% de alúmina, la concentración

* Grupo de Estudio de Materiales, Departamento de Física, Universidad Nacional de Colombia, Bogotá, Colombia.

** Grupo de Física de Nuevos Materiales, Departamento de Física, Universidad Nacional de Colombia, Bogotá, Colombia. E-mail: jroar@unal.edu.co

de caolinita se fue incrementando en pasos de 10% hasta completar el 100%. Las muestras fueron sinterizadas por el método de reacción de estado sólido a las temperaturas de 1150, 1250 y 1350 °C. Se encontró que las muestras de alúmina son estables a las diferentes temperaturas de síntesis. Las muestras de caolinita al 100% sufren un cambio de fase dependiendo de la temperatura de sinterizado, encontrando que a 1350 °C se produce 87% de mullita y 13% de cristobalita. La presencia de cuarzo fue solamente detectada en muestras con 100% de caolinita para temperaturas de sinterizado de 1150 y 1250 °C. Todas las muestras con una mezcla de alúmina y caolinita muestran las presencia de mullita, la cual se incrementa cuando el contenido de caolinita es alto o cuando se incrementa la temperatura de sinterizado. Esto nos permite inferir que la introducción de alúmina optimiza el proceso de formación de mullita debido a la reacción del SiO_2 que sobra de la caolinita. La muestra con 100% de alúmina tiene una dureza Mohs de aproximadamente 5, y está se incrementa con el contenido de caolinita, hasta alcanzar una dureza de cerca de 6 para la muestra con 100% de caolinita. La constante dieléctrica de estos materiales es de aproximadamente 27.82.

Palabras clave: Cerámicos, caolinita, mullita, alúmina.

1. Introduction

In recent years, the study of ceramic materials has been particularly important because the stability of their mechanical and physical properties at high temperatures which is especially useful for technological applications (**Aksay & Dabbs**, 1991). The development of research on ceramic materials is significant because, among other factors, the metallurgical production worldwide has a projection to decrease, which enables the ceramic to be an adequate substitute for applications based on metals. In some cases the production of ceramics have disadvantages such as large sintered-drying time and high manufacturing costs that prevent processing at industrial level (**Heimann**, 2010). One of the main difficulties on the synthesis of ceramic materials is the use of crucibles which remain chemically stable relative to the material that is produced (**Weber & Thompson**, 1957). For this reason, it is necessary to investigate methods to obtain ceramic materials in a controlled and efficient form, in order to reduce processing time and costs.

In recent decades, research on alumina-silicate ceramic materials has increased especially on mullite. Studies on raw materials, processing, heat treatment and mechanical behavior, among others, have been reported (Carty, 1998). Some of these studies have focused on the production of metakaolin in order to evaluate its performance as a function of the mineralogical composition (48-97%) of kaolinite (Burgoš, 2008). Furthermore, various concentrations of kaolinite have been tried at calcinations temperatures ranging from 700 to 1.600 °C for various heating times to examine the nucleation phenomenon of mullite; and mixtures of kaolinite have been treated with additives like silicic acid and aluminum hydroxide in order to achieve complete conversion to mullite (Schneider *et al.*, 2008). Fabrication of mullite refractory parts has been studied using some binders with aluminum phosphate and chromium, in order to compare the results with those obtained from commercial refractory mullite, clay and alumina (Torres & Mejía, 2007). Moreover, investigations have been developed that seek to create ceramic molds for use in some tests such as directional solidification of aluminum alloys; for which different concentrations of silica, bentonite, kaolinite, feldspar and several process for drying and thermal sintering were used (Rossíni & Arazi, 1970).

In this work we report the synthesis and characterization of structural, morphologic and hardness properties of ceramic materials composed by kaolinite $Al_2(Si_2O_5)(OH)_4$ and alumina (Al_2O_3) using the solid state reaction procedure and X-ray diffraction analysis (XRD), hardness measurements and electrical response.

2. Experimental

Samples were prepared from precursor powder oxides of alumina with substitutions of kaolinite from 0 to 100% (with increments of 10%), which were pressed to form pallets of *2.5 cm* diameter. Samples were dried in air and sintered at *1150, 1250, 1300* and *1350 °C* for *15 hs*. Structural characterization was carried out by using a Panalytical X-Pert PRO MPD diffractometer with CuKα (1,540598 Å). Refinements of the experimental data were performed through the GSAS and PowderCell 2.4 codes. From the X´Pert Highscore semiquantitative concentrations of samples were determined. Polarization curves were measured through a Radiant Technologies Polarimeter.

3. Results and Discussion

Figure 1 exemplifies the characteristic XRD results obtained for several concentrations of kaolinite in the samples sintered at 1350 °C. It can be seen that the intensity of the characteristic peaks of alumina (2Θ = 25.69, 35.16 and 43.43) decreases depending on the amount of kaolinite present in the samples. From the concentration of 20% kaolinite the diffraction pattern reveal the appearance of the characteristic

peaks of mullite (2Θ = 16.47, 26.91, 30.99 and 33.23) (Meng & Peng, 2013). For kaolinite concentrations above 90% traces of cristobalite and quartz are identified in the same angular positions reported for sintering temperatures of 1100 °C (Chen & Lan, 2000).

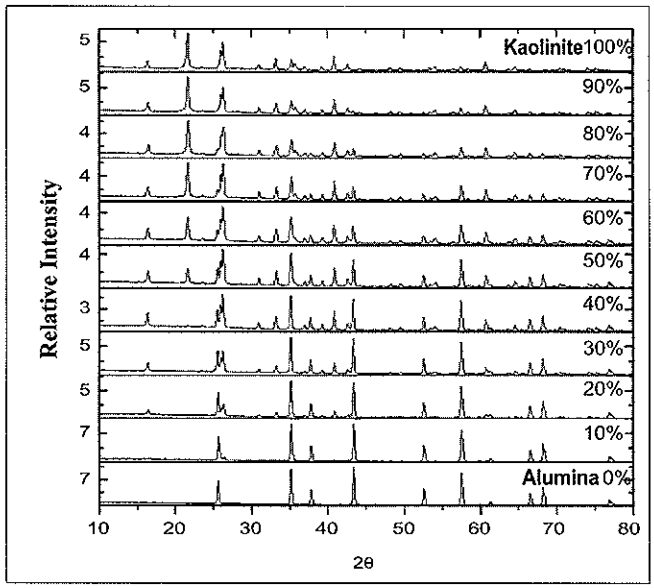

Figure 1: XRD pattern for alumina-kaolinite samples sintered at 1350 °C for several concentrations of kaolinite.

Using the semiquantitative phase analysis for the samples sintered at 1350 °C the weight percentage of the phases as a function of the kaolinite concentration were found as shown in Figure 2. It is observed that the weight percentage of cristobalite and mullite increases with the concentration of kaolinite. For all the sintering temperatures used in this work was determined that the weight percentage of cristobalite increases when we going from 90% to 100% kaolinite, which indicates that some percentage of the alumina reacts with the cristobalite that is produced after the process of mullite nucleation (**Rossíni & Arazi**, 1970). The presence of quartz was only detected in samples with 100% kaolinite for sinterization temperatures of 1150 and 1250 °C.

Also a systematical study of the effect of sintering temperature on the structure of the ceramics was performed as shown in figure 3. Comparing the x-ray diffraction patterns of the mixtures after the compaction and the sintering process is observed the phase transformation from kaolinite to mullite. Note the disappearance of the characteristic peaks of kaolinite (2Θ = 12.41 and 24.97), result that is consistent with those reported by other authors (**Torres & Castelló**, 2011). Figure 4 shows the dependence of the weight percentage of the different phases as a function of the sintering tempera-

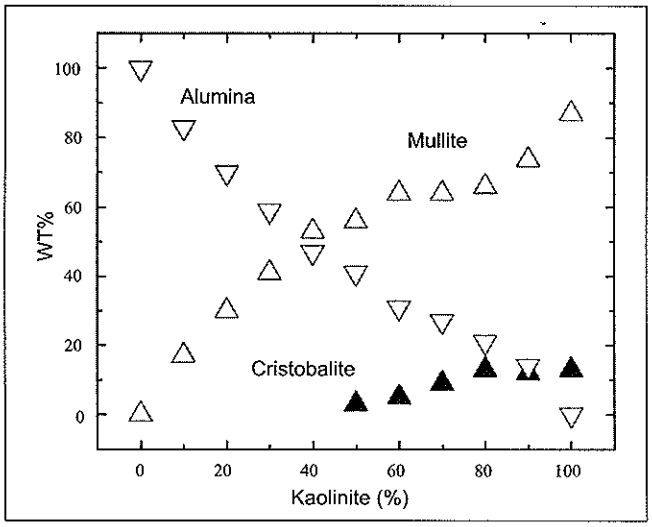

Figure 2: Weight percentage of the phases as a function of the kaolinite concentration for the alumina-kaolinite samples sintered at 1350 °C.

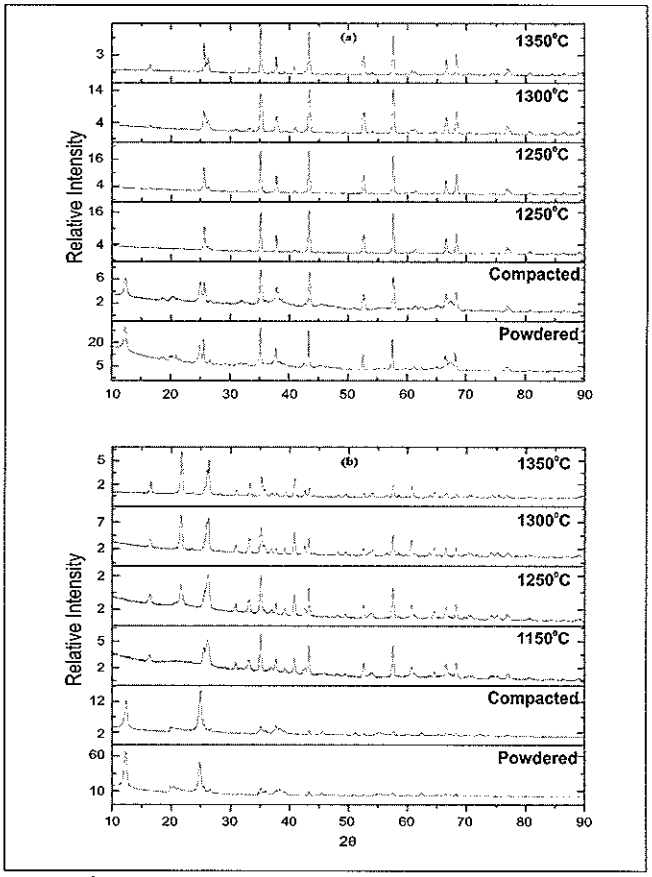

Figure 3: Diffraction patterns of samples prepared at several sintering temperatures for a) 20% and b) 80% of kaolinite. For comparison the patterns of the powdered and compacted samples before the sinterization process are also shown.

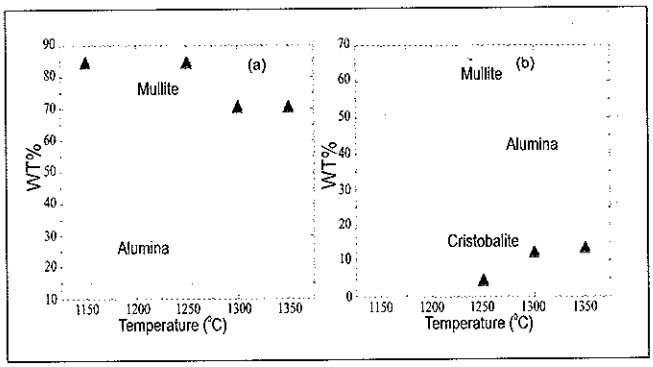

Figure 4: Quantitative analysis of the weight percentage of the phases as a function of the sintering temperature for a) 20% and b) 80% of kaolinite.

ture, for the samples prepared with 20% and 80% kaolinite. For the samples with 80 % of kaolinite was observed that as the sintering temperature increases the mullite concentration increases, which may be due to the presence of cristobalite.

Hardness analysis of these materials was performed by abrasive wear test. For this test we use an experimental setup consisting of a rotating disk with oxide aluminum sandpaper on the top that have 180 granules per square centimeter.

Figure 5 shows in a semi logarithmic scale the abrasive wear as a function of the percentage of kaolinite used for the material sintering at a temperature of *1350 °C*. Notice how the wear resistance of the material is improved as the kaolinite concentration increases. This result can be explained as due to the growth of the weight percentage of mullite and cristoballite when the kaolinite concentration increases, as shown in figure 2.

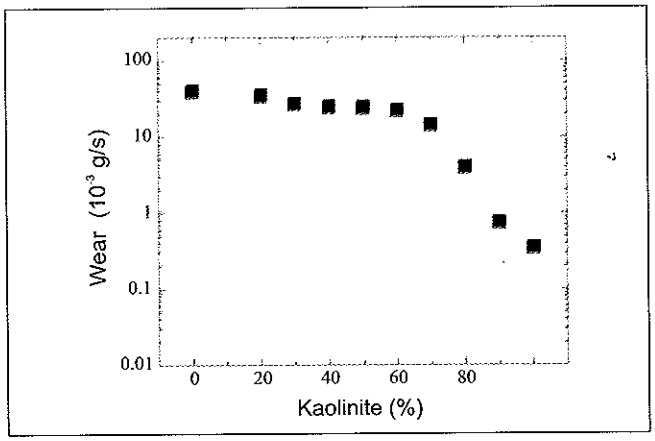

Figure 5: Abrasive wear dependence as a function of the kaolinite concentration. The sintering temperature of the material was 1350 °C.

From a comparative analysis with known hardness materials, we found that the sample with 100% alumina has a Mohs hardness of about 5 which increases with the content of kaolinite, until a Mohs hardness of about 6 for the sample with 100% kaolinite.

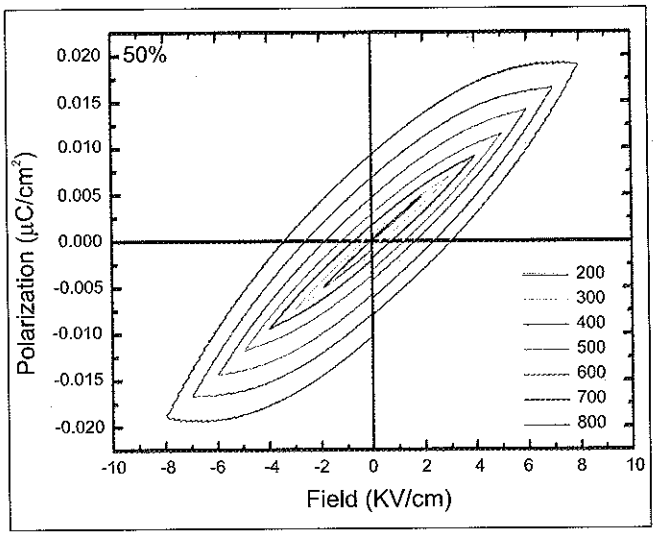

Figure 6: Polarization as a function of the electrical bias field for the sample with 50% of kaolinite, the voltage was changed from *200* to *800 V*.

Table 1: Dielectric constant (ε_r) for each of the voltages used on the measurement of polarization for the sample with 50% of kaolinite. The values of the electric field (E) and the saturation polarization (Ps) of hysteric curves are also shown.

Voltage (V)	E (V/m)*10^5	Ps (C/m^2)*10^{-2}	ε_r
200	1.94	0.005	29.29
300	3.05	0.007	27.61
400	4.02	0.009	27.18
500	5.03	0.012	27.29
600	6.01	0.014	27.78
700	7.01	0.017	27.72
800	7.99	0.019	27.90
Average ε_r		**27.82**	

Figure 6 shows the graph of polarization as a function of the applied field for the sample with a kaolinite concentration of 50%. In this graph are observed hysteresis curves by applying a bipolar triangular signal from *200 V* to *800 V* with *100V* increments. This behavior is evidence of a ferroelectric-like behavior. From the saturation polarization a relative

dielectric constant was obtained for each applied voltage, we found an average of 27.82 as presented in table 1. We notice that the value of the dielectric constant do not varies significantly with the concentration of kaolinite in the samples.

4. Conclusions

The synthesis and structural, morphologic, mechanical and electrical characterization of mullite obtained from alumina and kaolinite precursors were performed. Analyzing the weight percent of the phases present was identified the formation of secondary mullite as result of the transformation of kaolinite in mullite and cristobalite. Hardness test showed that the sintering temperature and the increasing of the kaolinite concentration improve the mechanical properties of the ceramic samples. From the saturation polarization of hysteric curves of polarization as a function of applied fields, the relative dielectric constant for the samples was obtained.

Acknowledgements

This work was partially financed by DIB (Hermes Code 13893) and "El Patrimonio Autónomo Fondo Nacional de Financiamiento para la Ciencia, la Tecnología y la Innovación Francisco José de Caldas" Contract RC No. 0850-2012".

References

Aksay, L. Dabbs, D. 1991. *Mullite for Structural, Electronic, and Optical Applications.* J. Am. Ceram. Soc., **74** (10): 2343-2358.

Burgos, O. 2008. *Síntesis y Procesamiento Coloidal de Nanocomposites de Alúmina-Mullita.* Tesis Doctoral, Instituto de Cerámica y Vidrio (CSIC), Madrid, Universidad Autónoma de Madrid.

Carty, W. 1998. *Porcelain—Raw Materials, Processing, Phase Evolution, and Mechanical Behavior,* J. Am. Ceram. Soc., **81** (1): 3-20.

Chen, C. Lan, G. 2000. *Preparation of mullite by the reaction sintering of kaolinite and alumina.* J. Eur. Ceram. Soc., **20** (14-15): 2519-2525.

Heimann, R. 2010. Classic and Advanced Ceramics, 1 ed, Wiley-VCH Verlag GmbH & Co. KGaA, Weinheim, Germany.

Meng, B. Peng, J. 2013. *Effects of in Situ Synthesized Mullite Whiskers on Flexural Strength and Fracture Toughness of Corundum-Mullite Refractory Materials,* Cerámics International, **39** (2): 1525-1531.

Rossíni, A. Arazi, S. 1970. *Mullitización de Mezclas de Arcilla Caolinítica e Hidróxido de Aluminio.* Boletín de la Sociedad Española de Cerámica, **5**, 579-591.

Schneider, H. Schreuer, J. Hildman, B. 2008. *Structure and properties of mullite.* J. Eur. Ceram. Soc., **28** (2): 329-344.

Torres, J. Mejía, R. 2007. *Influencia de la Composición Mineralógica de los Caolines Sobre el Desempeño de Morteros Adicionados con MK.* DYNA, Revista Universidad Nacional, **74** (153): 61-67.

Torres, J. Castelló, R. 2011. *Análisis Comparativo de Caolines de Diferentes Fuentes para la Producción de Metacaolín.* Revista Latinoamericana de Metalurgia y Materiales, **31** (1): 35-43.

Weber, B. Thompson, . 1957. *Ceramic Crucible for Melting Titanium.* J. Am. Ceram. Soc.**40** (11): 363-373

SYNTHESIS, ELECTRICAL AND STRUCTURAL CHARACTERIZATION OF A COMPOSITE MATERIAL BASED ON POWDERED MAGNETITE AND HIGH DENSITY POLYETHYLENE.

SÍNTESIS Y CARACTERIZACIÓN ELÉCTRICA Y ESTRUCTURAL DE UN MATERIAL COMPUESTO A BASE DE POLIETILENO DE ALTA DENSIDAD Y MAGNETITA PULVERIZADA

A.O. Garzón Posada*, F.E. Fajardo Tolosa, D.A. Landínez Téllez*, J. Roa-Rojas*, G. Peña Rodríguez*****

ABSTRACT

Garzón Posada A.O., F.E. Fajardo Tolosa, D.A. Landínez Téllez, J. Roa-Rojas, G. Peña Rodríguez. Synthesis, electrical and structural characterization of a composite material based on powdered magnetite and high density polyethylene. Rev. Acad. Colomb. Cienc., 37 (1): 55-59, 2013. ISSN 0370-3908.

This work describes the synthesis and characterization of a composite material based on magnetite filled HDPE, which is commonly known for its magnetic properties. Composites of this kind are used in different applications such as magnetic and microwave absorption, transducers manufacturing, and biomedical applications like targeted drug delivery, organs tagging, etc. The samples were produced according to different volume ratios of magnetite and HDPE. The samples structure was analyzed through X-ray diffraction tests and the crystallinity degree was calculated. Then, the samples were electrically characterized through volume resistivity measurements. The results showed that for ratios less than the 20% of magnetite there is not a substantial reduction in the resistivity of the composite compared to the unfilled HDPE. For magnetite ratios above the 30% the composite shows a substantial reduction of six orders of magnitude in its electrical resistivity.

Keywords: Magnetite, volumetric resistivity, High density Polyethylene.

RESUMEN

En este trabajo se describe la síntesis y caracterización de un material compuesto a base de polietileno de alta densidad (HDPE) y magnetita pulverizada, comúnmente conocido por sus propiedades magnéticas. Los compuestos de este tipo se utilizan en diferentes aplicaciones tales como la absorción magnética y de microondas, la elaboración de transductores y en aplicaciones biomédicas como la producción de capsulas para la entrega

* Grupo de Física de Nuevos Materiales, Departamento de Física, Universidad Nacional de Colombia, Bogotá DC, Colombia. E-mail: aogarzonp@unal.edu.co

** Grupo de Estudios de Materiales – GEMA, Departamento de Física, Universidad Nacional de Colombia, Bogotá DC, Colombia.

*** Grupo de Investigación en Tecnología Cerámica, Universidad Francisco de Paula Santander, San José de Cúcuta, Colombia.

focalizada de medicamentos, marcación de órganos, etc. Las muestras del material compuesto fueron producidas con diferentes proporciones en volumen de magnetita y HDPE. La estructura de las muestras se analizó a través de pruebas de difracción de rayos X y se calculó el grado de cristalinidad. Posteriormente las muestras se caracterizaron eléctricamente a través de mediciones de resistividad volumétrica. Los resultados mostraron que para proporciones menores al 20% de volumen de magnetita no hay una reducción sustancial en la resistividad del material compuesto, en comparación con el polietileno de alta densidad puro. Para proporciones de magnetita por encima del 30% el compuesto muestra una reducción sustancial de seis órdenes de magnitud en su resistividad eléctrica.

Palabras Clave: Magnetita, resistividad volumetrica, polietileno de alta densidad.

1. Introduction

This paper aims to produce a composite material based on high density polyethylene (HDPE) with different proportions of powdered magnetite (Fe_3O_4). The HDPE is one of the most used polymers in the world due to its low cost, ease of processing and good performance in addition to being known as a reusable thermoplastic.

During the last decade, many studies have tried to improve the performance of this material for specific applications, adding to the polymeric matrix different kinds of reinforcements like fibers and particulate materials such as the silicates or other ferrimagnetic minerals. For instance, in Colombia the magnetite is an abundant material, economical and easy to achieve due to the good amount of mines found throughout the country, mainly those that are located in Huila and Cundinamarca.

By the addition of silicates such as montmorillonite some researchers have successfully enhanced the mechanical properties of different polymeric matrices; these composites can be used as building block for constructions. In other works the addition of some minerals, like the graphite or magnetite in different proportions into the polymeric matrix, have allowed to study the percolative properties of the composite material, these kinds of studies are useful for the design of technological gadgets such as heat sinks or packages for electronic devices with electromagnetic shielding e (**Panwar et al.**, 2007; **Weidenfeller** et al, 2002). Although the use of magnetite in thermoplastic and thermoset matrices is relatively new, these composites has been implemented in the automotive industry and in some biomedical uses, like the design of stents that can be able to change their shape in the presence of magnetic fields (**Razzaq et al.**, 2007). Some polymers filled with magnetite can also use in pharmaceutical applications including targeted drug delivery, tissue reconstruction and tumor treatments (**Zhang et al.**, 2008), primarily because of the low cytotoxicity of the magnetite [**Miles et al.**, 2010; **Wentao et al.**, 1996].

In this work the samples were synthesized using an extruder plastic machine and its resistivity and crystallinity degree for different concentrations of HDPE and magnetite were studied. Is expected to be achieved a composite with the mechanical properties and excellent machinability of the polymers, along with the conductive and ferromagnetic properties of the magnetite. This composite can be used for the development of technology or biomedical products, using economic and reusable precursors.

2. Experimental

2.1 Samples Preparation

Based on the calculation of the HDPE and magnetite (Fe_3O_4) real densities, samples of filled HDPE with magnetite were obtained with different volume ratios: 90%-10%, 80%-20%, 70%-30%, 65%-35% and 60%-40%. For each volume ratio were prepared two samples.

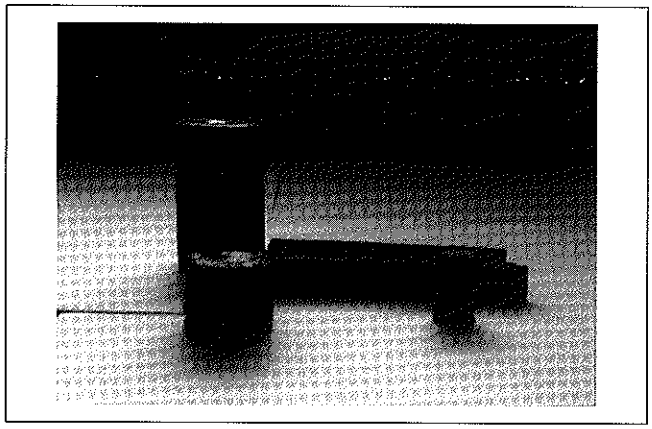

Fig. 1. Samples poured in different shapes.

The samples were made using an extruder plastic machine with three heating zones. After the extrusion process, the composite is poured into various molds with different shapes in order to facilitate the machinability of the samples, as is shown in figure 1.

For the X-ray diffraction tests and for the electrical resistivity measurements, small cylinders of approximately 1.2 mm diameter and 1mm height were cut and polished.

2.2 Resistivity Measurements

It is well known that the electrical resistivity of insulating polymers like de HDPE could decrease by dispersing a conductive filler, for instance, carbon black (CB) throughout the polymer matrix (**Wentao & Xinfang**, 1997; **Tang et al.**, 1994; **Beaucage et al.**, 1999); likewise, the magnetite as filler of polypropylene and polyamides matrices has been shown similar behaviors (**Weidenfeller** et al, 2002).

To assess the effect of the different magnetite ratios into the HDPE matrices, at room temperature, measures of volumetric resistivity were taken. The volumetric resistivity is the resistance to leakage current through the body of an insulating material, is commonly expressed in ohm-centimeters (**ASTM international**, 2007). The resistivity of the samples was measured the 6517A Keithley Electrometer and its 8009 resistivity test chamber.

2.3 X-ray diffraction Tests

The qualitative composition or phase identification of each sample is determined by the X-ray diffraction tests. The degree of crystallinity is estimated by the areas under the diffraction curves. The X'Pert PRO MPD panalytical X-ray diffractometer was used. This equipment uses a copper anode of 1.540998 Å. As analysis software the HighScore plus of panalytical was used.

3. Results and discussion

Fig. 2 shows the volume resistivity of HDPE samples filled with different volume proportions of magnetite, for each volume ratio two samples were measured. As is shown in Fig. 2 the significant drop (six orders of magnitude 10^{14} to 10^{6}) in the resistivity of magnetite filled HDPE can be observed between a filler loading of 30 vol% to 40 vol% as was predicted in previous works (**Weidenfeller et al.**, 2002; **Boettcher**, 1954; **Bruggeman,** 1937) . In contrast to this, the Fig.2 shows a high volume resistivity between the pure HDPE samples and the HDPE filled samples with 20 vol% of magnetite, that's an indicative of the predominant insulating polymeric phase.

The samples resistivity can be affected by some factors like the magnetite particles distribution and its interconnectivity into the HDPE matrix. This is why the samples with a low volume fraction of magnetite (0 vol% - 20 vol%) have a high volume resistivity, with a low magnetite particles dispersion, the resistivity is expected to be high and no conductive paths are available between the magnetite particles.

This behavior, the decrease of the resistivity between filler loadings of 30% to 40% of magnetite, and the increase of it between the pure HDPE to 20% of filler loading was also confirmed by electromagnetic polarization measures.

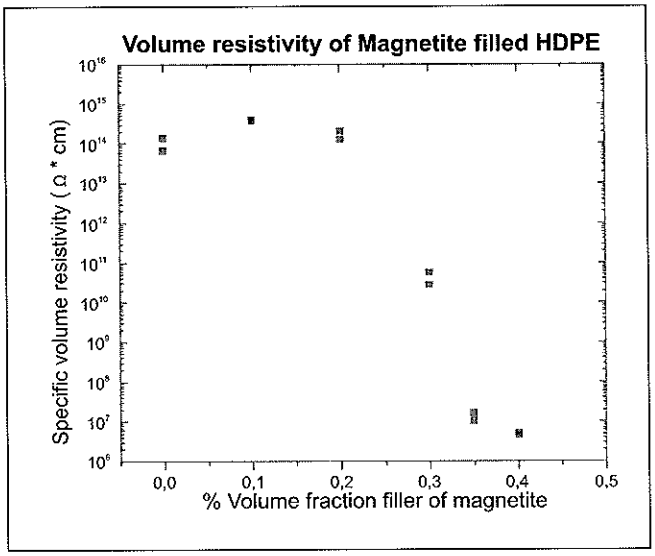

Fig.2. Specific volume resistivity of extruded and molded magnetite filled HDPE as a function of the percent of volume fraction filler of magnetite. For each volume ratio were prepared and measured two samples.

On the other hand, in the samples with the highest filler content (30 vol% - 40 vol%) some particles seem to have contacts points among them or are separated only by very small gaps, that produces conducting paths according to the theories of **Boettcher** (1954) and **Bruggeman** (1937). This indicates an ideally and homogenous dispersion of the magnetite particles in the polymeric matrix of HDPE. Therefore charge carriers can migrate from one magnetite particle to a neighboring one by hopping or tunneling. It's also possible according to the figure 2 make an approximation of the percolation threshold for the magnetite filled HDPE samples near to the 30 vol%.

Figure 3 shows the diffraction pattern of the pure magnetite, this describes the normal crystalline behavior of the ferrites. Figure 4 shows the diffraction patterns of each sample. Excepting the unfilled HDPE and the pure Magnetite it was observed three main phases: Magnetite, Hematite and HDPE. The Hematite phase belongs to the magnetite used as precursor material for the experiments and was not previously isolated.

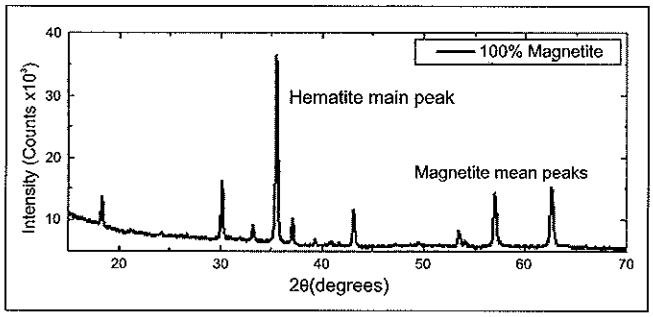

Fig. 3. Pure magnetite diffraction pattern.

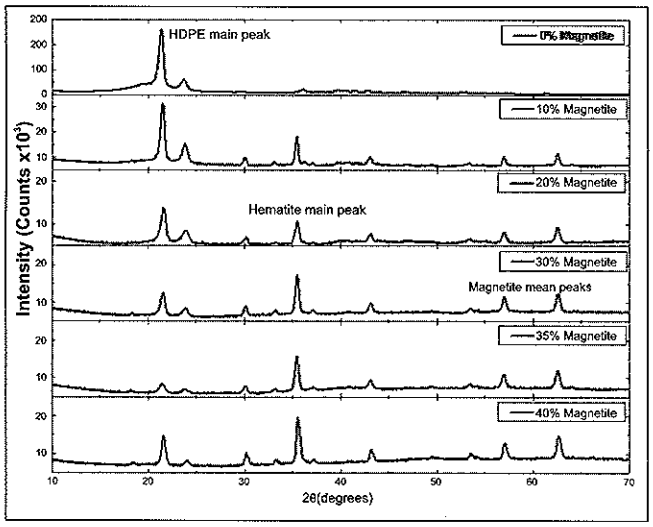

Fig. 4. Diffraction patterns of the magnetite filled HDPE samples.

As was expected, when the content of the magnetite is increased into the composite, the main peaks of the magnetite and hematite phases becomes more significant, while the main peak of the HDPE phase is gradually reduced (300.000 to 15.000 counts), in other words the degree of amorphousness decreases. The percentage of crystallinity for each diffraction pattern is measured as the ratio of the crystalline area over the total area, and the results are summarized in Table 1. Note that the percentage of crystallinity is higher as the volume of the magnetite increases.

Conclusions

Electrical and structural properties of magnetite filled HDPE samples were investigated. Samples were prepared with different volume ratios of magnetite. Electrical resistivity measurements show a rapid drop for filler loadings of the HDPE over the 30 % of volume, it is a result of point contacts between magnetite particles which are surrounded by the HDPE matrix. The increasing number of magnetite particles can be

Table 1. Magnetite filled HDPE samples degree of cristallinity.

% Vol Magnetite	% Cristallinity
0 %	16 %
10 %	24,4 %
20 %	22,4 %
30 %	24,5%
35 %	27 %
40 %	27,4 %

confirmed through the diffraction patterns and the cristallinity degree. The structural changes in the composite started with 20 vol% of filler. Therefore, the resistivity values of the investigated materials mainly depend on the magnetite grade.

Acknowledgements

This work was partially financed by DIB (Hermes code 13893) and "El Patrimonio Autónomo Fondo Nacional de Financiamiento para la Ciencia, la Tecnología y la Innovación Francisco José de Caldas" Contract RC No. 0850-2012

References

ASTM international 2007. Standard Test Methods for DC Resistance or Conductance of Insulating Materials. ASTM D257 – 07. **V10.0.** ICS Number Code: 29.035.01

Beaucage G., Rane S., Schaefer D.W., Fisher G. 1999. Morphology of polyethylene-carbon black composites. Journal of polymer science polymer physics **37**(11) 1105-1119.

Boettcher CJF. 1952. Theory of electric polarization. Elsevier, Amstterdam **Vol 1.** 415 pp.

Bruggeman DAG. 1937. Berechnung verschiedener physikalischer Konstantenvon heterogenen Substanzen. III. Die elastischen Konstanten der quasiisotropen Mischkörper aus isotropen Substanzen. Annalen der Physik **421**(2): 160–178.

Miles W.C., Goff J.D., Huffstetler P.P., Mefford O.T., Riffle J.S., Davis R.M. 2010. The design of well-defined PDMS–Magnetite complexes. Polymer, **51**(2): 482-491.

Panwar V., Sachdev V.K., Mehra R.M. 2007. Insulator conductor transition in low-density polyethylene–graphite composites. European Polymer Journal **43**: 573-585 .

Razzaq M., Anhalt M., Frormann L., Weidenfeller B. 2007. Thermal, electrical and magnetic studies of magnetite filled polyurethane shape memory polymers. Materials Science and Engineering **444** (1-2): 227-235.

Tang H., Liu Z.Y., Piao J.H., Chen X.F., Lou Y.X. 1994. Electrical behavior.of carbon black-filled polymer composite; effect of interaction between filler and matrix. Journal of Applied Polymer Science **51**(7): 1159-1664.

Weidenfeller B., Hoferb M., Schilling F. 2002. Thermal and electrical properties of magnetite filled polymers. Composites **33**(8): 1041-1053.

Wentao J., Xinfang C. 1997. Effect of polymer-filler interactions on PTC behaviors of LDPE/EPDM blends filled with carbon blacks. Journal of Applied Polymer Science **66**(10): 1885–1890.

Wentao J., Xinfang C., Shubua L. 1996. Effects of irradiation on PTC performance of LDPE/EPDM blends filled with carbon blacks. Journal of Applied Polymer Science **60**(13): 2317-2320.

Zhang J., Rana S., Srivastava R.S., Misra R.D.K. 2008. On the chemical synthesis and drug delivery response of folate receptor-activated, polyethylene glycol-functionalized magnetite nanoparticles. Acta Biomaterialia **4**(1): 40-48.

MORPHOLOGICAL, STRUCTURAL AND MAGNETIC CHARACTERIZATION OF BLACK SANDS OF THE GUAJIRA – COLOMBIA

CARACTERIZACIÓN MORFOLÓGICA, ESTRUCTURAL Y MAGNÉTICA DE ARENAS NEGRAS DE LA GUAJIRA – COLOMBIA

Johana Patricia Parra Sua*, Carlos Andrés Sjogreen Blanco, José Edgar Alfonso Orjuela*, David Arsenio Landínez Téllez**, Jairo Roa-Rojas****

ABSTRACT

Parra Sua J. P., C. A. Sjogreen Blanco, J. E. Alfonso Orjuela, D. A. Landínez Téllez, J. Roa-Rojas: Morphological, structural and magnetic characterization of black sands of the Guajira – Colombia. Rev. Acad. Colomb. Cienc., 37 (1): 60-64, 2013. ISSN 0370-3908.

This article shows the morphological, structural and magnetic properties of the black sand on the surface soil obtained in the Guajira-Colombia. Morphological characterization of samples is performed by SEM. The compositional analysis of the compounds and elements was carried out through the XRF technique and by applying the Rietveld method to the X-ray diffraction data by quantifying the polycrystalline phases present in the simple such as ilmenite and magnetite. Magnetic characterization was performed by obtaining the hysteresis curve of magnetization as a function of applied fields at 300K temperature. Results evidence a ferromagnetic behavior of sample with magnetic parameters that permit to discuss the origin of magnetic character in the black sands. From heat treatments on air at different temperatures, the present magnetic phases are studied in order to determine the possibility obtaining of a single phase.

Keywords: Black sand, ferromagnetic, ilmenite, magnetite

RESUMEN

En este artículo se muestran las propiedades morfológicas, estructurales y magnéticas de la arena negra obtenidas sobre la superficie del suelo en la Guajira - Colombia. La caracterización morfológica de las muestras se lleva a cabo por SEM. El análisis de la composición de los compuestos y elementos se llevó a cabo a través de la técnica de XRF y mediante la aplicación del método de Rietveld a los datos de difracción de rayos X mediante la cuantificación de las fases policristalinas presentes en la muestra tales como ilmenita y magnetita. La caracterización magnética se realizó mediante la obtención de la curva de histéresis de la magnetización en función de los campos aplicados a 300K de temperatura. Resultados evidencian un comportamiento ferromagnético

* Grupo de Ciencia de Materiales y Superficies, Departamento de Física, Universidad Nacional de Colombia, Bogotá, Colombia

** Grupo de Física de Nuevos Materiales, Departamento de Física, Universidad Nacional de Colombia, Bogotá D.C., Colombia

de la muestra con parámetros magnéticos que permiten analizar el origen de carácter magnético en las arenas negras. Los tratamientos térmicos se realizaron en aire a diferentes temperaturas, donde se estudiaron las fases presentes con el fin de determinar la posibilidad de la obtención de una sola fase.

Palabras claves: Arena negra, ferromagnéticos, ilmenita, magnetita

1. Introduction

Many materials that are currently used are mined [1] and it is known that the chemical composition of these minerals depends on its location. Minerals such as magnetite and ilmenite are of great interest due to their crystal structures because they show the presence of iron and titanium, which are materials with a wide application in fields such as aeronautics, military industry and some applications in biomedicine. The hematite phase of iron oxide is used as a pigment in the manufacture of paints. Studies in sands such as the one conducted by Muta'álim and others which are magnetic sands found on beaches in Indonesia, show the presence of iron-based compounds and titanium as shown in this paper [2]. In this paper the chemical and morphological description of the black sands of La Guajira Colombia and results of the magnetic response are presented. Experimental data of x-ray diffraction are compared with the results obtained by fluorescence spectroscopy X-ray, which shows the presence of compounds based on iron, titanium, quartz, zircons and others. Images found by scanning electron microscopy show the morphology of minerals which are consistent with results of the fluorescence and diffraction characterization. Finally, it shows the ferromagnetic behavior of the sample at room temperature, given that the composition of the sample is mostly magnetite.

2. Experimental

Obtaining black sands samples used in this study were collected from the Mingueo beach in the municipality of Dibulla in the department of La Guajira in Colombia, 90km east of the Sierra Nevada de Santa Marta, in a territory which is part national park of Sierra Nevada de Santa Marta.

The measurements of X-ray diffraction (XRD) was performed on a sample diffractometer with rotating Bragg-Brentano (Philips X'pert-Pro), the XRD data are taken at 2θ between 10° to 90° using radiation CuKα with a wavelength of 1.54 Å and a detector RTMS (remote traffic microwave sensor). Refinements of the experimental data were performed through the GSAS and PowderCell 2.4 codes. From the X'Pert Highscore 2.0 semiquantitative concentrations of samples were determined.

Mineral samples were reduced in grain size with a fritsch ball mill at *400 rpm* for *3 min* obtaining a grain size of *300 μm*.

Figure 1. Map of Mingueo beach in municipality of Dibulla.

Morphologic analysis was carried out with a scanning electron microscope FEI Quanta *200 in* a vacuum environment *10* to *130 Pa*, due to variations in intensity it can be observed the analyzed surface topography, where the lighter areas correspond to the phases of higher atomic weight, useful a solid state detector. The fluorescence analysis was performed on a petro AXIOS PANalalytical brand equipment with a reduced grain size produced by a ball mill described above, it was taken *8 g* of the obtained powder, where this powder was combined with *0.8 g* of wax, after that it was placed in a *40 mm* diameter mold, and then it was press at *100 kN* for *20 s*, resulting in a pellet. The scanning was performed at *2θ* in a range *10°* to *150°* using Super Q Manager software. This technique allows us to find the elements present in the sample, and it should be noted that there may be elements of concentrations below *100 ppm* which the equipment cannot detect. For measuring the magnetic properties it was used the magnetic power measurement system MPMS quantum design. The magnetic moment was measured at room temperature, by using the hysteresis measurement through the application of magnetic fields from *-5000 Oe* up to *5000 Oe*; the frequency used was *40 Hz*, and the trial was conducted between *250 mV – 25 mV*.

3. Results and Discussion

X-ray fluorescence Analysis shows the existence of different phases present in the sample which can be seen in Table1.

The spectroscopic analysis of X-ray fluorescence indicates that the iron is the element with the highest proportion in the count made, following by the titanium and silicon. These results can be verified in Table 1 which shows that *Fe*, *Ti* and *Si* are elements found in higher proportion in the sample. These results are compared with the analysis of X-ray diffraction in

Table 1: Results of X-ray fluorescence in the sample of black sands from la Guajira

Name*	Symbol	Composition (%)
Sodium	Na	1.6
Magnesium	Mg	0.7
Aluminium	Al	1.9
Silica	Si	10.8
Phosphorus	P	0.2
Sulphur	S	0.3
Potasium	K	0.2
Calcium	Ca	1.2
Titanium	Ti	21
Chromium	Cr	<0.1
Manganese	Mn	1.6
Iron	Fe	56.7
Zinc	Zn	<0.1
Zirconium	Zr	2.5
Yttrium	Y	<0.1
Niobium	Nb	0.1
Cerium	Ce	0.1
Hafnium	Nf	0.2
Chlorine	Cl	0.9

* The "elements" present make oxides.

which verifies that the phases present and the percentages of each of them coincide in the two methods of analysis. Consequently, it can be stated that present content of the sample phases are magnetite, ilmenite, quartz and zircon. Figure 2, show the difractogram performed on the sample of black sands from La Guajira where the characteristic peaks of the phases present in the sample can be appreciated, which are identified as magnetite, ilmenite, quartz, zircon and others with lesser degree.

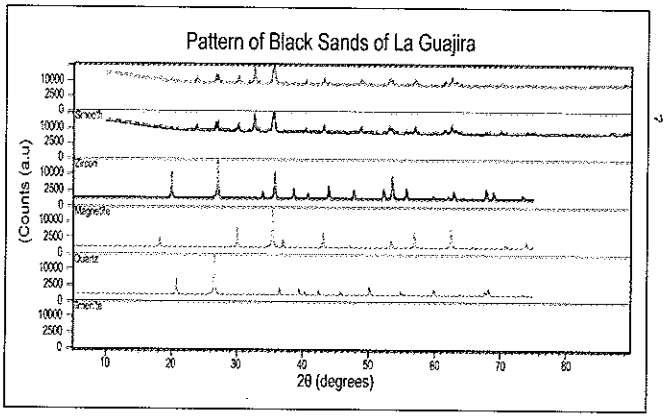

Figure 2. XRD pattern of black sands from Guajira.

The lattice parameters and crystal structures found for the compounds in the sample of black sand are compared with those reported by other authors and are consistent with the obtained by this work. Using the Rietveld refinement method the quantitatively phases of black sands samples were found. Results are consistent with the values in Table 1 and stoichiometry of the different phases which are around 37% magnetite, 42% ilmenite, 14% quartz and 7% zircon. After the sample was separated magnetically, it was heated at *650 °C*; it can be observed in the figure 3 the presence of hematite and titanium oxide phases.

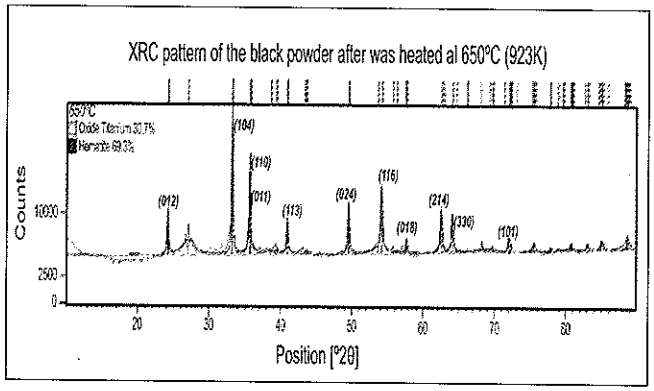

Figure 3. XRD pattern of the black powder after it was heated at 650 °C.

At the end of Table 2 it shows the found parameters of the new lattice of the crystalline phases where a comparison is made with results reported by other authors, and it is found a similarity in their parameters. The quantification of the sample indicates that 80% belongs to the hematite phase and 20% to the titanium oxide phase.

In Figure 4 it can be seen some maximized phases present in the sample such as quartz, magnetite and ilmenite. The grains have no crystalline forms due to erosion process.

Hysteresis curve shows a ferromagnetic behavior of the samples; this is because as noted above in the analysis of the x-ray diffraction phases is present a good amount of iron in their crystal structures as magnetite [5]. The hysteresis curve shows that Crystallites found in the black sands samples possess ferromagnetic behavior which can be attributed to the high concentration of magnetite in the material.

The magnetic parameters obtained were: *32.7 emu/g* saturation magnetization on *4.9 kOe*, *2.5 Oe* coercive field and *0.07458 emu/g* remnant magnetization.

Table 2: Lattice parameters of the phases present in the black sand of la Guajira.

Phase	Lattice Parameter (Å)	Ref.	Crystalline Structure
Magnetite (Fe_3O_4)	*a=8.3940*		Cubic
Ilmenite ($FeTiO_3$)	*a=5.09 c=14.093*	*a=5.088 c=14.093 [6]*	Hexagonal
Quartz (SiO_2)	*a=4.9148 c=5.4062*		Hexagonal
Zircon ($ZrSiO_4$)	*a=6.6042 c=5.9796*		Tetragonal
Hematite (Fe_2O_3)	*a=5.0355 c=13.7471*	*a=5.0355 c=13.7471 [7,8]*	Rhombic
Titanium Oxide (TiO_2)	*a=4.6530 c=2.9650*		Tetragonal

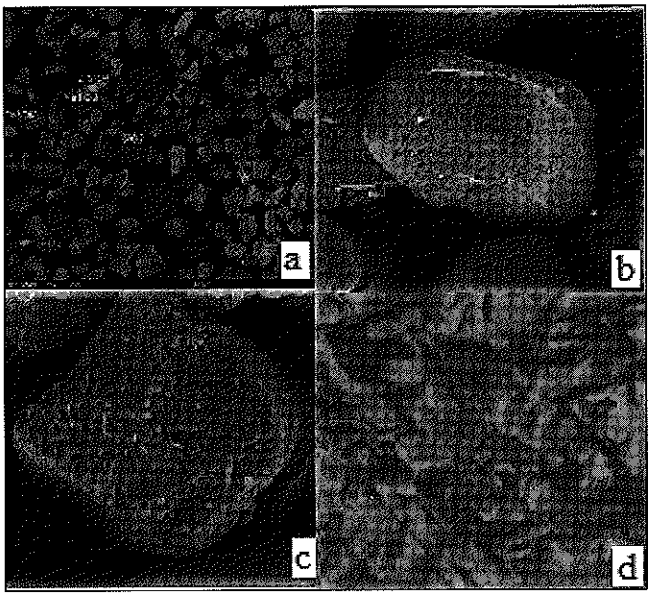

Figure 4. SEM image magnetic sands a) identification of the crystallites, b) and c) ilmenite grains d) magnetite grains

4. Conclusions

X-ray diffraction and X-ray fluorescence showed that the black sands from La Guajira have a high content of magnetite, ilmenite, quartz, and the presence of other elements

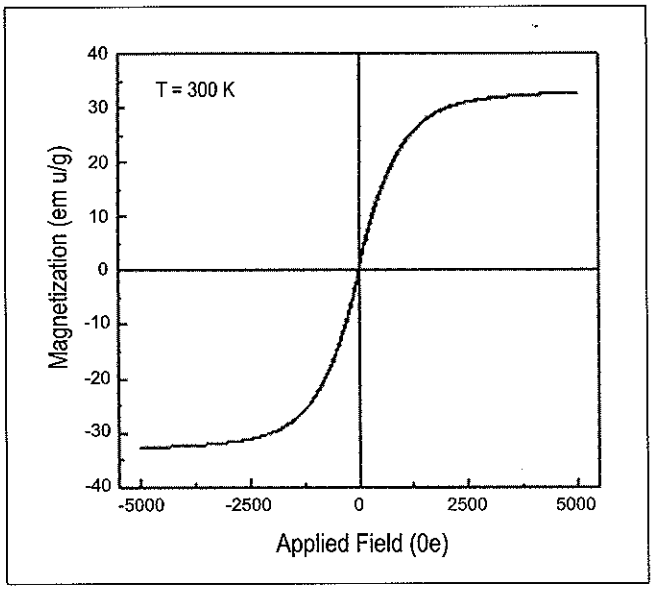

Figure 5. Magnetization as a function of applied field. Hysteresis curve shows the ferromagnetic behavior of the sample.

in low proportion such as zircons. The present phases were 42% of magnetite, 37% of ilmenite, about 10% of quartz, 3% of zircon, and the remaining 8% of the sample represent the presence of other components in lesser amount. Furthermore it can be seen that the heat treatment conducted in the magnetic phases evidenced a change of crystalline structure from magnetite and ilmenite to hematite and titanium oxide. The magnetization curve shows a ferromagnetic behavior due to the presence of minerals such as magnetite and ilmenite where magnetite phase being the largest contributor to this magnetic behavior.

Acknowledgements

Authors wish to thank ALPHA1 for providing the XRF equipment and ball mill. To Professor Helena Concha from Geology Department of National University of Colombia for his guidance in the field of minerals. This work was partially financed by DIB (Hermes Code 13893) and "El Patrimonio Autónomo

Fondo Nacional de Financiamiento para la Ciencia, la Tecnología y la Innovación Francisco José de Caldas" Contract RC No. 0850-2012".

References

[1] **M. Klepka, K. Lawniczak-Jablonska, M. Jablonski, A. Wolska, R. Minikayev, W. Paszkowicz, A. Przepiera, Z. Spolnik, R. Van Grieken,** (2005), Combined XRD, EPMA and X-ray absorption stu-

dy of mineral ilmenite used in pigments production. Journal of Alloys and Compounds. Volume 401, Issues 1–2, Pages 281–288.

[2] **M. Muta´alim**, (2009). Characterization of prereduced iron sand concentrate pellet with coal IRAM, International journal of science environment and technology, Volume 21, pp., 712.

[3] www.googlemaps.com.

[4] **A.A. Surour, A.A. El-Kammar, E.H. Arafa, H.M. Korany**, J. of Geochem. Explor. (2003), Dahab stream sediments, southeastern Sinai, Egypt: a potential source of gold, magnetite and zircón. Journal of Geochemical Exploration. Volume 77, Issue 1, Pages 25–43.

[5] **T. Taboada, A. Martínez Cortizas, C. García, E. Garcýa-Rodeja**, (2006), Particle-size fractionation of titanium and zirconium during weathering and pedogenesis of granitic rocks in NW Spain. Geoderma. Volume 131, Issues 1–2, Pages 218–236.

[6] **R. Luo, Li-qun**. (2012), Characterization and technology of fast reducing roasting for fine iron materials. J. Cent. South Univ. Volume 19, pp., 2272–2278.

[7] **M.C. Morris, et al., Natl. Bur. Stand**. (U.S.) Monograph 25, 15(1978) 34 (ICDD database Ref. 29-0733)

[8] **M.C. Morris, et al.**, Natl. Bur. Stand. (U.S.) Monograph 25, 18 (1981) 37 (ICDD database Ref. 33-0665).

PRODUCTION SYSTEM AND STRUCTURAL CHARACTERIZATION $CAMN_{1-x}TI_xO_3$ (WITH X = 0.0, 0.25, 0.5, 0.75 AND 1.0)

PRODUCCIÓN Y CARACTERIZACIÓN ESTRUCTURAL DEL SISTEMA $CAMN_{1-x}TI_xO_3$ (CON X=0.0, 0.25, 0.5, 0.75 Y 1.0)

José del Carmen Ríos Viasus* , Davian Martínez Buitrago*, Cesar Armando Ortiz, Aura Janeth Barón*, Carlos Arturo Parra Vargas***

ABSTRACT

Ríos Viasus J. del C., D. M Buitrago, C. A. Ortiz, A. J. Barón, C. A. Parra Vargas: Production system and structural characterization. CaMn1-xTixO3 (with x = 0.0, 0.25, 0.5, 0.75 and 1.0). Rev. Acad. Colomb. Cienc., 37 (1): 65-68, 2013. ISSN 0370-3908.

In this work, we report the production of new composite perovskite manganite system $CaMn_{1-x}Ti_xO_3$ with doping x = 0.25, 0.5 and 0.75, reaction sintering method solid state. Structural characterization was performed using the technique of X-ray Diffraction (XRD) and the Rietveld method, obtaining a tetragonal structure, with Pnma spatial group (# 62) (a=5.3586Å y a=5.2997Å; b=7.5041Å y b=7.5526Å; c=5.3182Å y c=5.3278Å). In this paper takes the discussion on possible structural changes with changes in the system titanium $CaMn_{1-x}Ti_xO_3$.

Key words: Manganites, perovskite, structural analysis.

RESUMEN

En éste trabajo se reporta la producción del nuevo sistema tipo perovskita compuesta manganita $CaMn_{1-x}Ti_xO_3$ con dopajes x= 0.25, 0.5 y 0.75, sinterizado por el método estándar de reacción de estado sólido. La caracterización estructural se realizó a través de la técnica de Difracción de Rayos X (DRX) y el método de Refinamiento Rietveld, obteniendo una estructura tetragonal, con grupo espacial Pnma (#62) (a=5.3586Å y a=5.2997Å; b=7.5041Å y b=7.5526Å; c=5.3182Å y c=5.3278Å). En este paper se realiza la discusión sobre los posibles cambios estructurales con la variación del titanio en el sistema $CaMn_{1-x}Ti_xO_3$.

Palabras clave: Manganitas, perovskita, análisis estructural.

* Grupo de Física de Materiales, Escuela de Física, Universidad Pedagógica y Tecnológica de Colombia, Tunja, Colombia. E-mail: chrios1@hotmail.com

** Grupo de Superfícies, Electroquímica y corrosión, Universidad Pedagógica y Tecnológica de Colombia, Tunja, Colombia.

I. Introduction

The manganites have been studied extensively in recent years, mainly due to the discovery advance property of colossal magneto resistance (CMR) and the discovery of high temperature superconductors (**Raveau *et al.,*** 1998; **Raveau *et al.,*** 2000). These also show extraordinary and varied transport properties (**Helmolt Von *et al.,*** 1993; **Kuwahara H. *et al.,*** 1998). Two types of behavior can be set to the manganites doped with holes, have CMR and electron-doped manganites showing CMR properties in a narrow range of composition and only for small cations, in this way substitution in Mn sites of these compounds doped generate great potential for inducing properties of the films **(Nagaev E. L. 2001).** As the metal insulator transition and CMR effects.

Recent studies (**Nagaev E. L.** 2001; **Raveau B *et al.,*** 2000). Show that partial substitution of pentavalent or hexavalent elements by Mn (IV) presenting induce electron doped double exchange phenomenon Mn^{3+} - O - Mn^{4+} (**Gil de Muro Izaskun *et al.,*** 2005) as it was shown for the system $CaMn_{1-x}Ln_xO_3$, besides that the manganite doped with electrons in the system $CaMn_{1-x}M_xO_{3-\delta}$ with M = Nb, Ta, W, Mo [2,8], almost semimetallic exhibit behavior over a wide range of composition below 30K and significant ferromagnetic interaction also demonstrated the existence of CMR at low temperatures in the range of 4-50K (**Ochoa Burgos R. *et al.,*** 2012; **Roa-Rojas *et al.,*** 2008). Thus, in the continuing search for understanding the inherent properties multiferroicidad and the discovery and production of new materials that exhibit this effect, generated the idea of producing the $CaMn_{1-x}Ti_xO_3$ new system, which has a complex perovskite structure $CaMn_{1-x}Ti_xO_3$. Initially system meets some of the requirements of the materials being multiferroics combining two simple perovskite dielectric $CaTiO_3$ magnetic $CaMnO_3$. This paper focuses primarily on the production and structural characterization $CaMn_{1-x}Ti_xO_3$ system by the Rietveld refinement technique (**Yung R. A.** 1993). In order to establish the structural characteristics of that system.

II. Experimental

The preparation process $CaMn_{1-x}Ti_xO_3$ samples (with x = 0.25, 0.5 and 0.75.) Was made by the standard method of solid state reaction (**Gil de Muro Izaskun *et al.,*** 2005) from the mixture of the precursor oxides of high purity titanium oxide TiO_2 (99.999%), manganese oxide MnO_2 (99.99%), calcium carbonate CaCO3 (**Raveau B. *et al.,*** 1998) (97.00%). These oxides were weighed in amounts calculated stoichometry, dried at a temperature of 120 ° C for 12 hours and macerated manually mixed in an agate mortar to obtain fine particles and to ensure a homogeneous mixture. These samples thus prepared were divided into two series preparing tablets with a diameter of 0.8cm and a thickness of 0.5 cm in a hydraulic press with pressure of 5 ton/cm^2 approximate which were subjected to two heat treatments calcined at a temperature of 900 °C for 36 hours and sintering at 1360 °C for 84 hours. Structural analysis was done by XRD technique using XPERT-PRO diffractometer PANalytical with λ = 1.54064 Å copper Kα line, step 2Theta: 0.001 Position with a Start position [° 2Th.] 20.0100 and End Position [° 2Th.] 79.9900. At diffractograms were asked to Rietveld software GSAS input crystallographic data were taken from references reported and these were adjusted PCW23 program, necessary for the software GSAS refinement. The experimental results presented correspond to the three values of doping respectively.

The figure 1. Displays the x-ray diffractogram theorists. Calculated at Spuds program and plotted on PCW theoretical modeled $CaMn_{1-x}Ti_xO_3$ system.

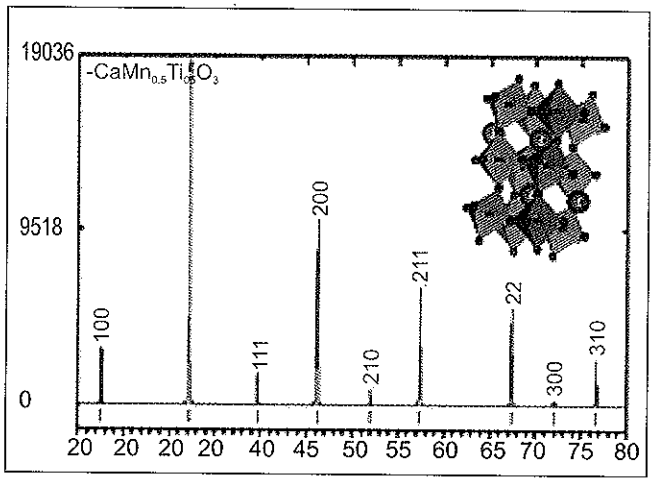

Figure 1. Theoretical Difragtograma of $Mn_{0.25}Ti_{0.75}O_3$.

III. Results and discussion

Figure 2 shows the experimental x-rays for the threedoped $CaMn_{1-x}Ti_xO_3$ system, clearly shows that the three belong to the same structural phase. Structural analysis of the samples was done using the Rietveld refinement technique (**Yung R. A.** 1993) through the GSAS program.

Comparing the diffraction patterns being theoretical and experimental adjustment necessary data manually until the best correlation between these using the PCW program, critical for the initiation process of refinement by Rietveld method. In Figure 3 are shown the data obtained by Rietveld refinement $CaMn_{1-x}Ti_xO_3$ system (with x = 0.75). The data marked with crosses represent the experimental result in continuous

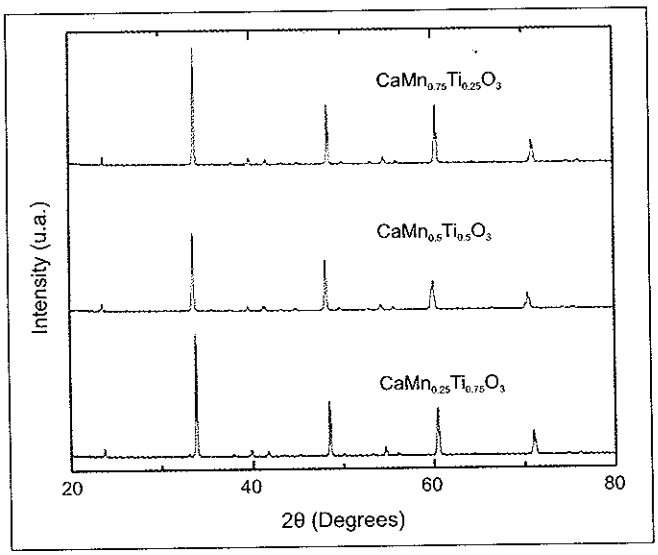

Figure 2. XRD diffractograms. Theoretical $CaMn_{1-x}Ti_xO_3$ system. For the three doped.

red line represents the theoretical diffractogram, green line and blue Background the difference between theoretical and experimental diffractograms. Also shown in Figure 4. Appropriate system-$CaMn_{1-x}Ti_xO_3$ (with x = 0.5) and Figures 5. $CaMn_{1-x}Ti_xO_3$ system (with x = 0.25.)

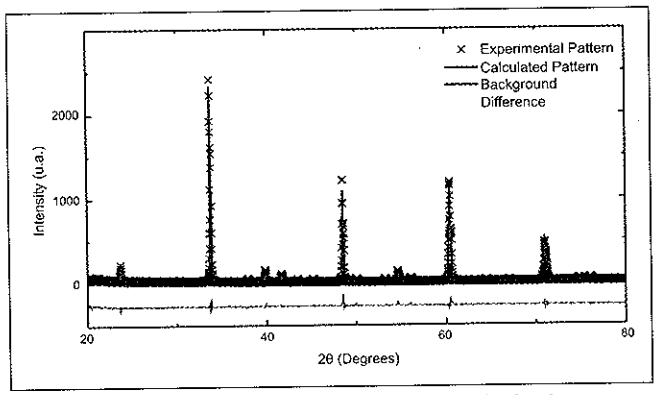

Figure 3. Rietveld refinement results obtained for the sample $CaMn_{0.25}Ti_{0.75}O_3$.

The refining process identified corresponding to a single phase$CaMn_{1-x}Ti_xO_3$ compound. Perovskite-type compound which crystallizes with orthorhombic structure with Pnma space group number 62.

In the Table 1, we identify the lattice parameters a, b, c structural angles α, β, γ; χ^2 R_{Bragg}, Rf^2, f.o factor and spatial positions x, y, z obtained by Rietveld refinement for the sample $CaMn_{0.25}Ti_{0.75}O_3$. In Figure 3, there is obtained quality refinement so that the calculated curve of peak intensities is set

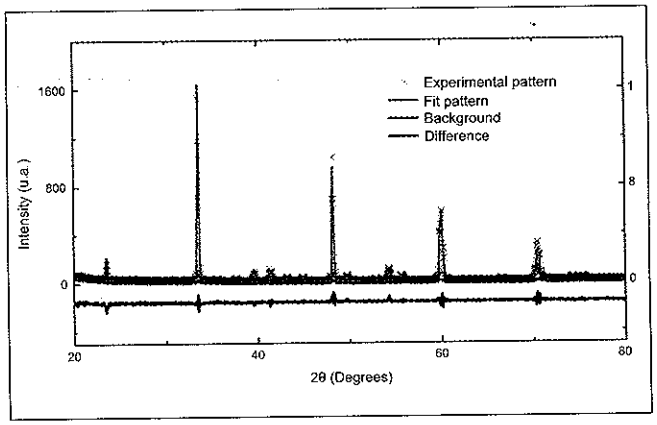

Figure 4. Rietveld refinement results obtained for the sample CaMn0.5Ti0.5O3.

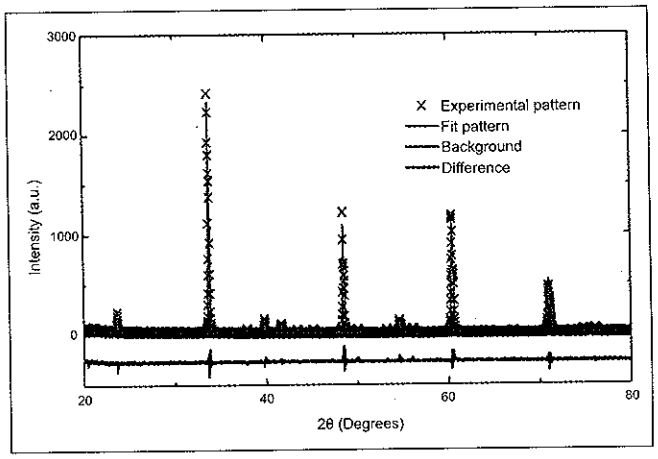

Figure 5. Rietveld refinement results obtained for the sample CaMn0.75Ti0.25O3

with good approximation to the observed intensities curve, obtained as a result of variance values: Rf^2= 12.72% and χ^2= 1.974 showing the reliability of the process, and it is observed that all the diffraction peaks correspond to a single phase of the compound and do not manifest secondary phases of impurities.

In the Table 2, we identify the lattice parameters a, b, c, structural angles α, β, γ; χ^2, R_{Bragg}, Rf^2, f.o factor and spatial positions x, y, z, obtained by Rietveld refinement for the sample $CaMn_{0.5}Ti_{0.5}O_3$. In Figure 4, like in figure 3 show the results of Rietveld refinement of variance values: Rf^2 = 14.79% and χ^2 = 1.435.

In the Table 3, we identify the network parameters a, b, c structural angles α, β, γ; χ^2, R_{Bragg}, Rf^2, f.o factor and spatial positions x, y, z, Rietveld structural refinement obtained for the sample $CaMn_{0.75}Ti_{0.25}O_3$. In Figure 5 in the same way as in Figures 3 and 4 shows the results of the Rietveld refine-

Table 1. Spatial positions and structural parameters obtained through the Rietveld refinement technique for the system $CaMn_{0.25}Ti_{0.75}O_3$

$CaMn_{0.25}Ti_{0.75}O_3$ Sample

	a = 5.3013 Å α = 90.00 χ^2= 1.974	b =7.5053 Å β = 90.00 R_{Bragg}=0 .1978	c = 5.3181 Å γ = 90.00 R_f^2 = 0.1272	
	X	**Y**	**Z**	**F.O.**
Ca	0.0155	0.2500	1.0010	1.000
Mn	0.0000	0.0000	0.5000	0.250
Ti	0.0000	0.0000	0.5000	0.750
O	0.4778	0.2500	0.0282	1.000
O	0.2998	0.6273	0.7096	1.000

Table 2. Spatial positions and structural parameters obtained through the Rietveld refinement technique for $CaMn_{0.5}Ti_{0.5}O_3$ system.

$CaMn_{0.5}Ti_{0.5}O_3$ Sample

	a = 5.3586 Å α = 90.00 χ^2 = 1.435	**b** = 7.5526 Å β =90.00 R_{Bragg}=0.1978	**c**=5.3278 Å γ =90.00 R_f^2=0.1479	
	X	**Y**	**Z**	**F. O.**
Ca	0.0269	0.2500	0.9886	1.006
Mn	0.0000	0.0000	0.5000	0.497
Ti	0.0000	0.0000	0.5000	0.497
O	0.4831	0.2500	0.0451	0.959
O	0.2895	0.0475	0.7081	1.029

Table 3. Spatial positions and structural parameters obtained through the Rietveld refinement technique for the system $CaMn_{0.75}Ti_{0.25}O_3$

$CaMn_{0.75}Ti_{0.25}O_3$ Sample

	a = 5.2997 Å α = 90.00 χ^2 = 1.622	b = 7.5041 Å β = 90.00 R_{Bragg} = 0.1978	c = 5.3167 Å γ = 90.00 R_f^2=0.1080	
	X	**Y**	**Z**	**F.O.**
Ca	0.0139	0.2500	1.0038	1.028
Mn	0.0000	0.0000	0.5000	0.726
Ti	0.0000	0.0000	0.5000	0.250
O	0.4767	0.2500	0.0215	0.971
O	0.3004	0.0635	0.7034	0.993

ment with values results in disagreement: Rf^2 = 10.94% and χ^2 = 1.620 again showing the reliability of the process.

IV. Conclusions

We produced the Compound the $CaMn1_{-x}Ti_xO_3$ (with x = 0.25, 0.5 and 0.75) system. Through the technique of solid state reaction. This material has a double perovskite structure which corresponds to the number 62 group Pnma.

Rietveld refinement analysis established that $CaMn_{1-x}Ti_xO_3$ system presents a single phase orthorhombic structure with lattice parameters between a = 5.3586Å and a = 5.2997Å, b = 7.5041Å and b = 7.5526Å and c = 5.3278Å and c = 5.3182Å for stoichiometries (with x = 0.25, 0.5 and 0.75) respectively.

In the graphs shows refinement quality obtained so that the curves calculated from the peak intensities adjusted with good approximation to the observed intensities curve, showing that the reliability of the process and the presence of a single phase of the compound and confirming the absence of secondary phase impurities.

V. References

Gil de Muro Izaskun, Insausti Maite, Lezama Luis, Rojo Teòfilo, Morphological and magnetic study of $CaMnO_{3-x}$ oxides obtained from different routes, journal of Solid State Chemistry **178** (2005): 928-936.

Helmolt Von, Wecker R., Holzapfel J., Schultz B., L. and Samwer, K. Giant negative magnetoresistance in perovskita-like La2/3Ba1/3MnOx ferromagnetic film, Phys. Rev. Lett. **71**, (1993): 2331-2336.

Kuwahara H. and **Tokura Y.**, "Colossal Magnetoresistance, Charge Ordering and Related Properties of Manganese Oxides", C.N.R. (1998): 217-216,

Kupriyanov M.F., V. S. Filip'ev, Kristallografiya (1963): 356-370.

Nagaev E. L., Colossal-Magnetoresistance materials: manganites and conventional ferromagnetic semiconductors, Physics Reports, **346**, (2001): 387-392.

Ochoa Burgos R., Martínez B. D., Parra Vargas C. A., Landinez Téllez D. A., Vera López E., Sarmiento Santos A., Roa-Rojas J., Magnetic and ferroelectric response of Ca_2TiMnO_6 manganite-like perovskite Revista Mexicana de Física S **58** (2012): 44–46.

Raveau B., Maignan A., Martin C., Hervieu M., Colossal Magnetorresistance manganite perosvkites: Relation between crystal chemistry and propertries. Chem. Mater. **10** (1998): 2641-2644.

Raveau B., Zhao Y. M., Martin C., Hervieu M. and Maignan A. Mn-Site Doped CAMnO3: Creation of the CMR Effect Journal of Solid State Chemistry **149**, (2000): 203-207.

Roa-Rojas, Salazar J., Llamosa C., Leon-Vanegas D., Landinez, Pereur D., Dias, F. T. Vieir, V. N., Magnetoelectric Response of new Sr2TiMnO6 manganite-like material, Journal of Magnetism and Magnetic Materials **320** (2008): 104-106.

Skakle J.M. S. and **A. R.** Superconducting $La_{1.5-x}Ba_{1.5+x-y}Ca_yCu_3O_z$ solid solutions I. Phase diagram, cation stoichiometry and T_c data. West, Physica C, vol. **220**, (1994):187-194.

Valldor Martin, Esmaeilzadeh Saeid, Andersso Magnus, Morawski Andrzej. Preparation and characterization of the double perovskita Sr_2TaMnO_6. Journal of magnetism and magnetic materials **299** (2006): 161-169

Yung R. A., the Rietveld Method, (Oxford University Press. (1993).

TECHNOLOGICAL, ENVIRONMENTAL AND ECONOMIC IMPACT, OF THE MINERAL MATTER PRESENTED IN COAL

IMPACTO TECNOLÓGICO, AMBIENTAL Y ECONÓMICO DE LA MATERIA MINERAL PRESENTE EN EL CARBÓN

F. Reyes Caballero[*], C. A. Parra Vargas[**], S. A. Martínez Ovalle[*].

ABSTRACT

Reyes Caballero F., C. A. Parra Vargas, S. A. Martínez Ovalle: Technological, environmental and economic impact, of the mineral matter presented in coal. Rev. Acad. Colomb. Cienc., 37 (1): 69-74, 2013. ISSN 0370-3908.

The analysis of the mineral matter contributes meaningfully to define the quality of coal. In this work we present the results of identification and quantification of mineral phases presented in samples of natural coal, and coal fractions beneficiated with concentration fractions of mineral matter, obtained by different separation methods using Rietveld-based X-ray diffraction (Rietveld-based XRD), ^{57}Fe transmission Mössbauer spectroscopy (MS) and scanning electron microscopy with energy dispersive X-Ray (SEM_EDX) analysis, which allows to identify the potential for removal of minerals. Furthermore, it is possible to explore the relationship between the ash obtained, the melting point, the calorific value and the relative proportions of the individual minerals in the samples studied. Similarly, using the information obtained, we evaluate the technological, environmental and economic impacts associated with mineral matter.

Key words: Coal quality, Mineral identification and quantification.

RESUMEN

El análisis de la materia mineral contribuye significativamente a definir la calidad del carbón. El propósito del artículo es presentar resultados de identificación y cuantificación, de las fases minerales presentes en el carbón y fracciones de carbón obtenidas por diferentes métodos de separación, usando Análisis Rietveld de patrones de difracción de rayos X, espectroscopia Mössbauer de transmisión 57Fe y microscopia electrónica de barrido con análisis de energía dispersiva de rayos X. Además, fue identificado el potencial de remoción de minerales, y fue explorada las relaciones entre la ceniza obtenida, el valor calorífico y las proporciones relativas de los minerales

[*] Grupo de Física Nuclear Aplicada y Simulación, Universidad Pedagógica y Tecnológica de Colombia, Tunja, Colombia.

[*] Grupo de Física de Materiales, Universidad Pedagógica y Tecnológica de Colombia, Tunja, Colombia.

individuales en las muestras estudiadas. Usando la información obtenida, se evalúan los impactos tecnológicos, ambientales y económicos asociados con la materia mineral.

Palabras clave: Calidad del carbón, Identificación y cuantificación de la materia mineral.

1. Introduction

Coal is the main and the most abundant in terms of reserves and geological resources of sedimentary fossil solid fuels: coal (<50 wt. % Ash), organic shales (50-90 wt. % Ash) and peat (**Alpern and Lemos de Sousa**, 2002). Coal is mostly used fuel for generating electricity in the world and current estimates indicate that 41% of global electricity is generated from its use (**WCA**. 2013). Several clean technologies (CCTs: Clean Coal Technologies) for the extraction, preparation and use of coal more efficient and environmentally acceptable are in used. Colombia has one of the most important reserves and resources in terms of quantity and variety of coal qualities with respect to Central and South America, from annually produce 5 to 10 Mt in the decade 1980-85 Mt in 2012 (Mt = Million tons).

Coal is a sedimentary rock, organic in nature, porous, complex, heterogeneous and stratified, formed from the fossilized remains of plants with inorganic elements incorporated. Inorganic elements are usually incorporated into the coal referred to as the "mineral matter," and contains three types of components: fluid matter (moisture and gas-liquid inclusions) through the pores of the coal, such as dissolved salts and other inorganic substances; elements inorganic associated with the organic compounds of the coal maceral (metal-organic complexes) and discrete crystalline inorganic particles (in the form of crystals, granules and aggregates) or non-crystalline (amorphous), representing true mineral components (**Tascón and Vassilev**, 2000).

Coal quality is defined as the coal properties and characteristics that affect its use (**Finkelman, 1995; Finkelman and Pierce**, 2002). Particularly, the information on the relative amount of the mineral phases, size, shape and composition of the minerals, the knowledge of the concentration and distribution of the elements between the organic and inorganic components, and washability potential or removal of an item during the benefit, contribute significantly to defining the quality of coal, due to: 1) Its influence on technological performance. In combustion processes the mineral matter is a source of unwanted agglomeration, abrasion, corrosion, inert material processing, tack, and pollution by gaseous emissions, liquid and solid, of volatile ashes, acid or alkaline solutions, toxic elements and potentially toxic compounds (**Clemens *et al.***, 2000; **Vassilev *et al.***, 2001). 2) Its environmental impact and human health. Most of the trace elements presented in natural coals are associated with mineral matter. The sulfides and sulfates contain various heavy metals (such as Pb, As and Ag) and its high sulfur content are a major source of environmental damage and human health, when coal is burned without previous cleaning procedures (**Finkelman and Gross**, 1999).

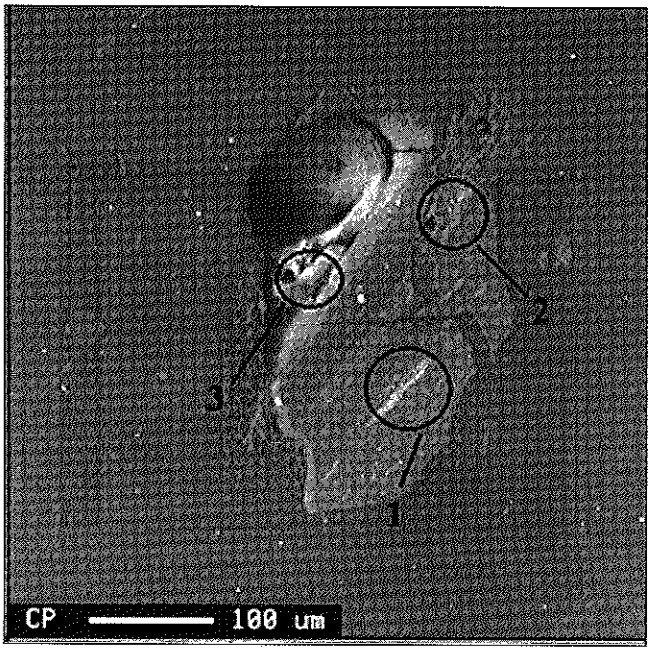

Figure 1. Electron micrograph of a fraction of beneficiated coal.

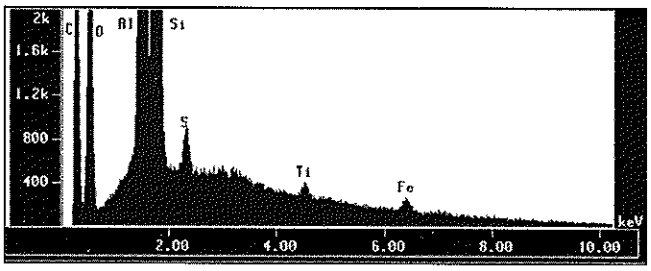

Figure 2. Analysis of X-ray energy dispersive.

3) Political and economic significance. Consumers, who currently define trading conditions, require coals meet strict specifications. 4) The use of residues of its benefit and processing. Globally, a fairly large number of projects are directed to find uses and recovery processes of waste byproducts of profit and coal processing (**ACAA**, 2013). 5) Its geoche-

mical significance. Mineral matter provides important information on the conditions of sedimentation and geologic history of the sequences containing the robes of a coal mine (**Ward**, 2002).

The purpose of our work is basically to apply analysis Rietveld of X-ray patterns diffraction,^{57}Fe Mossbauer spectroscopy of transmission and scanning electron microscopy with energy dispersive analysis of X-rays, to identify and quantify the mineral matter presented in Colombian coals. In this paper it is reported the identification of the potential for removal of minerals. Furthermore, it is examined the relationship between the calorific value and relative proportions of individual minerals. Similarly, using the information obtained are evaluated technological, environmental and economic impacts associated with mineral matter.

2. Experimental

In the study we have analyzed representative samples, air-dried and homogenized, from original material taken from Mine head with different ash contents of mines from Boyacá, Cundinamarca, Valle and Cauca. Different subsets have been subjected to various and different removal processes of mineral matter (physical: for example, floating, separation hidrociclónica and gamma irradiation separation, chemicals: treatment with dilute nitric acid and hot (**Reyes Caballero *et al.***, 2002; **Reyes Caballero and Martínez Ovalle**, 2013).

All samples were reduced to a particle size of 250 μm (No. 60 mesh), for analyzes according to ASTM standards (ash determinations, total sulfur, calorific value, etc.). (**ASTM**, 1991).

Partial information about mineral morphology, particle size and chemical composition was obtained by electron microscopy analysis of sample and microanalysis energy dispersive fluorescence using SEM/EDX JEOL 8900R.

For the analysis by Mossbauer spectroscopy and X-ray diffraction powder, subsamples were reduced to a particle size < 74 μm (N° 270 mesh).

It was prepared Mössbauer absorber by sandwich of powders of the samples (~ 100 mg) between two paper disks in circular specimen (12 mm diameter) in order to maintain constant the thinness of the absorber. Mössbauer spectra were taken at room temperature using a conventional spectrometer in transmission mode with a constant acceleration, with a source of ^{57}Co/Rh and calibration with respect to metallic iron. All spectra were fitted using the programs VARFIT y MOSSFIT. The identification of mineral phases presented, was made by comparing the Mössbauer parameters values obtained with values reported in the literature (**Stevens *et al.***, 1998; **Gracia *et al.***, 1999).

Standard specimen were prepared with a homogeneous mixture of natural coal dust or coal fractions (~ 50 mg) with ~ 10 mg of powder of high purity Fe (99.99%) used as internal standard for the radiation diffraction analysis with Cu -Ka on a Rigaku diffractometer in Bragg-Brentano geometry, 2θ-θ, with a scan speed of 0.05 ° 2θ / 5 so 0.05 ° 2θ/25 s, in the range of 4 ° to 140 ° in 2θ. The mineral phase identification was performed by search-match method using a personal computer with the help of PDF-2 Database and the software Perfil (**Reyes Caballero**, 2005). A software had to be developed to remove very high noise (background) presented in the diffraction profile before of the refinement procedure by Rietveld (**Reyes Caballero**, 2005). The Rietveld refinements were performed using the software DBWS-9807 y FullProf-2001

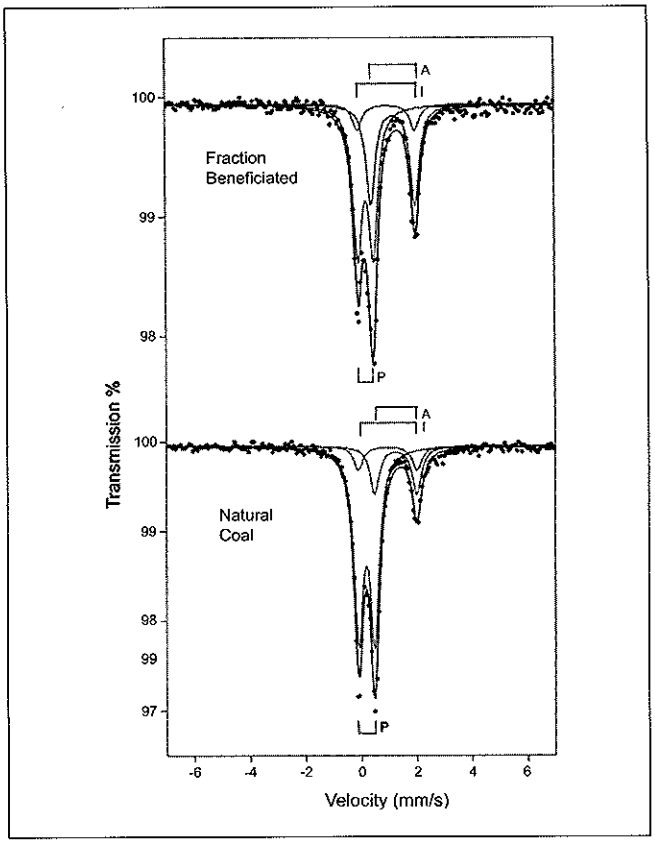

Figure 3. Mössbauer spectra of representative samples of beneficiated coal fraction (top) and natural charcoal (below), P: Pirita, A: Ankerita, I: Ilita.

3. Results and discussion

Quantification methods of mineral matter coal were initially indirect, it means, by calculating the ash content using various techniques, for example, **ATSM,** (2007):

$$MM=1.1CZ + 0.1AT,$$

Where CZ and AT are the values of ash and total sulfur, respectively. Today, there is the possibility of using modern methods of the mineral matter coal quantification, using electron microprobe, Mossbauer spectroscopy, analysis based on Rietveld patterns of X-ray diffraction. In Figure 1 it is showed an electron micrograph of a representative sample of a fraction of beneficiated coal. At points 1, 2 and 3 were identified clusters of pyrite grains. Figure 2 shows typical results obtained with the analysis of X-ray energy dispersive.

Table 1. Mössbauer parameters of the phases of Fe identified.

Sample	IS ±0.01 $mm \cdot s^{-1}$	QS ±0.01 $mm \cdot s^{-1}$	RA ±1 %	Phase
Yolanda	0.29	0.57	72	Pirita
Natural	1.35	1.52	20	Ankerita
Coal	1.02	2.03	8	Ilita
Yolanda	0.29	0.56	53	Pirita
Benef.	1.28	1.59	37	Ankerita
Coal	1.04	2.06	10	Ilita

Among the most important properties affecting the washability of minerals and / or elements are its modes of occurrence and their textural relationships. Elements associated with mineral phases offer the potential for removal by physical washing procedures coal. Elements associated primarily with the organic constituents will not be effectively reduced by the physical washing of the coal; on the contrary, they can be enriched in the washing of coal. Figure 3 compares the Mössbauer spectra of representative samples of beneficiated coal fraction (top) and natural coal (bottom). The identified phases correspond to Pirita, Ankerita e Ilita.. Mössbauer parameters of the phases Fe identified in the samples studied are presented in Table 1.

The spectra measured in this work allow define relative distributions of minerals and Fe concentration in the different products of the separation processes. The relative intensity of resonance Hp, peak height of Figure 3, gives the relative distribution of the phases of Fe in each sample. Relative spectral area (RA %) is considered proportional to the concentration of Fe in the sample, given the experimental conditions keeping constant spectrometer geometry and thickness of the sample. Therefore, changes in the value of the spectral area from sample to sample correspond to changes in the concentration of Fe. Mössbauer results show a Pirita removal of approximately 26%, while, reflect an inherent nature of mineral matter for the phases Ankerita and Ilita.

Figure 4 shows the Rietveld Refinement for the full pattern of X- ray difraction corresponding to a natural coal sample superimposed on the diffraction pattern of Fe, the latter used as internal standard. The mineral phases identified were Caolinita (K), Yeso (G), Dolomita (D), Calcita (C), Cuarzo (Q) y Pirita (P). The "hump" observed in X-ray diffraction profile for the region between 10° and 40°, is a characteristic pattern of X-ray diffraction corresponding to rock samples rich in organic matter such as coal. This "organic hump" is proportional to the content of organic matter in the sample (**Mandile and Hutton**, 1995).

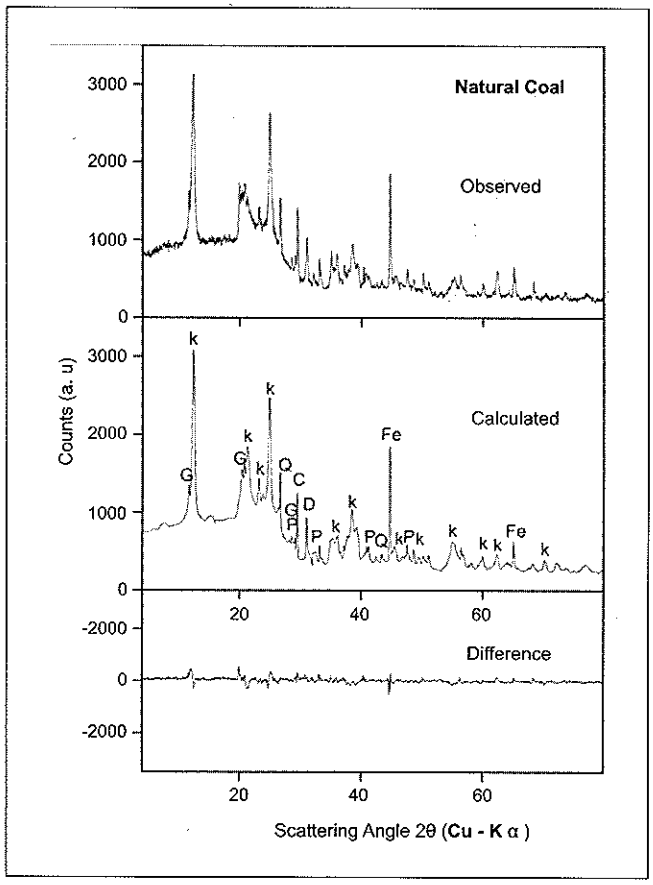

Figure 4. Rietveld Refinement of X-ray diffraction Pattern, of a natural mixture of carbon powder of Fe from high purity. K: Caolinite, G: Yeso, D: Dolomita, C: Calcita, Q: Cuarzo, P: Pirita.

The amount of ash and total sulfur determined by ASTM methods to natural coal were 25.1% and 2.2%, respectively. The concentrations of the mineral phases identified in natural coal, calculated of the Rietveld Refinement results for the full pattern of X-ray diffraction, are reported in Table 2.

Table 2. Refinement Rietveld results for the overall pattern of X-ray diffraction of a sample of natural carbon.

Phase	Formula	Regist (PDF-ICSD)	wt. %
Kaolinita	H4AI2 O9 Si2	PDF 14-164 ICSD 63192	24.3
Gypsum	H4 Ca O6 S	PDF 33-311 ICSD 2057	3.1
Dolomita	C2 Ca Mg O6	PDF 36-426 ICSD 10404	1.8
Calcita	C Ca O3	PDF 5-586 ICSD 16710	1.7
Quartz	O2 Si	PDF 46-1045 ICSD 63532	1.5
Pirita	Fe S2	PDF 42-1340 ICSD 43716	0.7
Total proportion crystalline mineral material			33.1

In Figure 5 are presented the calculated proportions of crystalline mineral matter and crystalline mineral phases for natural coal (Figure 5b) and beneficiated coal fractions (Figures 5a and 5d), and fractions of mineral matter concentration (Figure 5c and 5e). The results were obtained from the quantitative analysis based on Rietveld Refinement to the complete pattern of X-ray diffraction of the respective samples. The results show that the crystalline mineral matter represents a very important percentage of 33.1% of the total composition of natural coal. Mineral phases Caolinita y Cuarzo, are presented as foreign mineral matter in proportions of 24.3% and 1.5%, respectively. Carbonates Calcita and Dolomita are presented in the form of mineral matter inherent in proportions of 1.7% and 1.8%, respectively. Pirita and Yeso minerals are presented both as mineral matter and mineral matter odd inherent in proportions of 0.7% and 3.1%, respectively.

The mineral distribution between mineral odd matter and mineral matter inherent is associated with the amount of mineral matter that can be removed, so it is important to calculate the potential impact that can have on the cleaning processes on environmental quality, economic and technological of analyzed coal. The results show a 22% reduction in total sulfur content due to the first inorganic separation process (Figure 5b and 5a). Pyritic sulfur removal is 71%, while it is evidenced the mineral inherent matter character of the Yeso phase due to an increase of 9.5% in the pyritic sulfur content, assuming that the organic sulfur content was unchanged.

The heating value is the heat generated during the combustion of coal. In Figure 5 are presented the comparisons

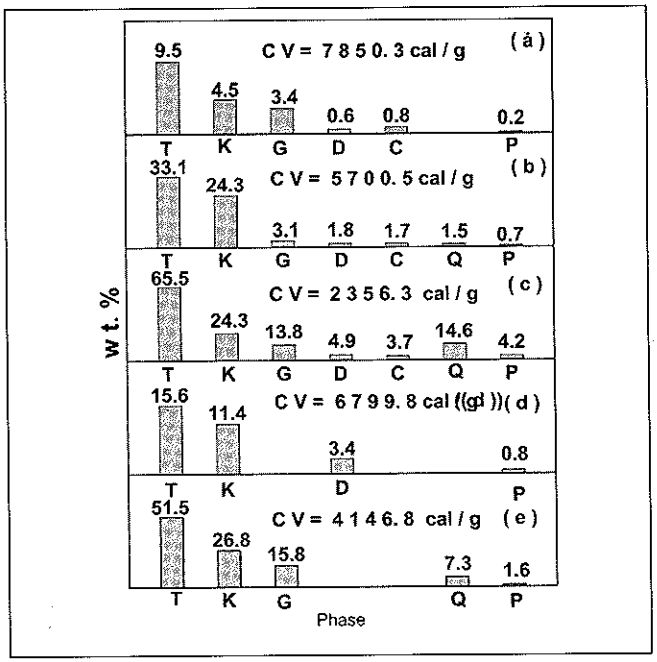

Figure 5. Calculation of ratios of total crystalline mineral matter of crystalline mineral phases presented for natural coal (b), beneficiated coal fractions (a) and (d), and fractions of coal mineral matter concentration (c) and (e). T: Total, K: Caolinita, G: Yeso, D: Dolomita, C: Calcita, Q: Cuarzo, P: Pirita.

between experimental measurements of calorific value (CV en $cal \cdot g^{-1}$ and the content (wt. %) of the mineral phases for representative samples of natural coal, and beneficiated coal fractions and fractions of coal mineral matter concentration. It is interesting to notice, a decrease in the total of crystalline mineral matter of 38%, between the natural coal and the beneficiated coal fraction, leading to an increased calorific value of 71%. In coal combustion, product of the transformation during heating, Pyrite phase has a thermal effect of exothermic nature with a value of +2193 $cal \cdot g^{-1}$, while the other phases have thermal effects of endothermic phase, with the largest value associated with Calcite phase - 437 $cal \cdot g^{-1}$.

4. Conclusions

There are meaningful technological, environmental and economic impacts due to the content of mineral matter in the coals.

From the experience gained, it is stated that there is no universal method that provides a complete mineralogical description for coals. Each technique, X-ray diffraction, Mössbauer spectroscopy, electron microprobe, etc, has advantages and limitations.

In the combustion of coal, Pirita has an exothermic nature effect, while the other mineral phases have endothermic effects.

5. References

ACAA, 2013. www.acaa-usa.org.

Alpern, B., Lemos de Sousa, M. J., 2002. Documented international enquiry on solid sedimentary fossil fuels; coal: definitions, classifications, reserves-resources, and energy potential. Int. J. Coal Geol., **50**, 3 - 41.

ASTM, 2007 ASTM D1506-99. Standard Test Methods for Carbon Black - Ash Content.

Clemens, A. H., Deely, J. M., Gong D., Moore T. A., Shearer J. C., 2000. Partitioning behaviour of some toxic trace elements during coal combustion – the influence of events occurring during the deposition stage. Fuel **79**, 1781 – 1784.

Finkelman, R. B., 1995. The Need for Enhanced Coal Quality Databases. Eight International Conference on Coal Science, Volume I, Oviedo, Spain. Elsevier Science, 75 – 78.

Finkelman, R. B., Gross, P. M. K., 1999. The Types of Data Needed for Assessing the Environmental and Human Health Impacts of Coal. Int. J. Coal Geol., **40**, 91-101.

Finkelman, R. B., Pierce, B. S., 2002. Coal Quality: Global Priorities. Proc. 27th International Technical Conference on Coal Utilization & Fuel Systems, Clearwater, Florida, USA, Coal Technology Association, Gaithersburg, Volume II, 667-668.

Gracia, M., Marco J. F., Gancedo J. R., 1999. Uses and perspectives of Mössbauer spectroscopic studies of iron minerals in coal. Hyperf. Int., **122**, 97-114.

Mandile, A. J., Hutton A. C., 1995. Quantitative X-ray diffraction analysis of mineral and organic phases in organic-rich rocks. Int. J. Coal Geol., **28**, 51-69.

Reyes Caballero, F., Pérez Alcázar, G. A., Barraza, J. M., Bohórquez, A., Tabares, J. A., 2003. Quantification of Pyritic Sulfur of the Colombian Coal by Mössbauer spectroscopy. Hyperf. Int., **148/149,** 31-38.

Reyes Caballero, F., 2005. Tesis Doctoral. Universidad del Valle, Cali-Colombia.

Reyes Caballero, F., Martínez Ovalle S. A., 2013. Mössbauer study of the inorganic sulfur removal from coals. Hyperf. Int., DOI 10.1007/s10751-013-0874-x.

Stevens, J. G., Khasanov, A. M., Miller, J. W., Pollak, H., Li, Z., 1998. Mössbauer Mineral Handbook. Baltimore Press, North Carolina, USA.

Tascón, J. M. D., Vassilev, S. V., 2000. La materia mineral del carbón: métodos de caracterización. Memorias V Congreso Nacional de Ciencia y Tecnología del carbón, Valledupar, Colombia, 19 – 23.

Vassilev, S. V., Eskenazy, G. M., Vassileva, C. G., 2001. Behaviour of elements and minerals during preparation and combustion of the Pernik coal, Bulgaria. Fuel Proc. Tech., **72**, 103 – 129.

Ward, C. R., 2002. Analysis and significance of mineral matter in coal seams. Int. J. Coal Geol., **50**, 135-168.

WCA, 2013. www.worldcoal.org.

REMOVAL OF PYRITE IN COLOMBIAN COALS BY USING GAMMA RADIATION

REMOCIÓN DE PIRITA EN CARBONES COLOMBIANOS USANDO RADIACIÓN GAMMA

J. A. Mejía[*], F. Reyes Caballero[**], C. A. Palacio[*], E. De Grave[***], H. Olaya Dávila[**], S. A. Martínez Ovalle[**]

ABSTRACT

Mejía J. A., F. Reyes Caballero, C. A. Palacio, E. De Grave, H. Olaya Dávila, S. A. Martínez Ovalle: Removal of pyrite in colombian coals by using gamma radiation. Rev. Acad. Colomb. Cienc., 37 (1): 75-78, 2013. ISSN 0370-3908.

In this contribution the results of a study by Mössbauer spectroscopy of the gamma-irradiation effect on the pyrite phase present in two Colombian coals are reported. The coals were exposed to different gamma-irradiation doses using a ^{60}Co source. It is known that the removal of sulfur from coal is necessary before using it as an energy source. This requirement results from the various environmental issues that sulfur-bearing species cause upon burning.

Key words: Pyrite, coals, gamma radiation.

RESUMEN

En esta contribución se reportan los resultados de un estudio Mössbauer acerca del efecto de la radiación gamma sobre la pirita que está presente en dos carbones colombianos. Los carbones fueron expuestos a diferentes dosis de radiación gamma proveniente de una fuente de ^{60}Co. Se sabe que es necesaria la remoción del sulfuro del carbón para ser usado como fuente de energía. Este requerimiento viene de los diferentes problemas ambientales que causan los componentes que contienen sulfuro cuando son sometidos a altas temperaturas..

Palabras clave: Pirita, carbones, radiación gamma.

[*] Universidad Antonio Nariño-sede Tunja, Tunja, Colombia. E-mail: juliethmejia@uan.edu.co

[**] Universidad Pedagógica y Tecnológica de Colombia, Tunja, Colombia.

[***] Ghent University, Ghent, Belgium

1. Introduction

Sulfur is present in coals in different forms, which are either elemental, organic or inorganic. In the case of the elemental sulfur S, it is present only occasionally in trace amounts. In the case of the organic sulfur, it is complicated to remove it from the coal by physical methods because it is chemically bound to the carbon matrix. Finally, in the inorganic case, S can be found as sulfide or as sulfate. In the first situation sulfur forms pyrite (FeS_2) as the most common component after it combines with iron in different ways. In the second situation, various iron sulfates e.g., Rozenite ($FeSO_4 \cdot 4H_2O$), ferrous sulfate ($FeSO_4$), Jarosite ($XFe_3(SO_4)_2(OH)_6$, etc. can be found,, or S can also be found as calcium sulfate.

When studying coal materials, the ^{57}Fe Mössbauer spectroscopy is a tool which is broadly applied. It is a non-destructive technique, with a high sensitivity, that gives information of the spectral parameters that are involved with the chemical state of the iron (Fe) and to its local chemical environment. By itself, the technique is very convenient for studying materials that contain combinations of iron compounds. However, in the Mössbauer spectra (MS) the presence of different Fe minerals in the coal samples strongly overlap, which makes the fitting very complicated. Also, the particle size, crystallinity, and substitution of certain particular phase may affect the hyperfine parameters of that individual Fe phase. Hence, when the MS are fitted, these aspects should be taken into account. These limitations can be handled by collecting MS at different (low) temperatures.

The removal of iron-sulfur minerals from coals prior to their combustion is necessary because these minerals cause sulfur oxides SOx (i.e., SO_2, SO_3) to be released and these are associated with environmental and health problems. In addition, the relative amount of pyrite usually influences the formation of agglomeration, corrosion, abrasion, tackiness. In preliminary works, methods used to remove Fe-S minerals have been examined. One method consists of a treatment with hot nitric acid, whilst two other physical methods use flotation and hydrocyclone separation (**Reyes & Martinez** 2013). Some studies concerning desulfurization of Indian and Egyptian coals using gamma irradiation have been reported (**Ram *et al.*** 1997, **Tripathi *et al.*** 2011, **Ahmed *et al.*** 2011).

In this work, the effect of gamma irradiation on the pyrite phase present in two Colombian coals is studied by means of Mössbauer spectroscopy.

2. Experimental Procedure

Coal samples were obtained from the mines Guachinte (Valle state) and Las Casitas (El Zalitre Zone, Boyacá state). The chemical analyses and Mössbauer results at room temperature of the samples were published elsewhere (**Reyes *et al*** 2003, ***Reyes & Martinez*** 2013).

20 g of the coal samples were placed at a distance of 40 cm from a ^{60}Co source which is part of a Theratron 780, Model C146. At the time of the irradiation, the equipment presented a reference rate of 118.48 cGy min^{-1} at 80 cm distance from the source. This equipment is located at the clinic for cancer of the city of Tunja (Boyacá). Subsamples of the two coals, approx. 1000 mg, were extracted after being irradiated with 284 Gy; and a second set of approx. 1000 mg was taken out after receiving 1800 Gy. The samples were named GUAX (Guachinte mine) and CASX (Las casitas mine), X being the radiation dose.

Mössbauer spectra (MS) in transmission mode were obtained from the samples at ~90 K, using a conventional spectrometer with constant acceleration drive and with a source of $^{57}Co/Rh$. The velocity scale was regularly calibrated by acquiring a spectrum of standard α-Fe_2O_3. DIST3E program was used for the analysis of the MS, which is based on hyperfine parameter distributions (**Vandenberghe *et al.*** 1994). The mineral phase identification was made by comparing the adjusted Mossbauer parameter values with the values reported in the literature for coals and also for pure compounds (**Huffman & Huggins** 1978, **Gracia et al.** 1999).

Table 1. Mössbauer results of the samples measured at 90 K. The quadrupole shifts ($2\varepsilon_Q$), quadrupole splittings (ΔE_Q) and isomer shifts (δ) are given in mm/s, the hyperfine fields (H_M) are in kOe and the areas (S) are given in %.

Sample	Phase	H_M	$2\varepsilon_Q/\Delta E_Q$	δ*	S
GUA284	Goethite	482.5	-0.25	0.47	32
	Pyrite		0.62	0.38	25
	Jarosite		1.20	0.46	28
	Kaolinite		2.73	1.41	15
GUA1800	Goethite	481.3	-0.23	0.49	31
	Pyrite		0.62	0.38	24
	Jarosite		1.20	0.46	30
	Kaolinite		2.72	1.41	15
CAS284	Pyrite		0.63	0.30**	100
CAS1800	Pyrite		0.63**	0.30**	4
	Iron Sulfate		1.78	0.87	96

* The values for the isomeric shift are referenced with respect to α-Fe at room temperature.
**Fixed parameter

3. Results and Discussion

Three doublets and a sextet were used to fit the MS from the Guachinte mine samples, corresponding to the phases pyrite, jarosite, kaolinite and goethite, respectively (see Figure 1(a)). Compared to the spectrum of the non-irradiated natural sample (**Reyes *et al*** 2003), it shows that there is a reduction of pyrite in favor of jarosite, kaolinite sulfates and goethite for all radiation doses. The presence of goethite is due to the highly oxidizing conditions. The hyperfine parameters of the samples GUA284 and GUA1800 are listed in Table 1.

The resulting Mössbauer spectrum of the Las Casitas sample irradiated with 284 Gy (not shown here) is in agreement with the spectrum for the natural coal (***Reyes & Martinez*** 2013); which exhibits a unique phase associated to the mineral pyrite (see Table 1). It means that applying such low dose does not reduce the content of pyrite for this coal species. In contrast, the spectrum obtained for the CAS sample after the highest irradiation dose shows a significant reduction of the pyrite phase, accompanied by a major contribution of jarosite (see Figure 1(b)). The prominent doublet corresponding to jarosite has high values of the isomer shift and quadrupole splitting (Table 1). This can be explained by the presence in the structure of high spin Fe^{3+} (***Ahmed*** **et al.** 2011).

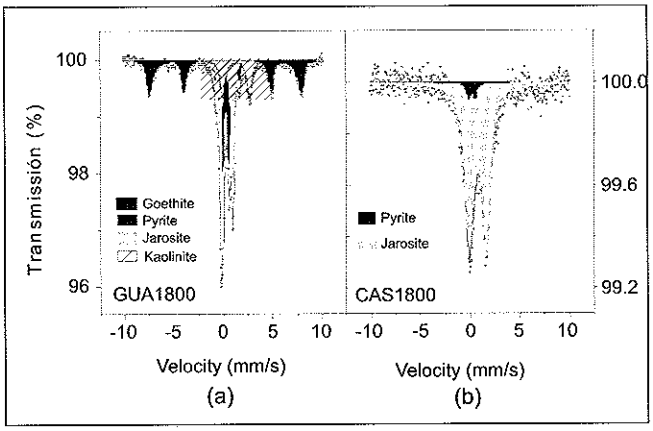

Figure 1. Mössbauer spectra at ~90 K obtained for the samples from (a) Guachinte and (b) The casitas after gamma irradiation of 1800 Gy.

Taking into account the differences between the Mössbauer results for each coal and comparing the chemical properties of them (**Reyes *et al*** 2003, ***Reyes & Martinez*** 2013), the effect of the irradiation is strongly correlated with the chemical features such as mineral matter, ash, and sulfur content.

In the energy range of 100 keV -10 MeV the radiation absorption is primarily due to Compton effect. In this case, approximately 99% of the gamma photons emitted from the ^{60}Co exhibit an energy of 1.17 MeV, and this radiation interacts with the sulfur. The S electronic configuration allows energy transfer from the photons to the S species, thus achieving the desired effect on the Fe-S minerals. This effect can be explained by the gamma radiolysis of the water present in the coals:

$$H_2O \overset{\gamma\, Rays}{\Rightarrow} H^*, e^-_{water}, OH^*, H_2O^+, H_2O_2, H_2^* \qquad (1)$$

Due to the presence of oxygen other products also can be formed. These radiolitic products generate an oxidizing atmosphere. It is expected that if the oxidation increases, the content of sulfides decreases in favor of ferrous and ferric sulfates and possibly a formation of oxyhydroxides takes place.

4. Conclusions

A high gamma radiation dose has been applied to coal samples obtained from two different Colombian mines. The samples, initially with high and low values of pyritic sulfur content, have been irradiated with the purpose of reaching their desulfurization. The Mössbauer results indicate that with the given radiation dose, the desired effect is only partly achieved, the sulfides being not fully removed. These finding suggests that the high costs and processes to obtain radioactive sources, and the physical changes, in locative terms, which are necessary for handling them would make the application of this method of desulfurization non-practical for thermoelectric companies that use coal for their fuel.

5. Bibliography

Ahmed, M. A., Mousa, M. A. A., Amami, S. M., Etmimi, K. M., & Ellid, M. S. (2011). Gamma Irradiation of Pyrite in Egyptian Coal as Studied by Means of Mössbauer Spectroscopy at Room Temperature. *Source Part A* 34 227-234.

ASTM, 1991. Annual Book of ASTM Standards.

Gracia, M., Marco, J. F., & Gancedo, J. R. 1999. Uses and perspectives of Mössbauer spectroscopic studies of iron minerals in coal. *Hyperfine Interact* **122**(1-2) 97-114

Huffman, G. P., & Huggins, F. E. 1978. Mossbauer studies of coal and coke: quantitative phase identification and direct determination of pyritic and iron sulphide sulphur content. *Fuel*, *57*(10), 592-604.

Ram, L. C., Tripathi, P. S. M., Jha, S. K., Sharma, K. P., Singh, G., & Mishra, S. P. 1997. γ-irradiation of coal and lignite: effect on extractability. *Fuel Process Technol.* **53** 1-14.

Reyes, F., Alcázar, G. P., Barraza, J. M., Bohórquez, A., Tabares, J. A., & Speziali, N. L. 2003. Mössbauer and XRD characterization of the mineral matter of coal from the Guachinte mine in Colombia. *Hyperfine Interact.* **148**(1-4) 39-46

Reyes F and Martinez Ovalle S A 2013 *Hyperfine Interact.*Mössbauer study of the inorganic sulfur removal from coals 10.1007/s10751-013-0874-x.

Tripathi, P. S. M., Mishra, K. K., Roy, R. R. P., & Tewari, D. N. 2001. γ-Radiolytic desulphurisation of some high-sulphur Indian coals catalytically accelerated by MnO_2. *Fuel Process Technol.* **70** 77-96

Vandenberghe, R. E., De Grave, E., & De Bakker, P. M. A. 1994. On the methodology of the analysis of Mössbauer spectra..*Hyperfine Interact.* **83** 29-49

ELECTROCHEMICAL STUDIES OF THE CORROSION RESISTANCE OF BISMUTH TITANATE THIN FILMS DEPOSITED BY RF SPUTTERING

ESTUDIOS ELECTROQUÍMICOS DE LA RESISTENCIA A LA CORROSIÓN DE PELÍCULAS DELGADAS DE TITANATO DE BISMUTO DEPOSITADO MEDIANTE SPUTTERING RF

Manuel Jonathan Pinzón Cárdenas[*,*], Jhon Jairo Olaya Florez[*,***], José Edgar Alfonso Orjuela[**,***]**

ABSTRACT

Pinzón Cárdenas M. J., J. J. Olaya Florez, J. E. Alfonso Orjuela: Electrochemical studies of the corrosion resistance of Bismuth titanate thin films deposited by RF sputtering. Rev. Acad. Colomb. Cienc., 37 (1): 79-84, 2013. ISSN 0370-3908.

Thin films of Bismuth titanate were grown on stainless steel (316L) and titanium alloy (Ti6Al4V) substrates, using the magnetron sputtering technique. The surface morphology of these films was observed with a scanning electron micrograph (SEM). The electrochemical studies used to evaluate the corrosion resistance of the substrate-coating set were the potentiodynamic polarization (Tafel) tests and electrochemical impedance spectroscopy (EIS), both done in a solution of NaCl (3%) as an electrolyte. The SEM showed that the morphology of the coatings grown on a titanium alloy Ti6Al4V substrate were in general homogeneous with a smooth surface but with un-melted material in some regions, while the morphology of the thin films grown on stainless steel 316L was mainly granular, with the presence of a few holes or craters. The potentiodynamic polarization curves showed that the corrosion resistance of the coated samples was better than that of the bare substrate, because the corrosion current obtained from the coated samples was lower by two orders of magnitude than that exhibited by the uncoated substrates, and in addition the corrosion potential of the coated samples was greater than that of the bare substrate. The EIS test showed the presence of a passive thin film of titanium oxide on the titanium alloy substrate.

Keywords: Bismuth Titanate, Thin films, Sputtering, Corrosion.

RESUMEN

Películas delgadas de Titanato de bismuto fueron crecidas sobre substratos de acero inoxidable (316L) y aleación de titanio (Ti6Al4V), utilizando la técnica de magnetrón Sputtering. La morfología de estas películas fue

* Departamento de Ingeniería Mecánica y Mecatrónica – Universidad Nacional de Colombia, Bogotá, Colombia

** Departamento de Física – Universidad Nacional de Colombia, Bogotá, Colombia. E-mail: jealfonsoo@unal.edu.co

*** Grupo de Ciencia de Materiales y Superficies, Universidad Nacional de Colombia, Bogotá, Colombia

observada con microscopio electrónico de barrido (MEB). Los estudios electroquímicos utilizados para evaluar la resistencia a la corrosión del conjunto substrato-recubrimiento fueron la prueba de polarización potenciodinámica (Tafel) y la espectroscopia de impedancias electroquímicas (EIS), ambas pruebas fueron hechas en una solución de NaCl (3%) como electrolito. El MEB mostro que la morfología de los recubrimientos crecidos sobre substratos de aleación de titanio Ti6Al4V fue homogénea en general con una superficie suave pero con presencia de material sin fundir en algunas regiones, mientras que la morfología de las películas crecidas sobre acero inoxidable 316L fue principalmente granular, con la aparición de algunos cráteres. Las curvas de polarización potenciodinámica muestran que la resistencia a la corrosión de las muestras recubiertas fue mejor que la de las muestras sin recubrir ya que la corriente de corrosión obtenida de las muestras recubiertas fue dos órdenes de magnitud menor que la exhibida por las no recubiertas, adicionalmente el potencial de corrosión fue mayor en las recubiertas que en las no recubiertas. El ensayo de EIS mostro la presencia de una capa pasiva de óxido de titanio en la superficie de los substratos de aleación de titanio.

Palabras clave: Titanato de bismuto, películas delgadas, Sputtering, Corrosión.

1. Introduction

Bismuth titanate compounds (Bismuth titanate) are present in different crystalline configurations [1], such as sillenite [2], aurivillius (Layered-Perovskite) [3, 4], and pyrochlore [5], as well as in the amorphous phase [6]. These configurations have been studied extensively for many years due to their versatility in fields such as electronics and optics. For instance, the sillenite structure ($Bi_{12}TiO_{20}$) exhibits high photocatalytic activity in many reactions as a photo-degradation of methyl orange under UV-light [7], and also has photorefractive and photoconductive properties, which make it an optically active material and allow it to exhibit electro-optic, piezoelectric, and elasto-optic effects that are interesting for use in applications such as optical memories and dynamic holography [8, 9]. Meanwhile, the aurivillius phase of bismuth titanate ($Bi_4Ti_3O_{12}$) exhibits interesting properties at high temperatures ($\leq$ 948 K), such as piezoelectricity and ferroelectricity, making it attractive for devices such as transductors and actuators, as well as for the automotive, aeronautic, and aerospace industries [3]. Furthermore, thanks to its reversible polarization, high dielectric constant, and electro-optic switching behavior, this compound is the object of special attention for applications such as non-volatile memories, capacitors of dynamic random-access memories, optical displays, and pyro-electric devices [10, 11]. The pyrochlore structure ($Bi_2Ti_2O_7$) has been the object of studies intended to take advantage of its optical properties and photocatalytic activities under visible-light [12]. Other research in this direction has proposed this compound as a material for use in the fabrication of advanced MOSFET transistors, taking advantage of its permittivity (relatively high) and low current leakage [13]. The foregoing information recounts a small part of the large number of studies done on the structural behavior, optical properties, and electrical properties of bismuth titanate. However, the number of studies devoted to the corrosion resistance and the electrochemical behavior of these materials is still very small. Therefore, in the present paper we present the results of the corrosion resistance of bismuth oxide grown in the form of a thin film.

2. Experimental Details

The equipment used to grow Bismuth titanate thin films was an Alcatel HS 2000 RF sputtering system with a balanced magnetron 4" in diameter. The Bismuth titanate thin films were obtained from a 4" x 1/4" $Bi_4Ti_3O_{12}$ (99.9%) stoichiometric target. The parameters used during the deposition process were: base pressure $4.0x10^{-5}$ mbar, total working pressure $7.4x10^{-3}$ mbar, power applied at the target 150W, substrate temperature 623K, gas flow (Argon) 20 sccm, deposition time 30 min., and target-substrate distance 2". The preparation of the samples was carried out in the following order: cleaning of the samples by immersing them in isopropyl alcohol in an ultrasonic bath for 5 min., drying (with dry air), mounting of the samples on the galvanic cell, and finally placing the galvanic cell inside a Faraday cage in order to minimize the effects of the magnetic and electrical fields in the environment. Analysis of the potentiodynamic polarization curves was done with GamryEchem Analyst software. The equipment used to carry out the potentiodynamic polarization tests and the electrochemical impedance spectroscopy (EIS) was a Gamry Instruments reference 600 potentiostat with a three-electrode configuration. The reference electrode used in this test was a Saturated Calomel Electrode (SCE), accompanied by a Platinum electrode as an auxiliary electrode, and as working electrodes the samples were used. For both corrosion tests a 3% solution of NaCl was used.

3. Results and Discussion

Under the experimental conditions in which the bismuth titanate thin films (T_s = 623 K) were grown, the XRD studies did not show a crystalline structure, because the temperature needed for crystallization was not reached, neither in the aurivillius nor in the pyrochlore phase (> 773K) [14, 15].

Furthermore, annealing was not was carried out, due to the fact that the sensitization temperature of the stainless steel substrate and the exposition time of the sample to this temperature didn't allow it, and neither was it done for the titanium alloy substrates, in order to maintain the same experimental conditions for both substrates.

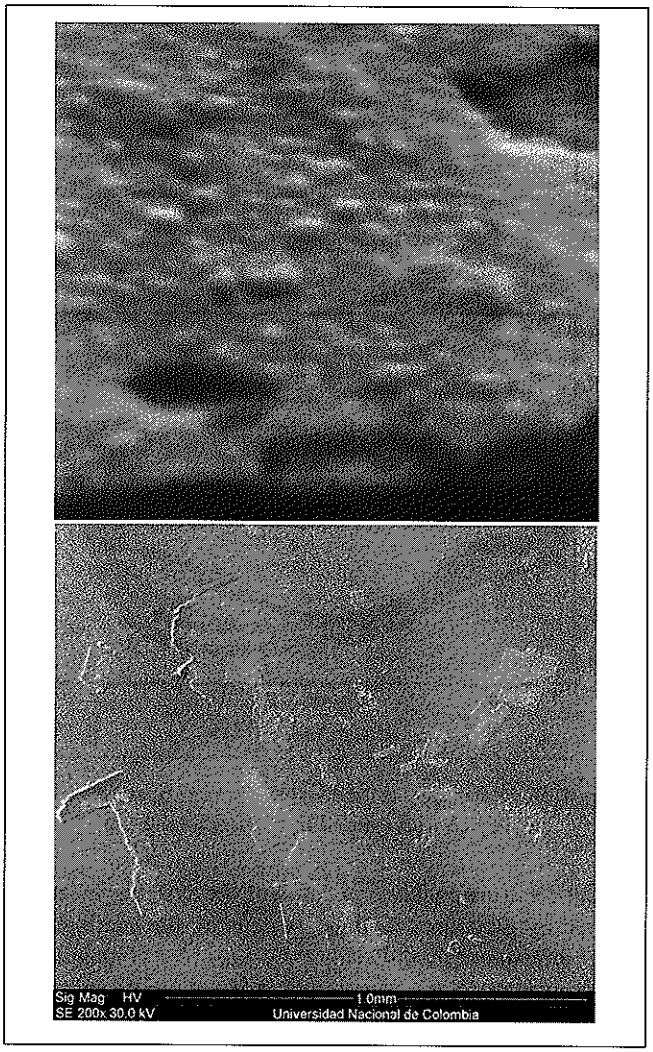

Figure 1. SEM of the surface of Bismuth titanate coating grown on stainless steel 316L (left) and titanium alloy Ti6Al4V (right).

The SEM (Fig. 1a) shows the surface of the Bismuth titanate coating on stainless steel 316L, in which one can observe that the morphology of the thin film is mostly granular; however, it also can be noted that there are a few holes or craters, which probably were formed through the re-sputtering effect. The grains that form the thin film have a size in the range of 0.028 to 0.17 μm^2, while the holes or craters have a size in the range of 0.22 o 1.1 μm^2. The SEM (Fig. 1b) shows the surface of the Bismuth titanate coating on titanium alloy Ti6Al4V, in which one can observe that the morphology of the thin film is homogeneous. However, it can also be noted that there is some un-melted material, which probably is due to the fact that the temperature is not homogeneous on the surface of the substrate.

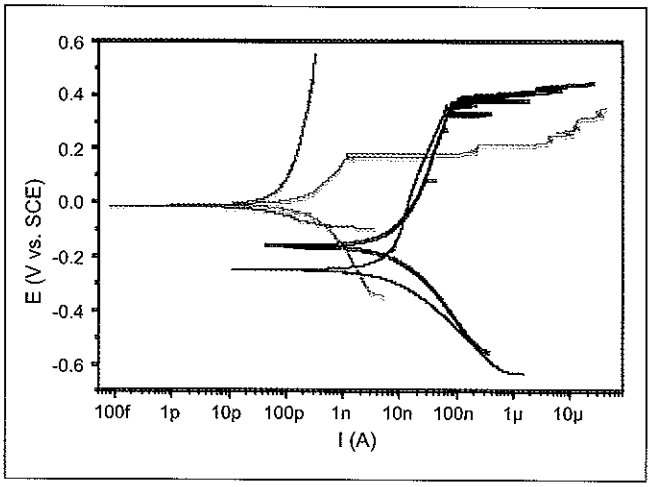

Figure 2. Potentiodynamic polarization curves obtained from stainless steel 316L substrate (black line), bismuth titanate thin film on stainless steel substrate (orange line), titanium alloy Ti6Al4V substrate (blue line) and bismuth titanate thin film on titanium alloy Ti6Al4V (green line).

The potentiodynamic polarization curves obtained from the samples of stainless steel 316L (Fig. 2, uncoated: black curve, and coated with BiTIO film: orange curve) show that the corrosion current (i_{corr}) decreases and the corrosion potential (Ecorr) increases in the samples coated with bismuth oxide with respect to the uncoated samples. This is due to the fact that the thin film exhibits a protective behavior, since we found that the film surface is composed of Bi_2O_3 and TiO_2, the latter oxide being a protection against corrosion [16, 17]. However, it is worth noting that although both i_{corr} and E_{corr} improved considerably with the application of the thin film onto the substrate surface, the appearance of possible pitting corrosion (current increase at the anodic region) occurs at a lower potential with the coating than without it. This behavior is due to the fact that the Bismuth titanate film is formed with holes through which the electrolyte penetrates.

Moreover, the potentiodynamic polarization curves obtained for the titanium alloy (Fig. 3, substrate: blue curve, and coated sample: green curve) shows that the coated sample exhibits a decrease in the corrosion current (i_{corr}) and an increase in the corrosion potential (E_{corr}) with respect to the uncovered samples, which is mainly due to the passive film

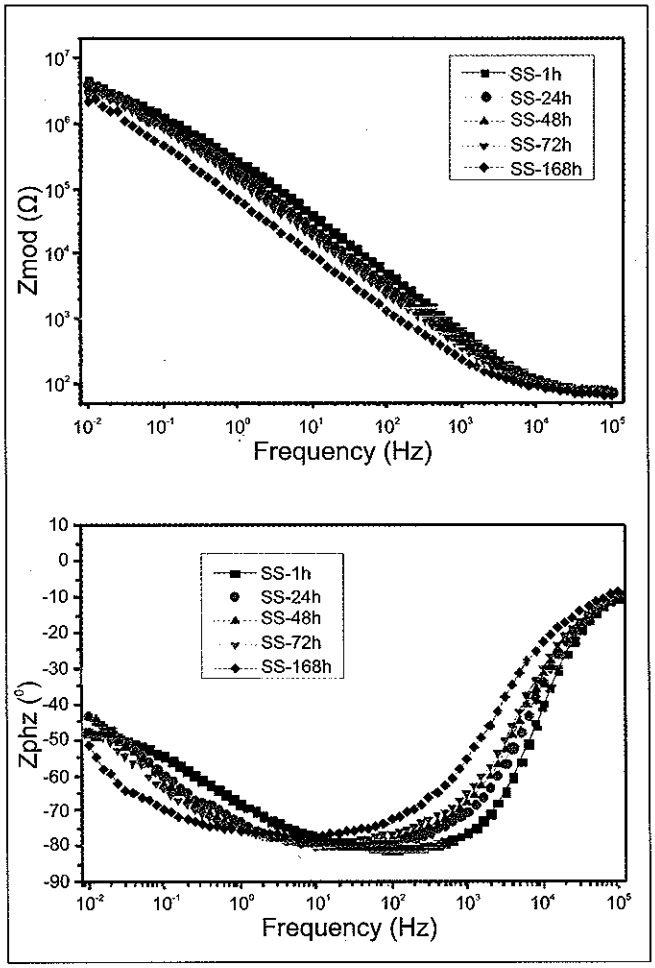

Figure 3. Bode diagram obtained from stainless steel 316L bare substratum.

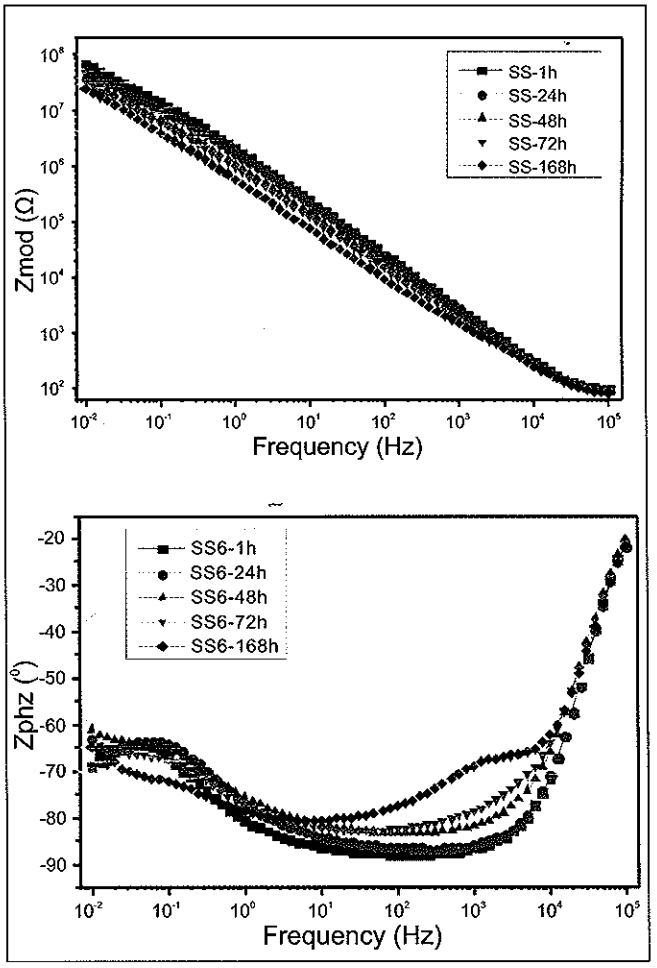

Figure 4. Bode diagram, obtained from stainless steel 316 substratum coated with a thin film of Bismuth titanate.

of TiO_2 spontaneously grown on the titanium substrate, since it behaves as a protective thin film [18]. It is noteworthy that the behavior of the anodic region of the titanium alloy and of stainless steel is very different, since in the first substrate there is a passivation zone that is not present in the stainless steel substrate.

Bode plots for the stainless steel 316L substrate (Fig. 3) and the Bismuth titanate coatings (Fig. 4) show the immersion time in the corrosive electrolyte, which shows the presence of a relaxation time at high frequencies, representing the dielectric nature of the coating and the passive film formed on the substrate. This layer is generated by diffusing oxygen from the electrolyte onto the substrate surface through permeable paths (pores and defects), forming a thin film of low conductivity whose capacitance has a dielectric constant approximately to the coating. The variation in the height of the peak of the relaxation times at high frequencies suggests that the electrochemical properties of the systems tested are affected by the exposure time. In general, the coatings had higher impedance module values by one order of magnitude, at a frequency of 10^{-2} Hz, compared to the bare substrate. Such a Bode pattern possibly was due to the formation of a dense and compact structure that reduced the number of defects such as cracks, pinholes, and pores within the coatings, thereby further restricting corrosive electrolyte diffusion. The relatively small changes observed in the Bode spectra suggest considerable electrochemical stability for the coating due to the obstruction of defects by means of the corrosion products.

In summary, the steel substrate shows an increase in the impedance module when the immersion time is reduced, because the electrolyte diffusion through the coating took less time, producing a dense, passive, low-conductivity oxide film at the bottom of the permeable defects, exhibiting a ca-

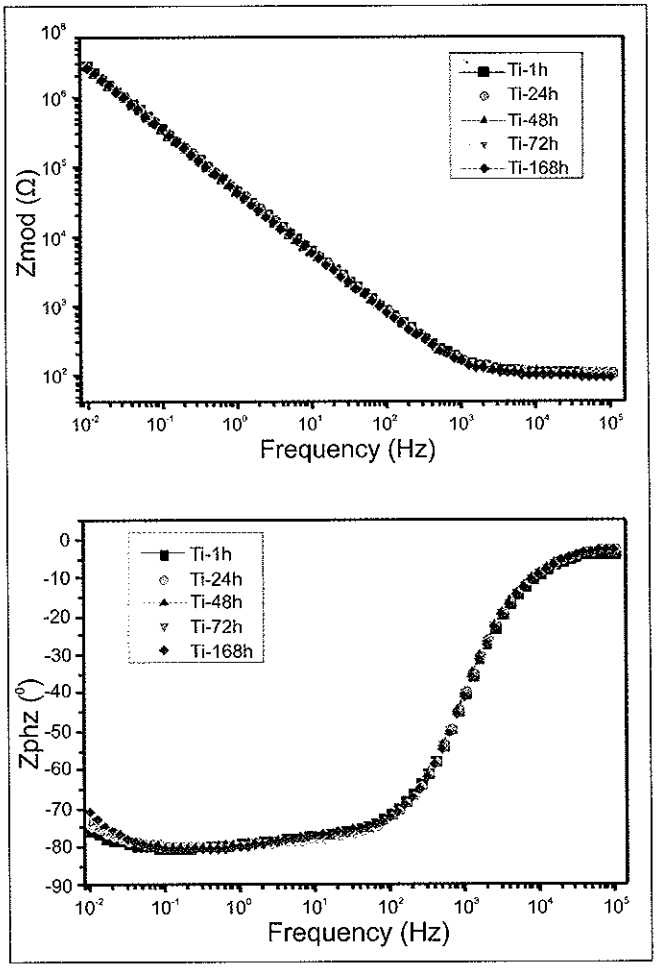

Figure 5. Bode diagram obtained for titanium alloy Ti6Al4V bare substratum.

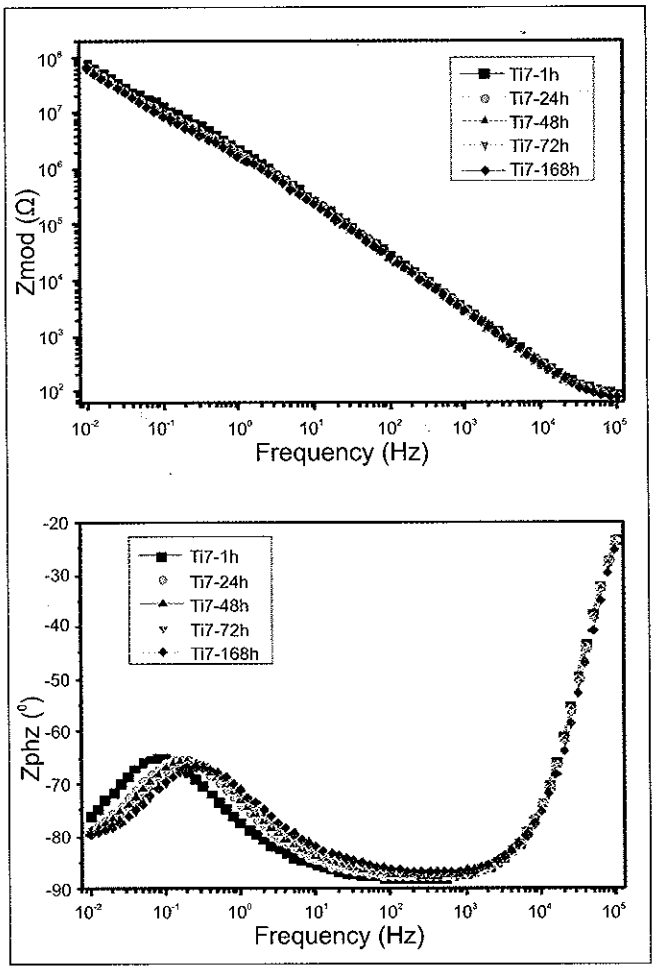

Figure 6. Bode diagram obtained for titanium alloy Ti6Al4V substratum coated with a thin film of Bismuth titanate..

pacitive behavior very similar to that of ceramic coatings. This behavior led to substrate surface passivity, which could dominate the corrosion process at the coating/substrate interface. However, increased immersion time expands the area of the pores in the coating, producing greater penetration of the corrosive solution toward the substrate surface, which produces localized corrosion.

A similar Bode pattern was seen for the titanium alloy Ti6Al4V substrate (Fig. 5) and the Bismuth titanate coatings (Fig. 6). However, the plots show one constant time, representing the capacitive response of the coating and the passive titanium alloy film. The relaxation time position remains unchanged, indicating no significant degradation of the coating as a function of testing time. The film deposited on Ti6Al4V exhibited the highest impedance module (~$7x10^8\Omega$ at 10-2 Hz) of all the coatings evaluated in this investigation, probably due to the strong influence of electrochemically inert passive films formed on Ti6Al4V.

4. Conclusions

Bismuth titanate thin films were grown on stainless steel (316L) and titanium alloy (Ti6Al4V) substrates through the rf magnetron sputtering technique, and their corrosion resistance was assessed via electrochemical techniques (potentiodynamic polarization and electrochemical impedance spectroscopy). These films exhibited a granular morphology with few craters for the stainless steel 316L, and un-melted material for the titanium alloy Ti6Al4V substrate. The electrochemical mechanisms that explain the increase of the corrosion resistance for the coated titanium alloy substrate obey the formation of the TiO_2 passivation layer, whereas for the coated stainless steel substrate the pitting currentis due to

the penetration of the electrolyte through the holes present on the surface of the films.

Acknowledgments

The authors are grateful to the Universidad Nacional de Colombia for its financial support grants through project 15059 of the DIB, and for European Union FP7-NMP EU-Mexico program under *grant agreement* n°263878.

References

[1] **K. Sardar, R.I. Walton,** (2012), Hydrothermal synthesis map of bismuth titanates, J. Solid. State. Chem., **189,** 32 - 37.

[2] **V.M. Skorikov, Yu. F. Kargin, A.V. Egorysheva, V.V. Volkov, M. Gosponidov,** (2005), Growth of Sillenite-structure single crystals, Inorg. Mater+., **41**, S24 – S46.

[3] **T. Jardiel, A.C. Caballero, M. Villegas,** (2008), Aurivillius ceramics $Bi_4Ti_3O_{12}$ based piezoelectrics, J. Ceram. Soc. Jpn. **116,** 511 - 518.

[4] **W.F. Yao, X.H. Xu, H. Wang, J.T. Zhou, X.N. Yang, S.X. Shang, B.B. Huang,** (2004), Photocatalytic property of perovskite bismuth titanate, Appl. Catal. B-Environ. **52**, 109 - 116.

[5] **I. Radosavljevic, J.S.O. Evans, A.W. Sleight,** (1998), Synthesis and structure of pyrochlore-Type Bismuth titanate, J. Solid. State. Chem., **136,** 63 - 66.

[6] **S. Kojima, A. Hushur, F. Jiang, S. Hamazaki, M. Takashige, M.S. Jang, S. Shimada,** (2001), Crystallization of amorphous bismuth titanate, J. Non-Cryst. Solids., **293-295**, 250 - 254.

[7] **J. Hou, Z. Wang, S. Jiao, H. Zhu,** (2011), 3D $Bi_{12}TiO_{20}/TiO_2$ hierarchical heterostructure, Synthesis and enhanced visible-light photocatalytic activities, J. Hazard. Mater., **192,** 1772 - 1779.

[8] **A.V. Egorysheva,** (2009), Atomic structure of doped sillenites, Inorg. Mater+., **45**, 1175 - 1182.

[9] **N.C. Deliolanis, E.D. Vanidhis, N.A. Vainos,** (2006), Dispersion of electrogyration in sillenite crystals, Appl. Phys. B., **85,** 591 - 596.

[10] **F. Soares-Carvalho, P. Thomas, J.P. Mercurio, B. Frit,** (1997), $Bi_4Ti_3O_{12}$ Thin Films from Mixed Bismuth-Titanium Alkoxides, J. Sol-Gel Sci. Techn., **8,** 759 - 763.

[11] **A.M. Umabala, M. Suresh, A.V. Prasadarao,** (2000), Bismuth titanate from coprecipitated stoichiometric hydroxide precursors, Mater. Lett., **44,** 175 - 180.

[12] **J. Hou, S. Jiao, H. Zhu, R.V. Kumar,** (2011), Bismuth titanate pyrochlore microspheres, Directed synthesis ad their visible light photocatalytic activity, J. Solid. State Chem. **184,** 154 - 158.

[13] **J. Harjuoja, S. Väyrynen, M. Putkonen, L. Niinisto, E. Rauhala,** (2006), Crystallization of bismuth titanate and bismuth silicate grown as thin films by atomic layer deposition, J. Cryst. Growth., **286**, 376 - 383.

[14] **Z. Wang, D. Sun, J. Hu, D. Cui, X. Xu, D. Wang, Y. Zhang, M. Wang, H. Wang, H. Chen, C. Fang, X. Liu, K. Wei, J.,** (2002), The reactive ion etching of $Bi_2Ti_2O_7$ thin films on silicon substrates and its image in atomic force microscopy, Cryst. Growth., **235**, 411 - 414.

[15] **M. Sedlar, M. Sayer,** (1996), Structural and electrical properties of ferroelectric bismuth titanate thin films prepared by the sol gel method, Ceram. Int., **22**, 241 - 247.

[16] **J.E. Alfonso, J.J. Olaya, M.J. Pinzón, J.F. Marco,** (2013), Potentiodynamic Polarization Studies and Surface Chemical Composition of Bismuth Titanate ($Bi_xTi_yO_z$) Films Produced through Radiofrequency Magnetron Sputtering, Materials, **6**, 4441 - 4449.

[17] **J. Pan, D. Thierry, C. Leygraf,** (1996), Electrochemical impedance spectroscopy study of the passive oxide film on titanium for implant application, Electrochim. Acta., **41**, 1143 - 1153.

[18] **J. Pouilleau, D. Devilliers, F.Garrido, S. Durand-Vidal, E.Mahé,** (1997), Structure and composition of passive titanium oxide films, Mat. Sci. Eng. B., **47**, 235 - 243.

DETERMINATION OF THE KINETIC PARAMETERS OF THERMOLUMINESCENT GLOW CURVES OF SINTERED AL_2O_3 PILLS BY THREE POINTS METHOD

DETERMINACIÓN DE LOS PARÁMETROS CINÉTICOS EN CURVAS DE BRILLO TERMOLUMINISCENTES DE PASTILLAS SINTERIZADAS DE AL_2O_3 POR EL MÉTODO DE LOS TRES PUNTOS

Mara Edith Pérez Díaz*, Rafael Ricardo Cogollo Pitalúa*, Omar Darío Gutiérrez Flórez**

ABSTRACT

Pérez Díaz M. E.*, R. R. Cogollo Pitalúa, O. D. Gutiérrez Flórez: Determination of the Kinetic Parameters of Thermoluminescent Glow Curves of Sintered Al_2O_3 Pills by Three Points Method. Rev. Acad. Colomb. Cienc., 37 (1): 85-89, 2013. ISSN 0370-3908.

The three points analysis method, proposed by Rasheedy, was applied to separate a complex thermoluminescence (TL) glow curve into its individual components and determine, for each component, the kinetic parameters. These are the order of kinetics b, the activation energy E (eV), and the pre-exponential factor S´´(s-1) associated with the TL glow peaks in sintered pure Al_2O_3 pills in response to gamma irradiation. The three points analysis method indicated that the glow curve of this material is the superposition of three general-order components, in which, the recombination processes predominates over retrapping processes.

Key words: alumina dosimeters, kinetic parameters determination, three points method.

RESUMEN

En este trabajo se aplicó el método de los tres puntos, propuesto por **Rasheedy**, para separar una curva de brillo termoluminiscente (TL) compleja en sus componentes individuales y determinar, para cada componente, los parámetros cinéticos. Estos parámetros son el orden cinético *b*, la energía de activación *E* (eV) y el factor pre-exponencial *S´´*(s^{-1}), asociados con las curvas de brillo TL en pastillas puras sinterizadas de Al_2O_3 expuestas a radiación gamma. El análisis con el método de los tres puntos indicó que la curva de brillo de este material se debe a la superposición de tres componentes TL de orden general, en los cuales, los procesos de recombinación predominan sobre los procesos de reatrapamiento.

Palabras clave: dosímetros de alúmina, determinación de parámetros cinéticos, método de los tres puntos.

* Materials and Applied Physics Group, University of Córdoba, Carrera 6 # 76-103, Montería, Colombia. E-mail: marepd16@gmail.com

** Alquimia Group, Metropolitan Technological Institute, Street 54a # 30-01, Medellín, Colombia.

1. Introduction

Thermoluminescence dosimetry has found a very important use in clinical, personal and environmental monitoring of ionizing radiation [McLaughlin et al., 1989; Daniels et al., 1953; Vaijapurkar, Bhatnagar, 1993; Mckeever et al., 1995; Rasheedy et al., 2007; Kortov, 2007; Pérez, 2010]. Aluminum oxide is a promising alternative to the thermoluminescent materials currently used for in vivo dosimetry in quality control programs. The interest in alumina increased with the development of new materials on the basis of its structure, like α-Al_2O_3:C, which contain oxygen vacancies and provide a high TL sensitivity [Pérez, 2010; Rocha et al., 2003].

In the TL materials, the kinetic analysis of TL glow curves allows to study its dosimetric properties [Daniels, 1953; Mckeever, 1995; Pérez, 2010]. Additionally, a TL glow curve usually corresponds to a superposition of one or more curves (complex curve), and this disables to apply the conventional methods for isolated TL glow peaks. In order to analyze complex TL glow curves, **Rasheedy** has introduced the three points method for separating a complex curve into its TL individual components and to evaluate the kinetic parameters for each component [Rasheedy, 2007; Pérez, 2010; Rasheedy, 2005].

In this paper we determine, employing the three points method (TPM), the kinetic parameters in the TL glow curves exhibited by the alumina studied. The glow curve of this material includes three overlapped glow peaks.

2. Experimental

2.a. Processing

Commercial Alumina (W. R. Grace & Co-Conn) was used to prepare sintered pure Al_2O_3 pills of 2.5 mm of radius and 1 mm of thickness. The powder was initially cold-pressed (2 ton) and then sintered at 1000°C in air for 3 h; later the pills were milled, compacted and sintered again at the same conditions.

2.b. Thermoluminescence tests

Irradiations of samples, using absorption dose of 10 Gys, were carried out in air at room temperature using a Theratron 780C-^{60}Co unit at a distance of 80 cm relative to the source, in a radiation field of 10 x 10 cm^2. The samples were placed between two acrylic plates of 5 mm of thickness, with the purpose of reaching the conditions of electronic equilibrium. Thermoluminescence measurements were performed using a commercial Harshaw TLD 4500 dosimeter manufactured by Bicron®, using a linear heating rate of 5 Ks^{-1} from 50 °C up to 360 °C. The readings were carried out in a N_2 atmosphere in order to eliminate the infrared contribution due to the heating and to reduce the moisture effects. In order to reduce the residual signal of the material before each irradiation, allowing their re-utilization, samples were then annealed at 400 °C/1h (heating rate of 12.5 K/min), followed by cooling in air until to reach room temperature.

2.c. Structural and thermoluminescent analysis

Sinterized samples were characterized by means of X-ray diffraction (XRD). The diffractograms were obtained at room temperature by means of a X'Pert PRO (PANalytical) diffractometer using a copper source $K_{\alpha 1}$ λ=1.54056 Å to a sweeping rate of 0.026°/s.

Glow curves obtained were analyzed using the TPM proposed by **Rasheedy** [Pérez, 2010; Rasheedy, 2005], for obtaining the kinetic parameters of the individual glow peaks in a complex glow curve. These parameters include the order of kinetics b, the activation energy E (eV), the pre-exponential factor S'' (s^{-1}) and the initial concentration of trapped electrons n_0 (cm^{-3}).

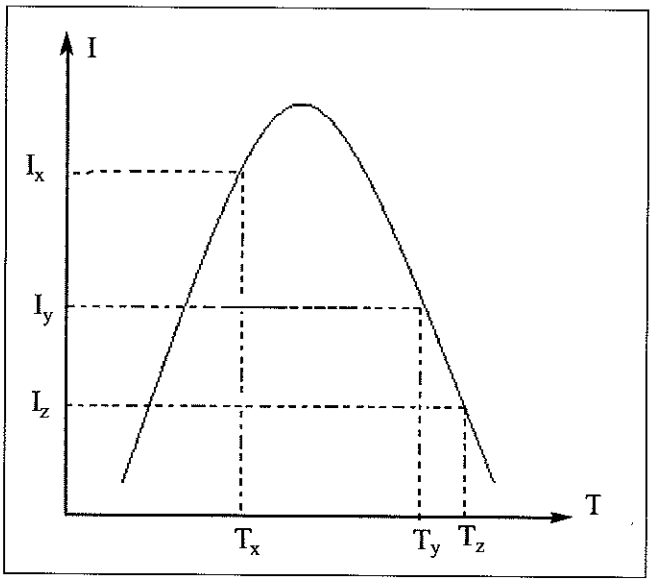

Figure1. Parameters I_x, I_y, I_z, T_x, T_y y T_z, in an isolated TL glow peak [Rasheedy, 2007].

This technique is applicable in TL curves consisting of multiple peaks and determines, by a general equation, the order b based on a set of three data points in an experimental TL glow curve (see Fig. 1) , considering that for general order kinetics, the behavior of TL intensity of a phosphor is governed by the following equation [Rasheedy, 2007; Rasheedy, 2005]:

$$I = -\frac{dn}{dt} = \frac{n^b}{N^{b-1}} S \exp\left(\frac{-E}{kT}\right) \quad (1)$$

Where I (in arbitrary units) is the TL intensity, n (cm^{-3}) the electron concentration trapped at time t (s), N (cm^{-3}) the traps concentration and k (eV/K) is the Boltzmann's constant. The solution of Eq. (1) for $b \neq 1$ is given by:

$$I = \frac{n_o S'' \exp(-E/kT)}{\left[1+\left[((b-1)S'')/\beta\right]\int_{To}^{T} \exp(-E/kT')dT'\right]^{b/(b-1)}} \quad (2)$$

Where β (Ks^{-1}) is the linear heating rate and n_0 (cm^{-3}) is the concentration of traps populated at the starting heating temperature T_0 (K). The pre-exponential factor S'' (s^{-1}), which is defined as $S''=S(n_0/N)^{b-1}$ is constant for a given dose, but it varies with changing the absorbed dose, i.e., with n_0. With equation (2) and the parameters b, E and S'', it will be possible to simulate the TL response in the alumina matrices studied.

From the TPM, the order of kinetics b is given by:

$$b = \frac{T_y[T_x - T_z]ln(y) - T_z[T_x - T_y]ln(z)}{T_y[T_x - T_z]ln\left[\frac{A_x}{A_y}\right] - T_z[T_x - T_y]ln\left[\frac{A_x}{A_z}\right]} \quad (3)$$

Where A_x, A_y and A_z indicate the areas under the glow peak from the temperatures T_x to T_f, T_y to T_f and T_z to T_f, respectively. There are not any relations between the intensities at which T_x, T_y and T_z exist. Also, T_x can antecede T_y (and/or T_z) or vice versa. The values of y and z are given by $y = I_x/I_y$ and $z = I_x/I_z$. The activation energy E is given either by

$$E = \left\{(\ln y) - b\ln[A_x/A_y]\right\}\left\{\frac{kT_xT_y}{T_x - T_y}\right\} \quad (4)$$

Or by

$$E = \left\{(lnz) - bln[A_x/A_z]\right\}\left\{\frac{kT_xT_z}{T_x - T_z}\right\} \quad (5)$$

Now, with b and E parameters the pre-exponential factor S'' is given by:

$$S'' = \frac{\beta E \exp(E/kT_m)}{[bkT_m^2] - (b-1)E\varnothing\exp(E/kT_m)} \quad (6)$$

Where T_m (K) is the temperature corresponding to the maximum intensity, I_m, of the glow peak and,

$$\varnothing = \int_{To}^{Tm} \exp\left(\frac{-E}{kT'}\right)dT' \quad (7)$$

Finally, inserting (6) into (2) can be obtained an analytical expression for n_0:

$$n_o = \frac{I_m \exp(E/kT_m)}{S''}\left(\frac{bkT_m^2 S''}{\beta E \exp(E/kT_m)}\right)^{b/(b-1)} \quad (8)$$

In equation (8), the parameters b, E, S'' y β are known, and the values of I_m and T_m can be obtained from experimental glow curve.

The quality of **Rasheedy**'s fit has been tested with the figure of merit (FOM) [Bos et al., 1994], where FOM is given by

$$FOM = \sum_p \frac{100\,|\,y_{experimental} - y_{fit}\,|}{Area_{fit}} \quad (9)$$

Where $y_{experimental}$ and y_{fit} represent the experimental data and the values of the fitting function correspondingly. The summation extends over all the available points and $Area_{fit}$ represents the integral of the fitted glow curve. Glow curves with FOM values in excess of 5%, must be examined by another technique of deconvolution, because in these cases the fit is not as accurate.

3. Results

3.a. Structural and thermoluminescent analysis

Crystalline phase analysis (Fig.2) by means of Rietveld refinement [Pérez, 2010], revealed the presence of the α-alumina with rhombohedric structure and lattice parameters a=b= 4.75793 Å, c =12.989945 Å; and approximate crystal size of 2038.9 Å.

3.b. Kinetic analysis

Figure 3 shows the whole experimental TL glow curve obtained for the alumina samples.

Let us start with obtaining the kinetic parameters of the higher temperature peak, labelled peak 1. The value of b for this peak is calculated according to Eq. (3) at randomly selected Tx, Ty and Tz points of the rising and descending part of this peak, since the peaks 1 and 2 don't exhibit important overlapping. The activation energy E is determined according to

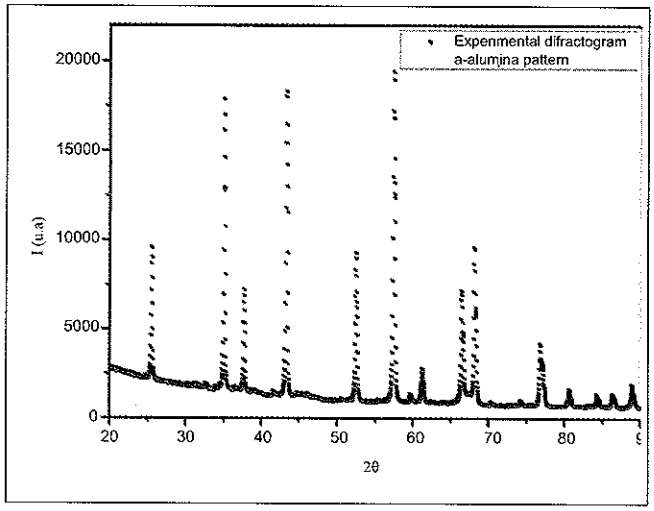

Figure 2. XRD pattern of the phase present into alumina samples.

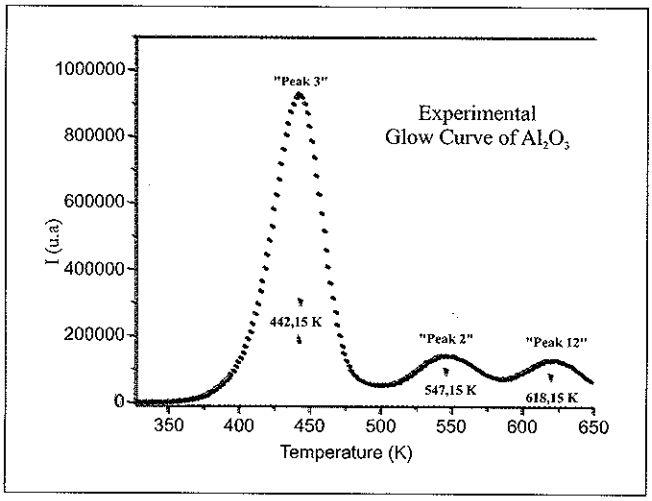

Figure 3. Experimental TL Glow Curve of alumina samples.

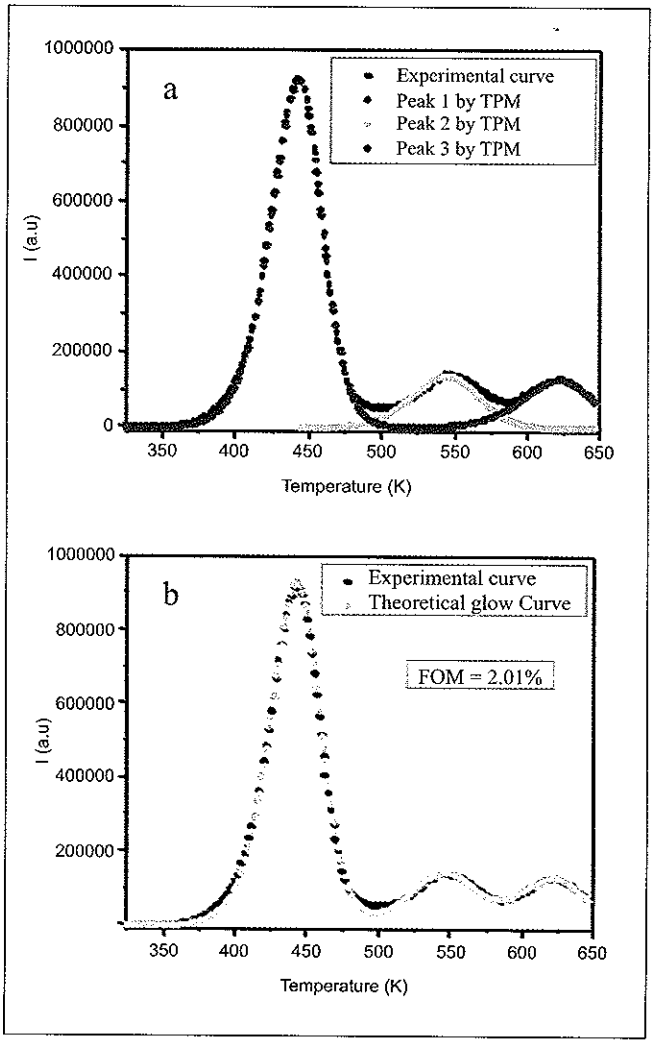

Figure 4. (a) Theoretical peaks obtained by TPM. (b) Experimental and fitted (summation of the theoretical peaks 1-3) curves.

Eqs. (4) or (5), while the pre-exponential factor S'' is estimated according to Eq. (6). Finally, the relative value of n_o is estimated according to Eq. (8). Later, we used the resulting parameters, β, b, E, S'' and n_o in Eq. (2) to fit the experimental glow peak 1 into a theoretical one. Then, the theoretical peak 1 was subtracted from the experimental glow curve and, over the remaining experimental glow curve, the mentioned procedures were repeated to obtain the kinetic parameters for peak 2 (employing in this case only the points of the descending part) and, once again, to obtain these parameters for the last peak 3. It is worth mentioning that, first, twenty runs of the TPM were executed in order to obtain average values of the kinetic parameters to generate each theoretical peak; and second, three theoretical peaks were enough to fit and to describe the whole experimental TL glow curve.

Fig. 4(a) shows the three theoretical peaks and the whole experimental glow curve. As shown in Fig. 4(b), the summation of theoretical peaks, fits well to the experimental glow curve (FOM value < 5%).

In the table 1 the kinetic parameters of each theoretical peak are listed. From the kinetic order b, it can be seen that recombination processes prevails over retrapping processes for peak 1 and 3, while for the peak 2 both processes occur.

On the other hand, the values of the activation energy for each peak are in agreement with the experimental observation since $E_{peak1} > E_{peak2} > E_{peak3}$. Similarly, the values of the initial concentration of trapped electrons n_o, show an agreement between their increment and the intensity of each peak,

Table 1. Experimental and kinetic (by TPM) parameters for peaks 1-3

Parameters	Peak 3	Peak 2	Peak 1
Tm (K)	442	543	622
Im (a.u)	9.28E+05	1.41E+05	1.29E+05
T0 (K)	323	444	544
b (K/s)	5	5	5
b	1.45	1.52	1.32
E (eV)	1.15431	1.3757	1.62579
S" (s-1)	4.86E+12	1.46E+12	3.58E+12
no (cm-3)	8.46E+06	1.67E+06	1.56E+06
FOM (%)	2.01		

since this parameter is proportional to the maximum Intensity of the TL peak.

4. Conclusions

The FOM value indicates that the three point method is valid as deconvolution analysis for the alumina investigated.

The three points method shows that experimental TL glow curve of alumina, only consists of three types of energy traps, since the overlapping of the theoretical peaks doesn't reveal the appearance of another signals.

The kinetic order indicates that the recombination prevails on the retrapping in the three types of energy traps that compose the experimental TL glow curve of alumina samples. Although for the "Peak 2" the method proposes a mixed deactivation mechanism in which the recombination prevails on the retrapping (b~1.5).

References

Bos A.J.J, Piters T.M, Gomez-Ros J.M, Delgado A. (1994). An Intercomparison of Glow Curve Analysis Computer Programs: II. Measured Glow Curves. Radiat. Prot. Dosimetry. 51(4): 257–264.

Daniels F, Boyd C, Saunders D. (1953). Thermoluminescence as a research tool. Science. 117, 343-349.

Kortov V. (2007). Materials for thermoluminescent dosimetry: Current status and future trends. Radiat. Meas. 42, 576-581.

Mckeever Stephen, Moscovitch Marco, Townsend Peter. (1995). Thermoluminescence Dosimetry Materials: properties and Uses. Ed 1. Ashford. Nuclear Technology Publishing.

McLaughlin W.L, Boyd A.W, Chadwick K.H, McDonald J.C, Miller A. (1989). Dosimetry for Radiation Processing. Ed 1. Taylor & Francis, London.

Pérez Mara Edith. (2010). Análisis de Curvas de Brillo Termoluminiscentes y Determinación de los Parámetros Cinéticos en Pastillas Sinterizadas de Al2O3. Trabajo Dirigido de Grado, Universidad de Córdoba, Departamento de Física y Electrónica. Monteria, Colombia.

Rasheedy M.S. (2005). A new evaluation technique for analyzing the thermoluminescence glow curve and calculating the trap parameters. Thermochimica Acta. 429, 143–147.

Rasheedy M.S, El-Sherif M.A, Hefni M.A. (2007). Determination of the trapping parameters of thermoluminescent glow peaks of K2YF5:Ce by three points method. Nucl. Instr. and Meth. in Phys. Res. B. 258, 440–444.

Rocha F.D.G, Oliveira M.L, Caldas L.V.E. (2003). Thin sintered Al2O3 pellets as thermoluminescent dosimeters for the therapeutic dose range. Applied Radiation and Isotopes. 58, 719–722.

Vaijapurkar S, Bhatnagar P. (1993). Low cost thermoluminescence (TL) gamma dosimeter for radiotherapy. Nucl. Tracks Radiat. Measur. 21(2): 267-269.

CHARACTERIZATION OF CR/CRN NANO MULTILAYERS OBTAINED THROUGH REACTIVE SPUTTERING WITH DIFFERENT DEGREES OF UNBALANCE IN THE MAGNETRON

CARACTERIZACIÓN DE NANOMULTICAPAS DE Cr/CrN OBTENIDAS POR SPUTTERING REACTIVO CON DIFERENTES GRADOS DE DESBALANCE EN EL MAGNETRÓN

Ulises Piratoba Morales*, Jhon Jairo Olaya Flórez**

ABSTRACT

Piratoba Morales U., J. J. Olaya Flórez: Characterization of Cr/CrN nano multilayers obtained through reactive sputtering with different degrees of unbalance in the magnetron. Rev. Acad. Colomb. Cienc., 37 (1): 90-93, 2013. ISSN 0370-3908.

Nanoscale hard coatings of bilayers of Cr/CrN were obtained and characterized through unbalanced magnetron sputtering (UBMS) in an atmosphere of Ar and Ar + N_2 on silicon and hardened and tempered H13 steel, with a degree of unbalanced K_G between 0.87 and 1.37. The deposition parameters were as follows: a power of 160 watts, Ar and N_2 flow rates of 9 and 3 sccm, and a substrate target distance of 5 cm. A Gencoa VT 100 magnetron with varying degrees of unbalance, obtained by displacing its central magnet, was used. The electrochemical behavior of these coatings was characterized using the technique of potentiodynamic anodic polarization. The coatings' microstructure and hardness were analyzed via X-ray diffraction (XRD) and nanoindentation tests; Cr, CrN and Cr_2N phases were obtained, with a hardness that increases with the degree of unbalance between 18.90 and 24.97 GPa.

Key words: Hard coatings; Cr/CrN, Sputtering; Unbalanced magnetron.

RESUMEN

Se obtuvieron y caracterizaron recubrimientos duros a escala nanométrica, de bicapas de Cr/CrN, mediante sputtering con magnetrón desbalanceado (UBMS) en atmósferas de Ar y Ar + N_2 sobre silicio y sobre acero H13 endurecido y templado, con grados de desbalance KG entre 0.87 y 1.37. Los parámetros de la deposición fueron los siguientes: una potencia de 160 vatios, flujos de Ar y N_2 de 9 y 3 sccm y una distancia blanco-sustrato de 5 cm. Se utilizó un magnetrón Gencoa VT 100 con diversos grados de desbalance, obtenidos por el desplazamiento de su imán central. El comportamiento electroquímico de estos recubrimientos se caracterizó

* Escuela de Física, UPTC Tunja, Colombia

** Departamento de Ingeniería Mecánica y Mecatrónica, Universidad Nacional de Colombia, AA 5997 Bogotá, Colombia

mediante la técnica de polarización anódica potenciodinámica. La microestructura y dureza de las multicapas fueron analizadas mediante difracción de rayos X (DRX) y análisis de nanoindentación; se obtuvieron fases de Cr, CrN y Cr2N, con durezas entre 18.90 y 24.97 GPa que aumentaron con el grado de desbalance.

Palabras clave: Recubrimientos duros; Cr/CrN, Sputtering; Magnetrón desbalanceado.

1. Introduction

Chromium, hard chromium, and chromium nitride are well known as coatings for protection of metallic materials [1, 2]. Titanium nitride (TiN) has been extensively researched and positioned as a prototype for hard coatings. TiN is now still being widely used in protective coatings for bearings, gears, and cutting and forming tools. However, the fracture toughness and the oxidation resistance of TiN coatings are not satisfactory for many advanced engineering applications, and it has been replaced in many advanced applications by CrXN. Although the hardness of CrN is slightly lower than that of TiN, its performance is superior in other ways: it has a lower friction coefficient, increased wear resistance, and a toughness that prevents crack initiation and propagation; CrN has a higher resistance to oxidation, erosion and corrosion [3, 4, 5, 6], is more stable at high temperatures, grows with lower residual stresses, and can achieve growth rates up to 3 times higher than TiN [7, 8]. New hard coatings have been obtained by the addition of further elements to produce ternary or quaternary systems [9] or nanoscale multilayers that increase the hardness and toughness as the period is reduced. Coatings with alternating configurations of pure metal and metal nitride exhibit superior mechanical and tribological properties [10,11,12].

The efficiency of the physical vapor deposition (PVD) process and the deposits' characteristics have been improved by applying magnetic fields in order to concentrate the plasma around the target, increasing the ionization processes. Unbalanced magnetron sputtering (UBMS) is one of the most effective systems for depositing high-quality coatings, as a consequence of the higher ion current densities and enhanced ion bombardment available during the deposition process. This bombardment causes a small warming in the substrate and provides the energy that facilitates the diffusion processes of adsorbed atoms, forming layers with a lower density of defects, especially vacancies, and lower residual stresses. Many of the articles on UBM provide little information on the relative intensities of the two magnetic poles or on their geometric arrangement; a systematic study of these aspects and their correlation with the coating's properties is therefore relevant. In the present paper, Cr/CrN nano-multilayers were obtained with five values of KG [13], combining the advantages of the wear resistance of nitride and the corrosion resistance of Cr-based coatings, in order to study the influence of these coatings on performance.

2. Experimental Procedure

Cr/CrN nano-multilayers were deposited with non-commercial equipment using the UBM technique, which consists of a stainless-steel cylindrical chamber provided with a pumping system (a rotary vane mechanical pump and a turbo molecular pump); the system had a Gencoa sputter VT 100 unbalanced cylindrical magnetron, which allowed varying the magnetic field through a variation of the distance between the internal magnet and the target. A Cr disk with a 4"diameter that was 1/8" thick and had 99.95% purity was used as a target, and was located 50 mm from the substrates, which was sputtered using an MDX 1K DC power supply (Advanced Energy), working at 160 watts power regulation mode. A shutter was located between the target and the sample surface at each interval in order to stabilize the deposition pressure before growing the corresponding layer; base pressure was less than $1\times10-3$ Pa and all multilayers were grown at room temperature. Table 1 summarizes the experiments' deposition conditions. Multilayers were deposited onto H13 steel and Si(100) substrates; metallic substrates were machined into disks with a 15 mm diameter and a 2 mm thickness and were polished to a mirror finish with alumina paste; previously, they had been subjected to quenching and tempering processes in order to increase their surface hardness. Before introducing the substrates into the deposition chamber, all substrates were cleaned in an ultrasonic bath of ethanol and then in acetone. Twenty-five Cr/CrN bilayers were deposited with a thickness of approximately 40 nm each on a Cr layer of approximately 100 nm. The electrochemical behavior was evaluated with the potentiodynamic anodic polarization test, carried out on a three-electrode cell in which the samples were connected to a working electrode; an Ag/AgCl reference electrode and a platinum counter electrode were used. The exposed area was 0.196 cm2. After 1 h of sample immersion in a 3% NaCl solution, scans were conducted in the −250 to 1000 mV range using a 3 mV/s scan rate, with a PCI/300 Gamry potentiostat. Coating surface hardness (H) and Young's modulus (E) were measured using a CSM nanohardness tester, related to ISO 14577 (CSM Instruments SA Switzerland). In this experiment, a 5 mN maximum load was selected, and the linear loading/unloading rates were kept at 10

mN/min. Young's modulus (E) was obtained from the slope of the unloading part of the load–displacement curve using the Oliver and Pharr method [14]. The hardness and Young's modulus measurements were calibrated using a fused silica standard sample.

Table 1. Coating process variables and the results of the nanohardness H and the elastic modulus E, where I is the discharge current and P is the work pressure.

Sample	K_G	Monolayers	I(mA)	P (Pa)	H (GPa)	E (GPa)
1	1.37	CrN [Cr]	467 [447]	0.67 [0.53]	18.905±2.337	289.9±32.4
2	1.25	CrN [Cr]	467 [448]	0.67 [0.525]	22.094±1.233	293.6±34.5
3	1.12	CrN [Cr]	442 [427]	0.68 [0.53]	23.141±2.055	311.9±20.3
4	1.00	CrN [Cr]	428 [416]	0.68 [0.52]	23.014±2.380	318.0±26.0
5	0.87	CrN [Cr]	403 [384]	0.68 [0.53]	24.966±1.448	270.4±20.0
H13	-	-	-	-	11.373±2.525	226.8±7.20

3. Results and discussion

As shown in Table 1, the discharge currents decreased with the increase in the degree of unbalance of the magnetic field; because the discharge power was kept constant, this implies that the potential difference between the target and the substrates increased with the degree of unbalance of the magnetic field. Table 1 also shows the values of nanohardness and elastic modulus, showing a steady increase in their values with the increase in the unbalance of the magnetron, i.e. when KG decreases; this could indicate that the coatings were densified with the increase of this unbalance.

The X-ray diffraction spectra obtained in the Bragg-Brentano configuration, Figure 1, showed the presence of the following phases: Cr, CrN and Cr_2N (ICDD 01-085-1336, 01-079-2159, and 01-0076-2494 cards, respectively). With the X'Pert HighScore program, a semiquantitative analysis was performed, resulting in the percentage composition data shown in Figure 2. The largest percentage content corresponded to the cubic phase CrN, with a lattice parameter of 4.1440 Å; the Cr cubic phase, with a lattice parameter of 2.8849 Å, was the lowest percentage content phase, and the hexagonal Cr_2N phase with lattice parameters of 4.7520 and 4.4290 Å had an intermediate concentration percentage, without apparent correlation with the degree of unbalance obtained.

The results of the potentiodynamic polarization test are shown in Figure 3. It can be seen from this figure that all of the corrosion potential shifted to positive values with respect to the substrate potential, whose value was - 616 mV, and all currents decreased (for the substrate, ICORR = 4.08 μA). In the anodic region, the oscillations in the current are evidence of the film's breaking, and the trends show a passive

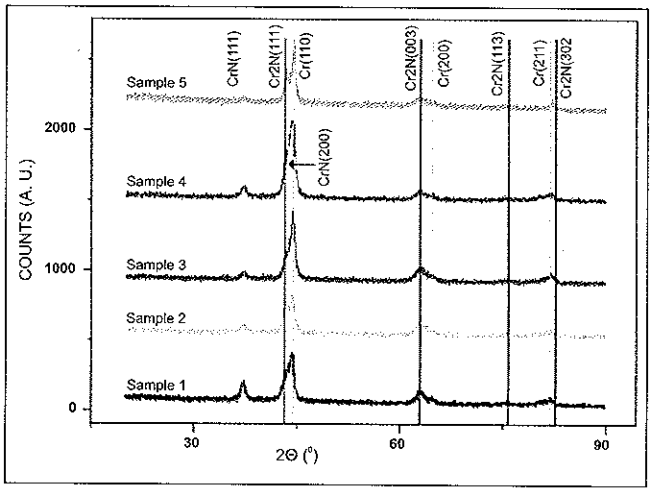

Figure 1. X-ray diffraction spectra for the Cr/ CrN coatings obtained with 5 degrees of unbalance and identifications of the phases present.

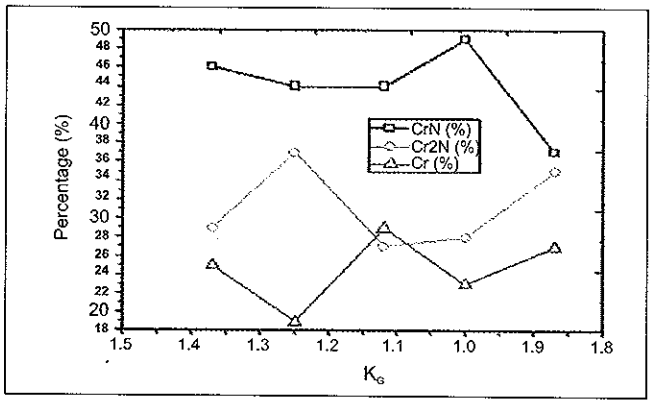

Figure 2. Percent content of the phases present in the Cr/CrN coatings obtained with different degrees of unbalance.

behavior that is especially notable for sample 5, which was obtained with the highest degree of unbalance.

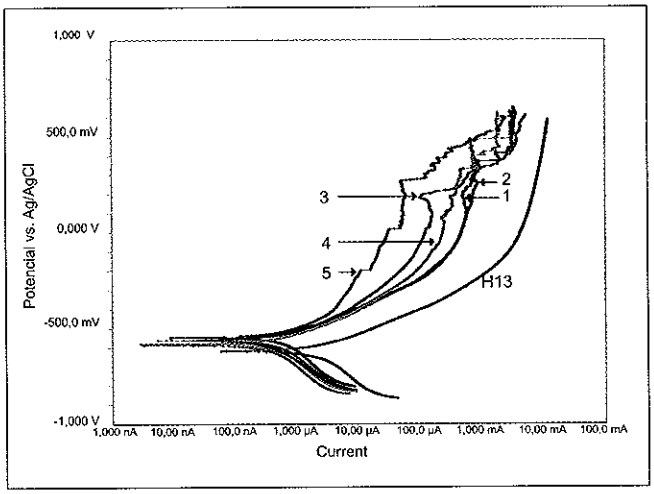

Figure 3. Potentiodynamic polarization test results of the substrate H13 and Cr/CrN coatings.

4. Conclusions

Cr/CrN coatings deposited on H13 steel with quenching and tempering treatments improved the mechanical properties of hardness and corrosion resistance. These improved properties were primarily obtained for coatings with the highest degree of unbalance in the magnetic field, but a monotonous increase was observed between the performance properties of these coatings and the degree of unbalance of the magnetic field, which could be due to an increase in the discharge voltage and therefore the energy of ions impinging on the growing film (i.e., the intensity).

References

[1] **Olaya J. J., Rodil S. E., Muhl S., Huerta L.** 2006, Influence of the energy parameter on the microstructure of chromium nitride coatings, Surface and Coatings Technology 200, 5743-5750.

[2] **Bayón R. et al.** 2009, Corrosion-wear behavior of PVD Cr/CrN multilayer coatings for gear applications, Tribology International 42, 591-599.

[3] **Cerný F., Pitter J., Konvickova S., Jech J.** 2009, High temperature oxidation protective chromium-based coatings prepared by IBAD and PACVD methods Surface and Coatings Technology 203 (2009) 2566-2570.

[4] **Liu C., Bi Q., Mattehws A.** 2001, EIS comparison on corrosion performance of PVD TiN and CrN coated mild steel in 0.5 N NaCl aqueous solution Corrosion Scicence 43, 1953-1961.

[5] **Liu C., Bi Q., Leyland A., Mattehws A.** 2005, An electrochemical impedance spectroscopy study of the corrosion behavior of PVD coated steels in 0.5 N NaCl aqueous solution: PartII.; EIS interpretation of corrosion behavior, Corrosion Science 45, 1257-1273.

[6] **Lousa A. et al.** 2001, Multilayered chromium/chromium nitride coatings for use in pressure die-casting, Surface and Coatings Technology, 146-147, 268-273.

[7] **Podgonik B.** 2001, Coated machine elements – fiction or reality?, Surface and Coatings Technology 146-147, 318-323.

[8] **Mayrhofer P. H. et al.** 2006, Microstructural design of hard coatings, Progress in Material Science 51, 1032-1114

[9] **Ding X., Zeng X. T. and Liu Y. C.** 2011, Structure and properties of CrAlSiN Nanocomposite coatings deposited by lateral rotating cathode arc, Thin Solid Films 519, 1894-1900.

[10] **Su Ch-Y. et al.** 2008, Investigation of the microstructure and characterization of TiN/CrN nanomultilayer deposited by unbalanced magnetron sputter process, Surface and Coatings Technology 203, 657-660.

[11] **Zeng X. T., Mridha S. and Chai U.** 1999, Properties of unbalanced sputtered TiN/NbN multilayer coatings, J. of Mat. Proc. Technol. 89-90, 528-531.

[12] **Zhang J. J., Wang M. X., Yang J., Liu Q. X., Li D. J.** 2007, Enhanced mechanical and tribological performance of multilayered Cr/ZrN coatings, Surface and Coatings Technology 201, 5186-5189.

[13] **Marulanda D. M., Olaya J. J., Piratoba U., Mariño A. and Camps E.** 2011, The effect of bilayer period and degree of unbalancing on magnetron sputtered Cr/CrN nano-multilayer wear and corrosion, Thin Solid Films 519, 1886-1893.

[14] **Cai F., Huang X., Yang Q., Wei R. and Nagy D.** 2010, Microstructure and tribological properties of CrN and CrSiCN coatings, Surface and Coatings Technology 205, 182-188.

THE SOLUTION OF THE NONLINEAR POISSON-BOLTZMANN EQUATION USING LATTICE-BOLTZMANN

SOLUCIÓN DE LA ECUACIÓN NO-LINEAL DE POISSON-BOLTZMANN USANDO EL MÉTODO DE LATTICE-BOLTZMANN

Frank Rodolfo Fonseca Fonseca*

ABSTRACT

Fonseca Fonseca F. R. The solution of the nonlinear Poisson-Boltzmann equation using Lattice-Boltzmann. Rev. Acad. Colomb. Cienc., 37 (1): 94-98, 2013. ISSN 0370-3908.

In this paper we present the solution of the Poisson-Boltzmann equation using the Lattice-Boltzmann method. In order to obtain the solution, we use a redefinition of tensor Π^0, which is declared as a symmetric tensor whose diagonal components are chosen as the second derivative in time of the first moment of the distribution function, and the components outside of the diagonal give account of the nonlinear terms. The results are presented in two dimensions employing the D2Q9 lattice velocity scheme. We obtain results for the scalar field and its gradient for several kinds of initial conditions.

Key words: Poisson-Boltzmann Equation, lattice-Boltzmann.

RESUMEN

En este trabajo se presentala solución de la ecuación de Poisson-Boltzmann utilizando el método de Lattice-Boltzmann. Con el fin de obtener la solución utilizamos una redefinición del tensor Π^0, el cual se declara como un tensor simétrico,cuyas componentesdiagonales se eligen como la segunda derivada en el tiempo del primer momento de la función de distribución y las componentes fuera de la diagonal dan cuenta de los términos no lineales. Losresultados se presentan en dosdimensiones empleando el esquema de rejillas de velocidades D2Q9. Se obtienen resultados para el campo escalar y su gradiente usando varios tipos de condiciones iniciales.

Palabras clave: Ecuación de Poisson-Boltzmann, lattice-Boltzmann.

1. Introduction

The study of Poisson-Boltzmann (PB) equation gives the semiconductor equilibrium energy band for heterostructures (**Lundstrom M. S., Schuelke R. J.** , 1982). Also PB it is very important in the biological sciences, because of the principal role of electrostatics interaction (**Luo G.**, et. al, 2006). The dynamics become more complex when they are mixed biomaterials with low dimensional semiconductors (**Cui Y., et. al**, 2001). On the other hand, a few analytical problems can be solved from weakly charged distributions.

* Universidad Nacional de Colombia, Departamento de Física, Grupo de Ciencia de Materiales y Superficies; Bogotá-Colombia.
E-mail: frfonsecaf@unal.edu.co

Therefore, a lot of work has been done implementing computational techniques in the solution of PB equation, e.g., a combination of a Garlerkin discretization method, the boundary element method, interface methods; a Newton-Krylov method, finite element methods, lattice-Boltzmann, etc. For a discussion of the different computational methods and their efficiency applied to the PB equation the reference (**Lu B. Z. et al.**, 2008) is suggested.

On the other hand, lattice-Boltzmann (LB) has been applied with success to many problems in Physics, and in particular, we find a previous paper (**Wang M., Wang J. and Chen S.**, 2007) on the application of LB to study effects of cavitation and roughness in micro-channels for electro-osmotic flows. Basically, the electric potential and the pressure are introduced as an external force term in the LB expansion. Unlike this approach, our work uses the redefinition of Π^0 tensor of the distribution function as a way to obtain the PB equation.

This manuscript is organized as follows. In section (2) we present the lattice Boltzmann method and the moments of the distribution. Section (3) shows deduction of the PB equation using the definition of the Π^0 tensor. Section (4) presents the equilibrium distribution function, based on **D2Q9** scheme that gives rise to PB equation. In section (5) we present results and in section (6) we give conclusions.

2. The lattice-Boltzmann model

This is considered a bi-dimensional model where the velocities of particles are discretized on the grid into d directions. The lattice-Boltzmann equation is:

$$f_i(\vec{x} + \vec{e}_x\delta t, t + \delta t) - f_i(\vec{x}, t) = \Omega_i(\vec{x}, t) \tag{1}$$

where f_i is the probability density function of finding the group particle i, in the spatial point $\vec{x}$ and time t and δt is the time step. Ω_i is the collision term. It is defined as:

$$\Omega_i(\vec{x}, t) = -\frac{1}{\tau}(f_i(\vec{x}, t) - f^{eq}{}_i(\vec{x}, t)) \tag{2}$$

The collision operator, Eq. (2), is expressed using the B.G.K. approximation (**Bathnagar P. L., Gross E. P. and Krook M.**, 1954), where τ is the non-dimensional relaxation time that measures the approaching rated to the statistical equilibrium. Expanding the left-hand side of Eq. (1) up to second order, in a Taylor series, and using ε as a time step unit, we have:

$$f_i(\vec{x} + \vec{e}_\alpha\varepsilon, t + \varepsilon) - f_i(\vec{x}, t) = \varepsilon\left(\frac{\partial}{\partial t} + e_x\frac{\partial}{\partial x_1} + e_y\frac{\partial}{\partial y_1}\right)f_i + \frac{\varepsilon^2}{2}\left(\frac{\partial}{\partial t} + e_x\frac{\partial}{\partial x_1} + e_y\frac{\partial}{\partial y_1}\right)^2 f_i \tag{3}$$

Assuming the spatial and temporal derivatives as:

$$\frac{\partial}{\partial x} = \mathcal{E}\frac{\partial}{\partial x_1} \tag{4}$$

$$\frac{\partial}{\partial y} = \mathcal{E}\frac{\partial}{\partial y_1} \tag{5}$$

$$\frac{\partial}{\partial t} = \mathcal{E}\frac{\partial}{\partial t_1} + \mathcal{E}^2\frac{\partial}{\partial t_2} \tag{6}$$

Expanding the distribution function f_i in a perturbative series:

$$f_i = f^0{}_i + \mathcal{E}f^1{}_i + \mathcal{E}^2 f^2{}_i \tag{7}$$

we obtain at first order in $\mathcal{E}$:

$$-\frac{1}{\tau}(\mathcal{E}f^1{}_i) = \delta t(\mathcal{E}\frac{\partial}{\partial t_1} + \mathcal{E}e_x\frac{\partial}{\partial x_1} + \mathcal{E}e_y\frac{\partial}{\partial y_1})f^0{}_i \tag{8}$$

and at second order in ε:

$$-\frac{1}{\tau}\mathcal{E}^2 f^2{}_i = \mathcal{E}^2\delta t\frac{\partial}{\partial t_2}f^0{}_i + \frac{\delta t^2}{2}\left(\mathcal{E}\frac{\partial}{\partial t_1} + e_x\mathcal{E}\frac{\partial}{\partial x_1} + \mathcal{E}e_y\frac{\partial}{\partial y_1}\right)^2 f^0{}_i + \delta t(\mathcal{E}\frac{\partial}{\partial t_1} + e_x\mathcal{E}\frac{\partial}{\partial x_1} + \mathcal{E}e_y\frac{\partial}{\partial y_1})\mathcal{E}f^1{}_i \tag{9}$$

where it is assumed that

$$f^0{}_i = f^{eq}{}_i \tag{10}$$

Inserting Eq. (8) in Eq. (9), we obtain:

$$-\frac{1}{\tau}\left(\mathcal{E}f^1{}_i + \mathcal{E}^2 f^2{}_i\right) = \left(\frac{\partial}{\partial t_1} + e_x\frac{\partial}{\partial x_1} + e_y\frac{\partial}{\partial y_1}\right)(\mathcal{E}f^0{}_i + \mathcal{E}^2 f^1{}_i\left(1 - \frac{1}{2\tau}\right)) + \mathcal{E}^2\left(\frac{\partial f^0{}_i}{\partial t_2}\right) \tag{11}$$

Replacing eq. (9) in (11), we obtain:

$$-\frac{1}{\tau}f^2{}_i = \frac{\partial f^0{}_i}{\partial t_2} + (1 - \frac{1}{2\tau})\left(\frac{\partial}{\partial t_1} + e_x\frac{\partial}{\partial x_1} + e_y\frac{\partial}{\partial y_1}\right)f^1{}_i \tag{12}$$

The moments of the distribution function are defined as:

$$\rho = \sum_i f^0{}_i \tag{13}$$

$$\vec{u} = \sum_i \vec{e}_i f^0{}_i \tag{14}$$

$$\Pi^0 = \sum_i \vec{e}_i \cdot \vec{e}_i f^0{}_i, \tag{15}$$

$$\sum_i f^k{}_i = 0,\ k > 0 \tag{16}$$

$$\sum_i \vec{e}_i f^k{}_i = 0,\ k > 0 \tag{17}$$

Also we assume the distribution function f_i satisfies the probability conservation condition with the equilibrium distribution ${f^{eq}}_i$ such that:

$$\sum_{i=0}^{N} {f^{eq}}_i = \sum_{i=0}^{N} {f^{0}}_i \tag{18}$$

3. The Poisson-Boltzmann equation

We do the summation about (i) in Eqs. (8) and (9), and computing (8) and (9)x($\vec{e}_\alpha$), we get:

$$\frac{\partial \rho}{\partial t} + \nabla \cdot \vec{u} = 0 \tag{19}$$

and

$$\frac{\partial \vec{u}}{\partial t} + \nabla \cdot \Pi^0 = 0 \tag{20}$$

We assume Π^0 as a symmetric tensor given by:

$${\Pi_{\mu\nu}}^0 = \frac{\partial^2 \rho}{\partial t^2}\delta_{\mu\nu} + (1-\delta_{\mu\nu})(\rho - \kappa^2 \sinh(\rho)) \tag{21}$$

where κ^2 is a constant. Replacing Eq. (21) and (21-a) in Eq. (20), we obtain for the diagonal components of the tensors:

$$\frac{\partial \vec{u}}{\partial t} + \nabla\left(\frac{\partial^2 \rho}{\partial t^2}\right) = 0 \tag{22}$$

and the off-diagonal components are:

$$\nabla(\rho - \kappa^2 \sinh(\rho)) = 0 \tag{23}$$

and we assume it as:

$$(\rho - \kappa^2 \sinh(\rho)) = 0 \tag{24}$$

Then eq. (23)

$$\frac{\partial}{\partial t}(\vec{u} + \frac{\partial}{\partial t}\nabla(\rho)) = 0 \tag{25}$$

assuming

$$\vec{u} + \frac{\partial}{\partial t}\nabla(\rho) = 0 \tag{26}$$

Taking divergence

$$\nabla.\vec{u} + \frac{\partial}{\partial t}\nabla^2(\rho) = 0 \tag{27}$$

Using Eq. (19)

$$-\frac{\partial \rho}{\partial t} + \nabla^2(\rho) = 0 \tag{28}$$

Taking out the temporal derivative

$$\frac{\partial}{\partial t}(\rho - \nabla^2(\rho)) = 0 \tag{29}$$

assuming

$$\rho - \nabla^2(\rho) = 0 \tag{30}$$

Using eq. (24), we have the Poisson-Boltzmann equation:

$$\nabla^2 \rho = \kappa^2 \sinh(\rho) \tag{31}$$

4. The equilibrium distribution function

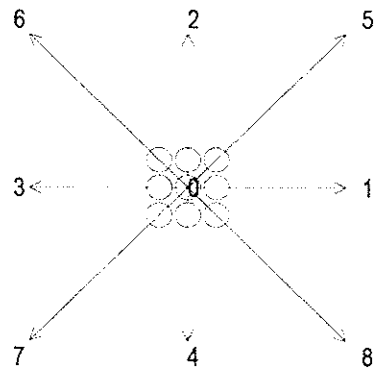

Fig.1. The lattice velocities of the **D2Q9** scheme.

We use the **D2Q9** velocity scheme shown in fig. (1), for the directions $\vec{e}_i$ and weights w_i on each cell:

$$w_i = \begin{Bmatrix} \frac{4}{9} & \rightarrow & i = 0 \\ \frac{1}{9} & \rightarrow & i = 1,2,3,4 \\ \frac{1}{36} & \rightarrow & i = 5,6,7,8 \end{Bmatrix} \tag{32}$$

Both directions $\vec{e}_i$ and weights w_i follow the next set of tensor relations:

$$\sum_i w_i \, e_{i,\alpha} = 0 \tag{33}$$

$$\sum_i w_i \, e_{i,\alpha} e_{i,\beta} = \frac{1}{3}\delta_{\alpha,\beta} \tag{34}$$

$$\sum_i w_i \, e_{i,\alpha} e_{i,\beta} e_{i,\gamma} = 0 \tag{35}$$

Also, we assume the equilibrium function

$${f^{eq}}_i = \begin{Bmatrix} w_i(A + B\vec{e}_i \cdot \vec{u}) & i > 0 \\ w_0 C & i = 0 \end{Bmatrix} \tag{36}$$

Using Equations (13-17) that define the moments of the distribution, and also the set of equations that give the tensor relations of the lattice velocity equations (27-28), we obtain:

$$A = 3\left(\frac{\partial^2\rho}{\partial t^2} - \kappa^2\rho - \kappa^2\sinh(\rho)\right) \tag{37}$$

$$B = 3 \tag{38}$$

$$C = \frac{9}{4}\rho - \frac{5}{4}\left(\frac{\partial^2\rho}{\partial t^2} - \kappa^2\rho - \kappa^2\sinh(\rho)\right) \tag{39}$$

Then, the equilibrium distribution function that satisfies the Helmholtz equation is:

$$f^{eq}{}_i = \begin{cases} 3w_i\left(\vec{e}_i\cdot\vec{u} + \left(\frac{\partial^2\rho}{\partial t^2} - \kappa^2\rho - \kappa^2\sinh(\rho)\right)\right) & i > 0 \\ w_0\left(\frac{9}{4}\rho - \frac{5}{4}\left(\frac{\partial^2\rho}{\partial t^2} - \kappa^2\rho - \kappa^2\sinh(\rho)\right)\right) & i = 0 \end{cases} \tag{40}$$

5. Analysis and Results

We use the difference discretization scheme of the second derivative, in order to apply the distribution function, as:

$$\frac{\partial^2\rho}{\partial t^2} = \frac{\rho(x,t+\delta t) - \rho(x,t) + \rho(x,t-\delta t)}{\delta t^2} \tag{41}$$

The system is initialized with the function:

$$f_i(x,y,0) = A_1 sin(D(x+2)^2 + D(y+2)^2) \tag{42}$$

and

$$f_i(x,y,0) = A_1 exp(-D(x+2)^2 - D(y+2)^2) \tag{43}$$

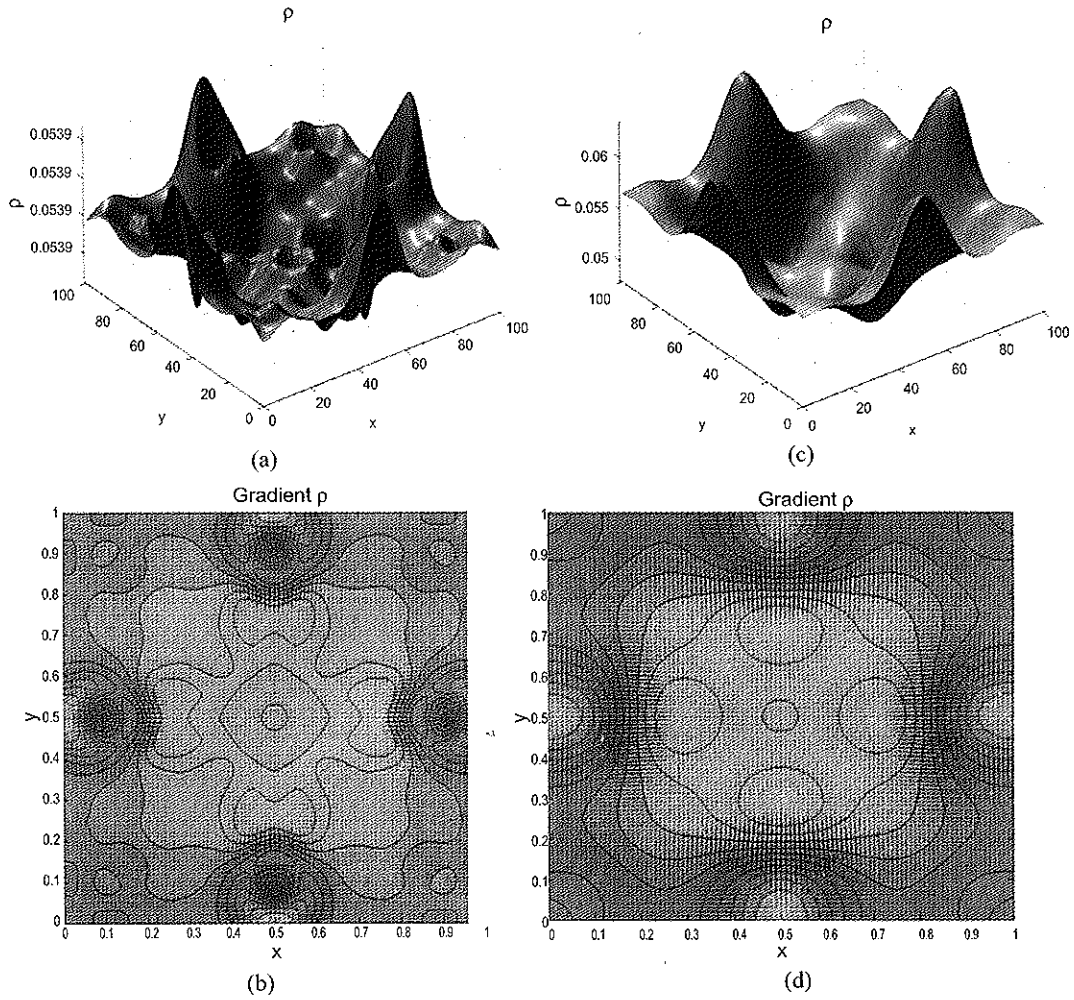

Fig.2. The numerical result of the d1q3 lattice Boltzmann model. Panels (a)-(d) correspond to simulations at times t = 140Δt. Parameters are: lattice size L = 100, κ =20,07, Δx = Δy = 1/L.

Then the algorithm initiates at $t_0 = 0$, with Eq. (42) or (43) in all the nodes of system. We present results for simulations in Figure (2), panels (a-d) for a system size of ***100x100***, with periodic boundaries conditions. In Figures (2) a-b, we show results for an initial Sine pulse and its gradient field. For Figures (2) c-d, we have the potential and the gradient field, respectively, for an initial Gaussian pulse.

5. Conclusions

We have solved the Poisson-Boltzmann equation using the lattice-Boltzmann technique. We obtain the structure of the potential and its gradient field for Sine and Gaussian initial configurations. This method can be easily extended to three dimensions. For a future paper, we can extend the method to explore phenomenology for unbalanced charge distributions.

7. Acknowledgments

This paper was supported by Universidad Nacional de Colombia (DIB-8003355).

8. References

[1] **Lundstrom M. S., Schuelke R. J.** , 1982, Modeling semiconductor heterojunctions in equilibrium, *Solid State Electron,* **25** 683-691.

[2] **Luo G., et. al**, 2006, Ion Distributions near a Liquid-Liquid Interface *Science*, **311** 216-218.

[3] **Cui Y., et. al**, 2001, Nanowire Nanosensors for Highly Sensitive and Selective Detection of Biological and Chemical Species, *Science*, **293** 1289-1292.

[4] **Lu B. Z. et al.**, 2008, Recent progress in numerical methods for the Poisson-Boltzmann equation in biophysical applications, *Commun. Comput. Phys.* **3** 973-1009.

[5] **Wang M., Wang J. and Chen S.**, 2007, Roughness and cavitations effects on electro-osmotic flows in rough microchannels using the lattice Poisson-Boltzmann methods, *Journal of Computational Physics*, **226** 836-851.

[6] **Bathnagar P. L., Gross E. P. and Krook M.**, 1954, A Model for Collision Processes in Gases. I. Small Amplitude Processes in Charged and Neutral One-Component Systems, *Phys. Rev.* **94** 511-525.

STRUCTURAL ANALYSIS OF NbN THIN FILMS GROWN THROUGH RF MAGNETRON SPUTTERING

ANÁLISIS ESTRUCTURAL DE PELÍCULAS DELGADAS DE NbN CRECIDAS A TRAVÉS DE PULVERIZACIÓN CATÓDICA MAGNETRÓN RF

J. E. Alfonso*,, J. J. Olaya*, A.P.C. Campos***, M.E. Mendoza*****

ABSTRACT

Alfonso J. E, J. J. Olaya, A.P.C. Campos, M.E. Mendoza: J. E Structural analysis of NbN thin films Grown through rf magnetron Sputtering. Rev. Acad. Colomb. Cienc., 37 (1): 99-103, 2013. ISSN 0370-3908

In this work NbN thin films have been grown through rf magnetron sputtering technique from a δ-NbN (99.99%) target. In particular, we have studied the influence of the additional N2 flux in the preparation chamber in crystallization and microstructure of the deposited films. The films have been characterized by X-Ray diffraction (XRD) in θ-2θ configuration and at grazing angle, scanning electron microscopy (SEM) and transmission electron microscopy (TEM). XRD results show that the films grown at different fluxes of N2 have high textured coefficient along [200] direction. SEM results indicate the films have columnar growth with high homogeneity and average thickness of 0.7 μm. TEM results reveals that the films have grown from crystalline nanoparticles of NbN with highly textured along the (200) plane.

Keywords: Thin films, grazing angle, crystalline structure, nanoparticles.

RESUMEN

En este trabajo se han crecido películas delgadas de NbN a través de la técnica de pulverización catódica magnetrón rf a partir de un blanco de δ-NbN (99,99%). En particular, se ha estudiado la influencia que tiene la incorporación de flujo adicional de N2 a la cámara de preparación en la cristalización y la microestructura de las películas depositadas. Las películas se han caracterizado por difracción de rayos X (DRX) en la configuración de θ-2θ y en ángulo de incidencia rasante, microscopía electrónica de barrido (SEM) y microscopía electrónica de transmisión (TEM). Los resultados de DRX muestran que las películas crecidas en diferentes flujos de N2 tienen alto coeficiente de textura a lo largo de la dirección [200]. Los resultados de SEM indican

* Grupo de Ciencia de Materiales y Superficies, Universidad Nacional de Colombia, Bogotá, Colombia. E-mail: jealfonsoo@unal.edu.co

** Investigador asociado al Centro Internacional de Física, Bogotá, Colombia.

*** Divisão de Metrologia de Materiais, Instituto Nacional de Metrologia, Qualidade e Tecnologia, Rio de Janeiro, Brazil.

que las películas tienen un crecimiento columnar con alta homogeneidad y espesor medio de 0,7 μm. Los resultados de TEM revelan que las películas han crecido a partir de nanopartículas cristalinas de NbN con alta textura a lo largo del plano (200).

Palabras clave: Películas delgadas, ángulo rasante, estructura cristalina, nanoparticulas.

1. Introduction

Transition metal nitrides have physics and chemical properties such as high fusion points and chemical stability that allow it be used in different applications spanning from hard coatings to electromagnetic radiation detectors. For instance, the NbN films have been studied as potentially useful material for low temperature electronics, because the highest transition temperature is of approximately 17.3 K, value that allows to be used in fabrication of multilayer films of (NbN/AlN/NbN) type which have been used as tunnel junctions [1, 2]. Likewise, due their value of work function (4.7 eV) there is the possibility of using NbN as cathode in vacuum microelectronic devices [3]. Other nitrides such as TiN and TaN have been used as diffusion barriers to prevent copper diffusion into silicon used in microelectronic devices.

Although NbN has been prepared as thin films using different techniques including reactive phase rf magnetron sputtering [4, 5], pulsed laser deposition (PLD), or atomic layer deposition [6], influence of some deposit fabrication parameters such as argon pressure in the work chamber or the power supplied to the target on the structural properties of the deposited materials have not been studied. This work presents results obtained from the growth of NbN thin films on glass substrates, through rf magnetron sputtering technique which has proven to be quite versatile to prepare a variety of different materials [7]. In particular, we have studied the crystalline structure, microstructure and morphology of the NbN films deposited with different nitrogen fluxes.

2. Experimental techniques

The equipment used to grow the NbN films is an Alcatel HS 2000 rf magnetron described in previous papers [8]. The NbN films were obtained from a 4"x1/4" NbN (99.9%) target (CERAC, Inc.). The parameters used during deposition process were: base pressure 2.0×10^{-4} Pa, total working pressure 7×10^{-1} Pa, deposition time 30 min, target–substrate distance 5 cm and argon (99.999%) flux in 20 standard cubic centimeters per minute (sccm). We studied the influence of additional nitrogen (99.99%) flux inside the deposit chamber (Φ= 2, Φ = 4, and Φ = 6 sccm) in the structural and microstructure of the films. The final working pressure was maintained using a valve controller for all the nitrogen flow values given above, the argon and nitrogen flows were controlled by mass flow controllers.

The structural characterization of the films was performed by X-ray diffraction (XRD) with a Philips diffractometer operated at 30 kV and 20 mA and using Cu Kα radiation. Surface morphology was characterized by imaging the secondary electrons with a FEI-Quanta 2000 scanning electron microscope operating at 15 kV and 10 mA filament current. Microstructure characterization was carried out with 2100F and FEI-Titan 80-300 transmission electron microscope, both equipped with energy-dispersive X-ray spectroscopy detector (EDXS).

The samples analyzed by TEM were prepared according to the following procedure: two samples with rectangle shape (4x5 mm) were cut, these two rectangles were glued with epoxy resin, cross section slices were obtained using an ultrasonic cut, the slices were fixed in a brass tube (3 mm diameter) and further disks were cut, the disks were thinned with sandpaper and disks with abrasive (40, 15 and 4 μm grain-size), final thinned sample was obtained with a dimple and the finally step was ion beam milling using Ar ions at 5 keV.

3. Results and discussion

Fig. 1a shows the Rietveld analysis carried out in the target used to growth the NbN thin films. The study established that the crystalline phase of the target is δ-NbN (a= 4.3927Å) face centered-cubic (SG Fm-3m). The fig. 1b shows the difference between the experimental and calculated XRD patterns.

In a previous work we found that the optimal conditions to deposit NbN thin films were: 300 W of power supply to the target and heating the substrate to 553 K [9]. In order to study the influence of gas addition on the structural and morphology properties of the NbN films we have introduced nitrogen gas in the deposition chamber. XRD studies of these films have previously been performed and are detailed elsewhere [9], in brief it was shown that in all cases a preferential growth appears along the (200) plane (see Fig. 2) and the polycrystalline character of the film was established by X-ray diffraction experiments at grazing incidence (see Fig. 3). These results indicate that incorporation of nitrogen du-

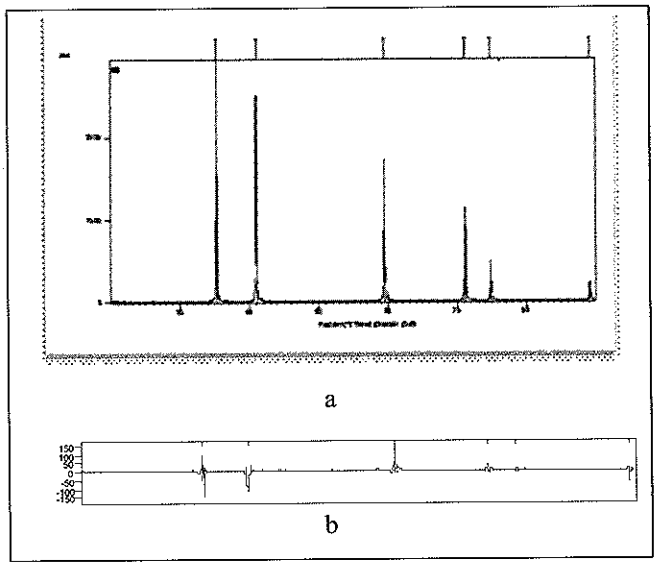

Figure 1 a- Experimental XRD pattern and calculated of NbN target and b- difference of the two patterns.

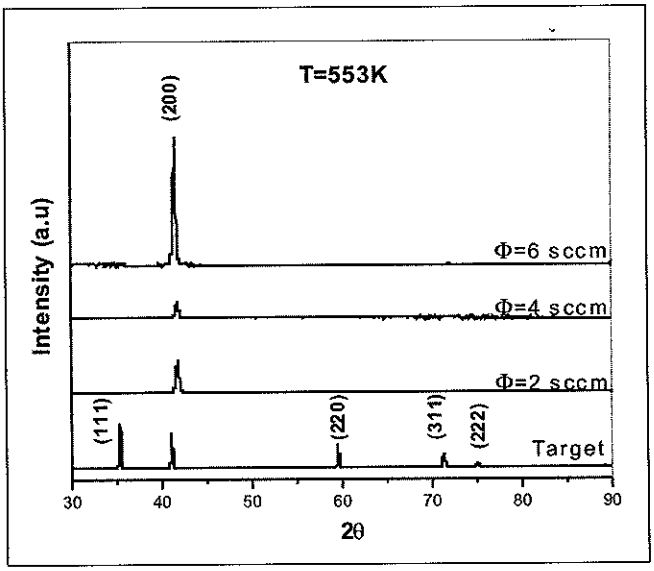

Figure 2. XRD patterns recorded from NbN films deposited at 553 K, 300 W and with different nitrogen fluxes. The pattern of the target from which the films were obtained is included for comparison purposes. Published with permission number 3157800386723 of JMS.

ring the growth of the films determined the direction of the δ-NbN phase, this is evidencing by texture coefficient (defined as $[\Gamma_{(200)} = I_{(200)}/ [I_{(200)} + I_{(111)} + I_{(220)} + I_{(311)} + I_{(222)}]$ where I is the intensity of diffraction peak) which was of 0.65 to the films grown at 6 sccm.

Moreover, previous works on the growth of NbN thin films by different techniques (sputtering, cathodic arc, and reactive methods) [10, 11] have established that the variation in texture may depend on factors such as the treatment of the substrate prior coating, the deposition rate [6] the type of substrate and the highly non-equilibrium condition of the plasma sputtering [12]. Furthermore, Bendavid *et al.* [13] showed that the substrate bias voltage also affects the microstructure and preferred orientation. Also it has been shown that changing the nitrogen flow during the growth of TiN films interchanges the preferred orientation of the films from the [111] direction to the [200] direction, it is due to incorporation of nitrogen during the deposition process that implies changes in the dynamics of the plasma since the increase in the number of nitrogen molecules increases the probability of collisions, promoting a larger number of chemical reactions on the substrate surface. Consequently, the presence of the nitrogen atoms reduces the flux of cations from the (200) to the (111) planes, resulting in the orientation of the growth in the [200] direction [14].

The surface morphology of these films have previously been characterized [9], showing that the grown NbN films present a compact granular structure, with a columnar growth of the

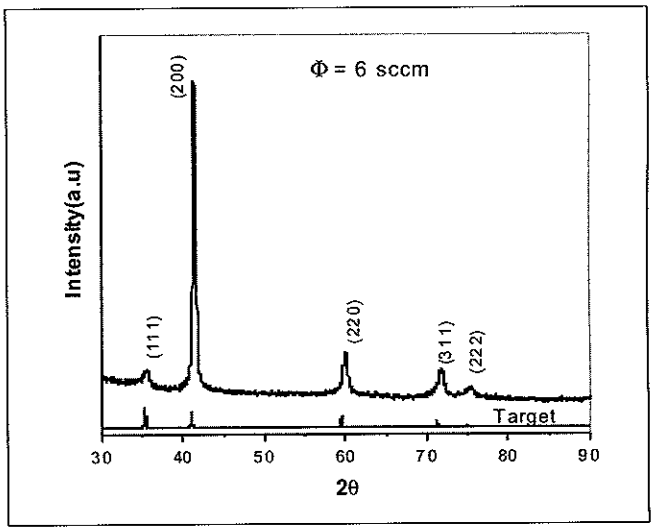

Figure 3. Grazing angle (2°) XRD pattern recorded from a NbN film grown at 553 K, 300 W, and 6 sccm nitrogen flux. The target XRD pattern is included as reference. Published with permission number 3157800386723 of JMS.

type described by Movchan and. Demchishin [15] having an average thickness of 0.7 μm (see Fig. 4).

The structural analysis of the NbN films was completed by transmission electron microcopy (TEM) through the electron diffraction patterns (DP) measurements and high resolution

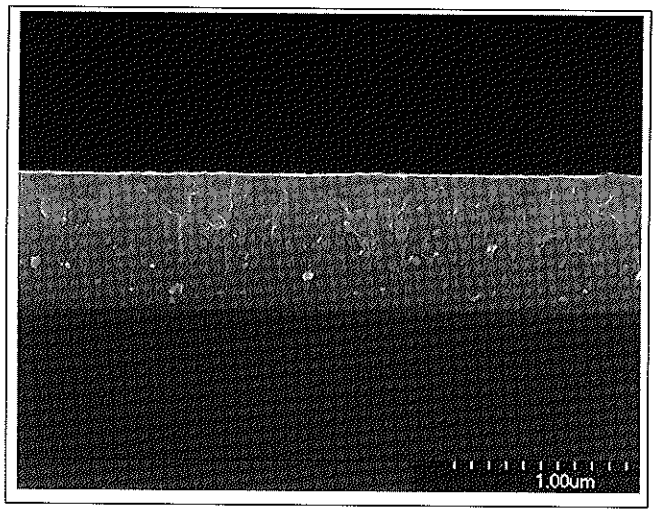

Figure 4. Cross-section SEM micrograph obtained with secondary electrons of the NbN film grown at 300 W, 513 K and 6sccm nitrogen flux. Published with permission number 3157800386723 of JMS.

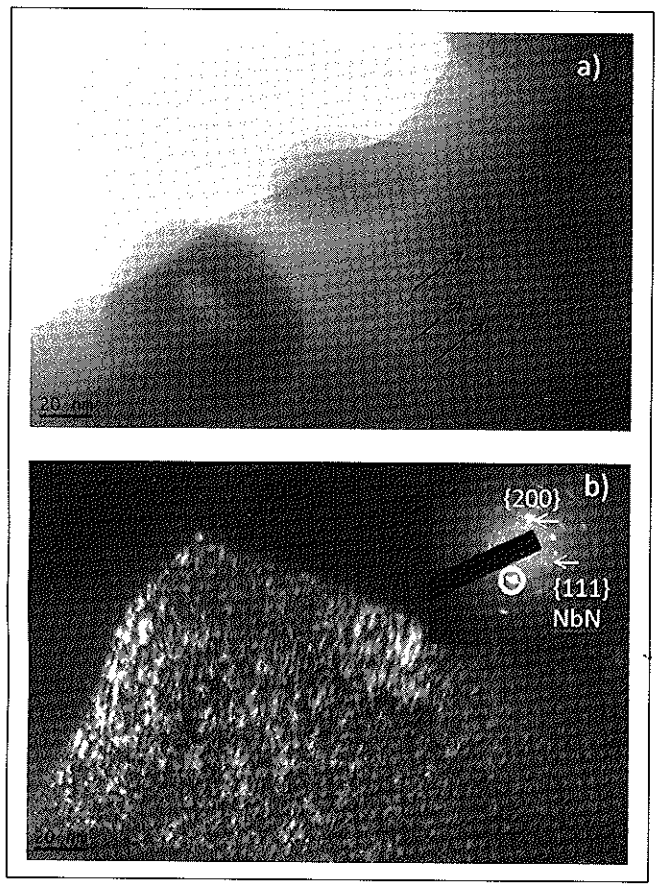

Figure 5. a) Bright field image of the film grown at 2 sccm nitrogen flux and b) dark field imageof the film grown at 6 sccm, with the corresponding electron diffraction pattern.

images (HRTEM) obtained from the films which were grown at 2 and 6 sccm of nitrogen flux. Fig. 5a corresponds to the bright field image of the film grown at 2sccm and Fig. 5b shows the dark -field image of the film which was grown in a high flux (6 sccm). Where, it can be seen that the film is formed by concentrated clusters of nanoparticles with dimension less than 10 nm and that the films grown at 6 sccm have a nanostructured morphology and grew mainly along of {111} and {200} family planes.

TEM analysis was also performed to analyze the NbN films morphology as a function of nitrogen flux, Fig. 6a and 6b show the morphology of the NbN films grown at 2 sccm and 6 sccm nitrogen fluxes, respectively. Micrographs reveal

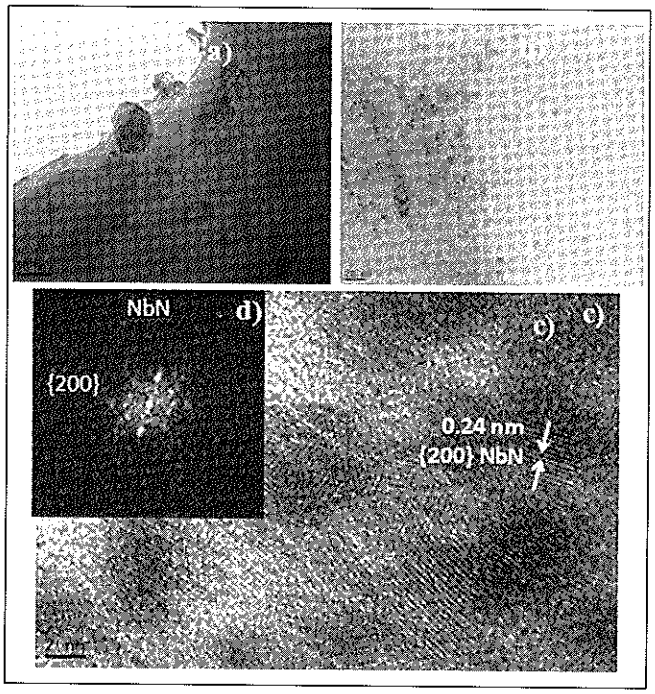

Figure 6. TEM images showing NbN nanoparticles with spherical morphology at different nitrogen fluxes: a) 2 sccm; b) 6 sccm; c) HRTEM image, NbN nanograins growing in a preferential direction of atomic planes (200) can be observed in d.

films are nano structured and that there are constituted by clusters and amorphous regions. All the samples are formed by nanograins homogenously distributed. The size of clusters was in the 2 nm to 10 nm range. It was observed that the amount of NbN clusters increases as the nitrogen flux increases too. Using Gatan software we have determined that the average grain size of the nanoparticles was 2.7 ± 0.6 nm with normal distribution. HRTEM image (Fig. 6c) presents an interferential pattern produced by the atomic planes and its corresponding Fourier transform, lets us visualize the re-

ciprocal space of one NbN nanoparticle (Fig. 6d). Measuring the distance between the spots (0.24 nm), we can confirm that they correspond to the (200) planes of δ-NbN. These results are in agreement with XRD analysis, which established that NbN grows preferentially along the (200) plane. The physical explanation of the phenomena that produces the preferential growth along the (200) plane of NbN has been given in a previous work [9].

Finally, EDX analysis (Fig. 7) confirms that the analyzed clusters were constituted by Niobium and Nitrogen. Si, Al, Ba, Fe, O correspond to the elements of the common glass substrate. Presence of copper is due to the sample holder.

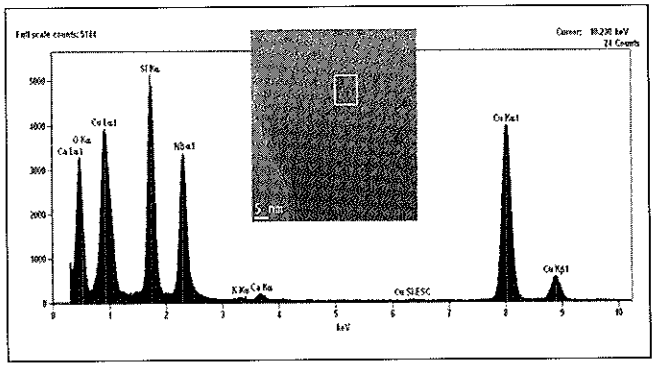

Figure 7. EDX spectrum of NbN films grown at 6 sccm of nitrogen flux.

Conclusions

The results obtained in this work indicate that during the preparation of NbN films by rf magnetron sputtering, the variation of nitrogen flux introduced in the preparation chamber has decisive influence on the orientation and morphology of the deposited films, since that as a function of the nitrogen flux, these grow with high texture coefficient along the [200] direction and the morphology evolves from nanometric clusters to nanoparticles homogeneously distributed.

References

[1] **Ishiguro T, Matsushima K, Hamasaki K** "Sectional structures and electrical properties of ultrathin NbN/MgO bilayers on Si(100)" , J. Appl. Phys 73, 1151-1153, 1993.

[2] **Wang Z., Kawakami A., Uzawa Y., Komiyama B. J.,**" Superconducting properties and crystal structures of single-crystal niobium nitride thin films deposited at ambient substrate temperature", J. Appl. Phys. 79, 7837- 7842,1996.

[3] **Gotoh Y., Nagao M., Ura T., Tsuji H., Ishikawa J.,** "Ion beam assisted deposition of niobium nitride thin films for vacuum microelectronics devices", Nucl Instr. Meth. Phys. Res. B. **148,** 925-931, 1999.

[4] **Wong M.S., Sproul WD, Chu X, Barnett S.A.,** "Reactive magnetron sputter deposition of niobium nitride films", J. Vac. Sci. Technol. A **11(4),** 1528-1536 ,1993.

[5] **Havey K.S., Zabinski J.S., Walck S. D.,** "The chemistry, structure, and resulting wear properties of magnetron-sputtered NbN", Thin Solid Films, **303**, 238- 245, 1997.

[6] **Alén P., Ritala M., Arstila K., Keinonen J., Leskela M.,** "The growth and diffusion barrier properties of atomic layer deposited NbN thin film", Thin Solid Films 49, 235- 239, 2005.

[7] **Yu J.H., Park D.S., Kim J.H., Jeong .T.S., Youn C. J., Hong K.J.,** "Post-growth annealing and wide bandgap modulation of BeZnO layers grown by RF co-sputtering of ZnO and Be targets", J. Mater. Sci. **45**,130-135 , 2010.

[8] **J.E. Alfonso, J. Torres,J.F Marco,** "Influence of the substrate bias voltage on the crystallographic structure and surface composition of Ti6Al4V thin films deposited by rf magnetron sputtering", Brazilian J. Phys. Vol. **36** no. **3B**, 993-996, 2006.

[9] **J. E. Alfonso , J. Buitrago,J. Torres, J. F. Marco, B.** Santos, "Influence of fabrication parameters on crystallization, microstructure, and surface composition of NbN thin films deposited by rf magnetron sputtering", J. Mater. Sci. **45,** 5528-5533 , 2010.

[10] **Rutherford K. L., Hatto P.W., Davies C, Hutchings I.M.,** "Abrasive wear resistance of TiN/NbN multi-layers: measurement and neural network modeling", Surf. Coat. Technol. , **86,** 472- 479, 1996.

[11] **Zhitomirsky V.N., Grimberg I., Rapport L., Travitzky N.A.,** Boxman R.L., Goldsmith S., Raihel A., Lapsker I., Weiss B. Z., "Structure and mechanical properties of vacuum arc-deposited NbN coatings", Thin Solid Films, **326,** 134- 142, 1998.

[12] **Chu X., Wong M.S., Sproul W. D., Rhode S.L, Barnett S. A.,** "Deposition and properties of polycrystalline TiN/NbN superlattice coatings J. Vac. Sci. Technol. A10 1604 - 1609, 1992.

[13] **Bendavid A., Martin P. J., Kinder T.J., Preston E.W.,** "The deposition of NbN and NbC thin films by filtered vacuum cathodic arc deposition", Surf. Coat. Technol., 163, 347-352 , 2003.

[14] **Huang J-H, Lau K-W, Yu G-P.,** "Effect of nitrogen flow rate on structure and properties of nanocrystalline TiN thin films produced by unbalanced magnetron sputtering", Surf. Coat. Technol. **191**,17-24, 2005.

[15] **B. A. Movchan and A. V. Demchishin, Fiz.,** "Study of the Structure and Properties of Dioxide thin, Met. Metalloved, **28,** 83-90 ,1969.